SPECTROSCOPIC STUDY OF THE ADSORPTION COMPLEXES OF BENZENE AND OXYGEN ON CU/HZSM5 ZEOLITES

VON DER FAKULTÄT CHEMIE DER UNIVERSITÄT STUTTGART ZUR ERLANGUNG
DER WÜRDE EINES DOKTORS DER NATURWISSENSCHAFTEN (DR. RER. NAT.)
GENEHMIGTE ABHANDLUNG

vorgelegt von

Augusta Bianca Ene

aus Cluj-Napoca, Rumänien

Hauptberichter:	*Prof. Dr. E. Roduner*
Mitberichter:	*Apl. Prof. Dr. M. Hunger*
Tag der mündlichen Prüfung:	*23.11.2010*

INSTITUT FÜR PHYSIKALISCHE CHEMIE
DER UNIVERSITÄT STUTTGART

2010

Eidesstattliche Erklärung

Ich versichere, dass ich diese Dissertation selbstn̈dig verfasst und nur die angegebenen Quellen und Hilfsmittel verwendet habe.

Stuttgart, den 26.01.2011 *Augusta Bianca Ene*

To my family

There is a theory which states that if ever anyone discovers exactly what the Universe is for and why it is here, it will instantly disappear and be replaced by something even more bizarre and inexplicable. There is another theory which states that this has already happened.

-Douglas Adams

CONTENTS

Contents **1**

1 Introduction **5**
- 1.1 Motivation 5
- 1.2 Phenol Production 6

2 Zeolites **9**
- 2.1 General Information 9
- 2.2 The ZSM5 Zeolite 10
- 2.3 Generation of Acid Sites 11
- 2.4 Copper Exchanged HZSM5 15

3 Infrared Spectroscopy **19**
- 3.1 Molecular Vibrations 19
- 3.2 Vibrational Spectra 21
- 3.3 Molecular Rotation 21
- 3.4 Rotation - Vibration Interaction 22
- 3.5 Isotopic Shifts 23
- 3.6 Absorption of Infrared Radiation 23
- 3.7 Fourier Transform Spectroscopy 25

4 Electron Paramagnetic Resonance **29**
- 4.1 The Electron Spin and Magnetic Moment 29
- 4.2 Electron Spin in a Magnetic Field: the Zeeman Effect 30
- 4.3 Spin-Orbit Coupling 31
- 4.4 Hyperfine Coupling 32
- 4.5 The Hamiltonian 35
- 4.6 g-Anisotropy 37
- 4.7 Electron Exchange Coupling 38
- 4.8 Macroscopic Magnetization 38

5 Experimental Details 41
5.1 Sample Preparation 41
5.2 FTIR Measurements 42
5.3 EPR Measurements 44
5.4 Gas Chromatography Measurements 48
5.5 UV-Vis Measurements 49
5.6 EXAFS and XANES Measurements 49

6 Initial State of the Catalyst 51
6.1 FTIR Spectra 51
6.2 EPR Spectra 53
6.3 UV-Vis Spectra 57
6.4 EXAFS Measurements 58
6.5 Discussion 59

7 Oxygen Adsorption 61
7.1 FTIR Spectra 61
7.2 EPR Spectra 69
7.3 Discussion 76

8 Benzene Adsorption 79
8.1 FTIR Spectra 79
8.2 EPR Spectra 90
8.3 Discussion 99

9 Competitive Adsorption of Oxygen and Benzene 101
9.1 FTIR Spectra 101
9.2 EPR Spectra 107
9.3 GC/MS Measurements 113
9.4 Discussion 114

10 Comparison between the Cu/HZSM5 and Cu/HY Zeolites 115

11 Conclusions 117

12 Summary 121

13 Zusammenfassung 127

14 Abbreviation List 133

List of Figures 137

List of Tables **145**

Bibliography **147**

Acknowledgment **153**

CHAPTER 1

INTRODUCTION

1.1 MOTIVATION

The phenol production by a one step, environmentally friendly catalytic oxidation of benzene is an attractive but also very challenging alternative to the commercially used three-step Cumene process. Giving a yield between only 4%[1] and 10%[2], the Cu/HZSM5 zeolite was found to be the most active catalyst for the oxidation of benzene to phenol with molecular oxygen in the gas phase. Even though studies of this reaction over various iron[3] or copper[1,4–6] supported catalysts have already been reported, the detailed reaction mechanism is still unknown. This information would permit an intentional modification of the zeolite to favor phenol formation.

First, the initial state of the catalyst has to be fully known before the changes that it undergoes during the reaction can be understood. Then the adsorption complexes of oxygen and benzene on copper-containing and copper-free HZSM5 zeolites have to be studied independently of each other in order to be able to point out the catalytically active sites among the different adsorption sites, the hydroxyl groups of the parent zeolite and the exchanged copper ions.

The study of benzene adsorption is of great interest not only for the optimization of the phenol production, but also for the understanding of the kinetics of many catalytic reactions, since it is a component of numerous processes conducted with zeolite catalysts and is often used as a probe molecule for studying the adsorption in the tight pore space of zeolites.[7,8] In literature the benzene adsorption on the plain HZSM5 zeolite has been studied both by experimental methods[9–18] and theoretical calculations[19] but no agreement was reached concerning the preferential adsorption sites. The interaction of the exchanged copper ion with benzene has been discussed more recently in FTIR and DFT studies[20–22] but no clear picture of the coordination of benzene to copper and the activation of the molecule is available.[23,24]

For the desired oxidation reaction of benzene to phenol both benzene and oxygen must interact with the catalyst at the same time. This can be achieved either by adding both reactants simultaneously to the catalyst sample or by inserting them one after the other. In both cases one of the molecules might be a stronger adsorbate on one type of adsorption center than the other one, possibly being able to even displace the first. If the adsorption strengths of benzene and oxygen are similar it could also be conceivable that both molecules adsorb together on the same catalytic center, a fact that could facilitate the cracking of benzene. The competitive adsorption of benzene and oxygen must be studied as well as their behavior under reaction conditions.

By combining the published theoretical calculations with different spectroscopic methods (EXAFS, EPR, FTIR and UV-Vis) and product analysis (via gas chromatography) we will attempt to characterize the active copper centers in their initial form, as well as their interaction with the reactants. The present work is part of an extended program in which the oxidation of benzene to phenol using molecular oxygen is first studied for Cu/HY and Cu/NaY. The faujasite is of cubic crystal symmetry which makes it more suitable for theoretical calculations. Since it does not perform the benzene to phenol oxidation its comparison to the Cu/HZSM5-system should facilitate the determination of the catalytically important steps and enable us to propose a reaction path for the catalytic cycle.

1.2 PHENOL PRODUCTION

Since 1952 phenol is commercially available and is used in medicine, color industry and as an intermediate for the manufacture of various petrochemicals. Since then it is produced via the so-called Cumene Process (figure 1.1), which includes three steps: the alkylation of benzene to cumene, the oxidation to cumene hydroperoxide and its hydrolysis to phenol and acetone. The advantage of this process is that it takes two inexpensive starting materials benzene and propylene and transforms them into two expensive products. One major disadvantage is that it produces as much acetone as phenol. Up to 6.7 million tons of phenol are synthesized each year with 4.1 million tons of acetone as an equimolar side product.[25] The acetone price is thus driving the economic efficiency of the process. Furthermore, hazardous compounds like aluminium chloride, phosphorous- and sulfuric acid are needed. Smaller amounts of phenol are produced also via toluene oxidation or recovered from coal tar.

For this reasons a process is desired whereby phenol could be formed in one step. A great advantage would be gained by the use of a solid state catalyst which would ease the product extraction. In literature, there are many proposed oxidation processes over various catalysts, but most give only small yields and are of

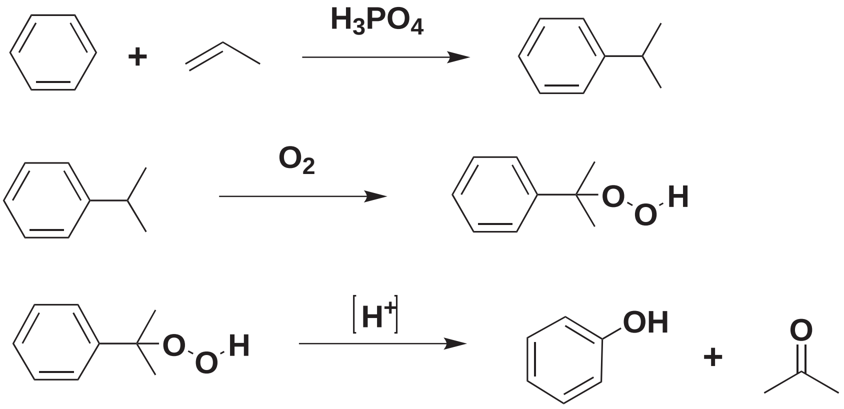

Figure 1.1: Cumene process

no industrial interest. The use of hydrogen peroxide on titanium silicalites gives a 30% yield at high selectivity but the high price of hydrogen peroxide makes the process not profitable. The only process used on a large scale, is the direct oxidation of benzene with N_2O over ZSM5 zeolites.[25] The use of N_2O is convenient since it is a greenhouse gas and must be decomposed to avoid emission but implies also carefull and elaborate handling in order to avoid emission.

Kitamura et. al.[5] proposed a reaction mechanism for the oxidation of benzene in liquid phase with oxygen as oxidant and ascorbic acid as reducing agent, though the charge balance is not complete. The highest yield was obtained on CuHY zeolite (2.5%) with dehydroascorbic acid as a side product in stochiometric amount.

$$\begin{aligned}
Cu^{2+} + ascorbic\ acid + 1/2O_2 &\longrightarrow Cu^{1+} + dehydroascorbic\ acid + H_2O \\
2Cu^{1+} + O_2 + 2H^+ &\longrightarrow 2Cu^{2+} + H_2O_2 \\
Cu^{1+} + H_2O_2 + H^+ &\longrightarrow Cu^{2+} + {}^{\bullet}OH + H_2O \qquad (1.1) \\
C_6H_6 + {}^{\bullet}OH &\longrightarrow {}^{\bullet}C_6H_6OH \\
{}^{\bullet}C_6H_6OH + Cu^{2+} &\longrightarrow phenol + Cu^{1+} + H^+
\end{aligned}$$

This mechanism assumes that the Cu(I) ions are able to activate the oxygen molecules over the formation and dissociation of hydrogen peroxide. The so generated radicals would then react with benzene to a hydroxycyclohexadienyl radical which could reduce the copper ions to form phenol.

The phenol production in the gas phase by direct insertion of oxygen into the benzene ring is an attractive and challenging method not only from a practical point of view but also from a synthetic chemical point of view because this is a very difficult oxygenation reaction due to the energetically stable benzene. More than 100 years ago, Friedel and Crafts examined the conversion of benzene to phenol using oxygen. The experiments carried out in 1888 were conducted in the gas phase in the presence of aluminium chloride.[26] Later studies on different catalysts in both gas and liquid phase always gave small phenol yields and sometimes also poor selectivity. Thus it is not surprising that the direct oxidation of benzene to phenol using pure oxygen has been mentioned in literature as one of the "10 challenges for catalysis".[27]

CHAPTER 2

ZEOLITES

2.1 GENERAL INFORMATION

Zeolites are natural or synthetic crystalline aluminosilicates with a three-dimensional regular arrangement of oxygen linked TO_4 tetrahedra (T = tetrahedrally coordinated atom). The framework structure forms uniformly sized pores of molecular dimensions, which can host compensating cations, water or other molecules and salts. The size of the synthetic crystals is generally between a fraction of a micrometer and several hundred micrometers, with the diameter of the channels and cavities varying between 0.3 to 1.3 nm.[28] Preferentially, only molecules that fit snugly inside the pores are adsorbed, while molecules that are too large are excluded. The zeolites act thus as molecular sieves. In some places the Si^{4+} atoms are replaced by Al^{3+} atoms, generating negative charges in the framework. These are compensated by cations which can easily be exchanged, offering the possibility of changing the acidic properties of the zeolite. The negative charge of the framework increases the zeolites absorption capability and affinity for polar adsorbates and thus its efficiency as molecular sieve.

The structural formula of a zeolite is based on the crystallographic unit cell, represented by:

$$M_{x/n}\left[(AlO_2)_2\,(SiO_2)_y\right] \bullet H_2O \qquad (2.1)$$

where x and y are the total number of tetrahedra per unit cell, with y/x varying usually between 1 and 5 and between 10- and 100 for high silica zeolites.[29] The water can be removed reversibly by heat treatment, which leaves intact the crystalline structure of the zeolite permeated by the void pore structure, which can make up to 50% of the crystall volume. The framework is not a static structure, but rather flexible, responding to changes in temperature, pressure, sorbed molecules or exchanged cations by adjusting slightly its bond lengths and angles.

First zeolite synthesis started in the 19th century aiming the production of synthetic counterparts to naturally occurring zeolites. With time, many new structures were synthesized and characterized but the exact factors governing the crystallization process are still under study. Classically, the synthesis involves the solution mediated crystallization from an amorphous gel, containing a silica source and an alumina source in water under basic pH conditions. Cations can be added to the gel as their oxide, hydroxide or salts which then act as OH^- ion source, as electrolyte, as counter ion for the anionic framework, or as structure directing agents.[30]

2.2 THE ZSM5 ZEOLITE

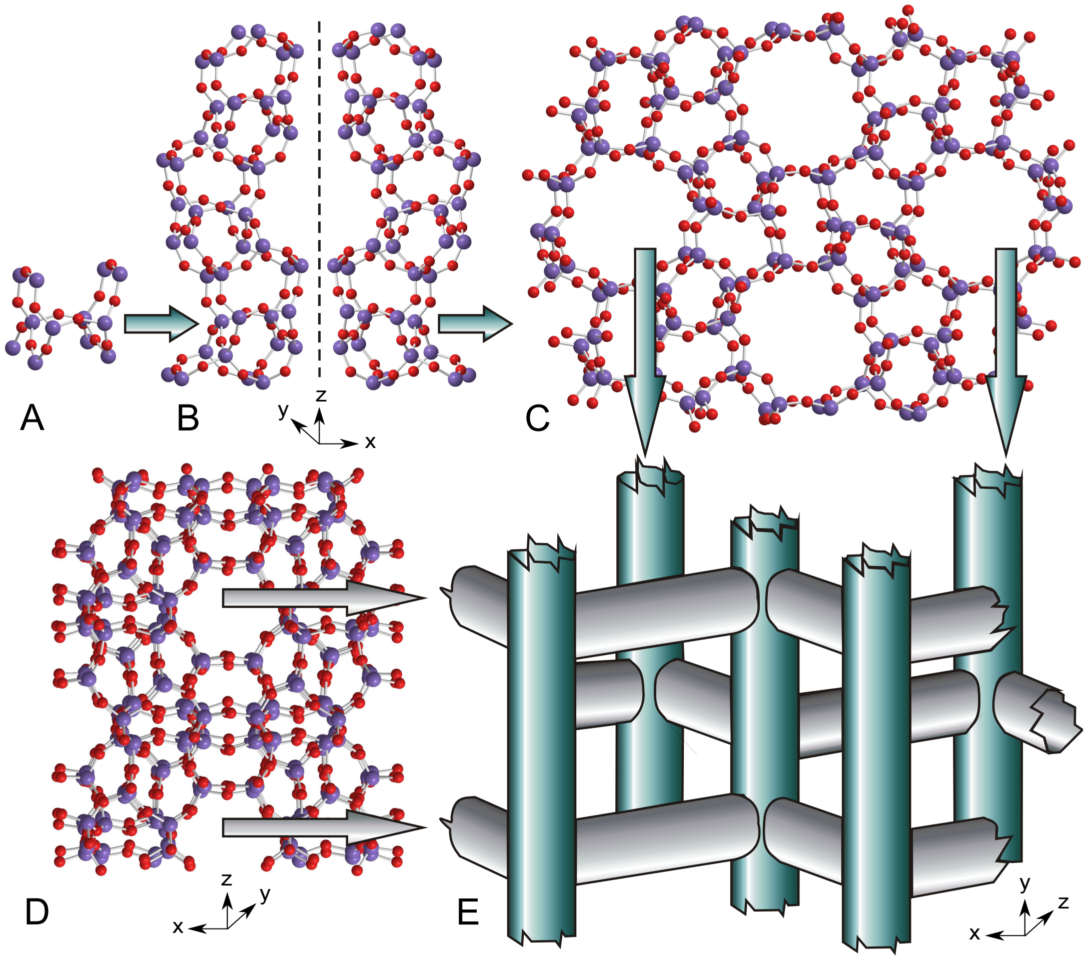

Figure 2.1: Scheme of the construction of the ZSM5 framework from pentasil units (A) linked to form chains (B). The resulting channel system (E) is sketched with the projections along the straight (C) and sinusoidal channels (D).

From the medium pore size materials, the pentasil materials, one of which is the ZSM5 zeolite, are the most interesting, due to their three-dimensional pore system. Pentasil units (figure 2.1 A) are linked by applying a two-fold screw axis parallel to z to form chains. The mirror images of these chains are connected by bridging oxygen atoms to form sheets with 10-ring holes (figure 2.1 B). Adjacent sheets are related to one another by an inversion center, creating thus straight 10-ring channels parallel to the corrugations (along y) and sinusoidal 10-ring channels perpendicular to the sheets (along x). The sinusoidal channels connect the straight channels to one another to form a three-dimensional channel system. With 12 T-atoms in the asymmetric unit, it is one of the most complex zeolite types known.[29] In figure 2.1 the ZSM5 zeolite is pictured as a scheme of the channel system (figure 2.1 E) and the projections along the straight (figure 2.1 C) and sinusoidal channels (figure 2.1 D). The straight channels have a diameter of 5.3×5.6 Å, the sinusoidal channels 5.1×5.5 Å.

Because the pore openings are 10-rings rather than 12-rings, the shape selectivity and catalysis is different from that of faujasites. The three-dimensional channel system leads to a better resistance to pore blocking through coke deposition. Mobil's methanol to gasoline process is one of the most important processes developed in the last years on ZSM5 zeolites.[31] Other processes include benzene alkylation with ethylene to produce ethylbenzene, the isomerization of xylene isomers to paraxylene[31], the dewaxing of gasoline, oligomerization of light olefins and the subsequent cracking of the products[30] and many more.

2.3 GENERATION OF ACID SITES

For an acid solid to convert an adsorbed basic molecule into its conjugated acid form, it must be able either to transfer a proton (these sites are called Brønsted sites) to the molecule, or accept an electron pair from it (Lewis sites). In zeolites both acid sites are present simultaneously. These sites are either hydroxyl groups which can eliminate a proton, or metal cations which can act both as electron acceptors and donors depending on their oxidation state. Since the inner surface of the zeolites is due to their pore system much larger than the outer surface, it is convenient to create the acid sites inside the channel structure. Having the reactive sites inside the pores offers also the possibility to use the molecular sieve properties of the zeolite and its shape selectivity for further reactions.

2.3.1 Generation of Brønsted Sites

Brønsted sites in zeolites must be able to transfer a proton to the adsorbed molecule. For this purpose OH groups containing mobile protons must be created on the surface of the channel system of the zeolite. There are four general methods for generating hydroxyl groups in zeolites.

1. The zeolites can directly be ion exchanged with diluted mineral acids like HCl, HNO_3, acetic acid etc:

$$\left(M^+Z^-\right)_{hydr.} + \left(H^+Cl^-\right)_{solution} \longleftrightarrow \left(H^+Z^-\right)_{hydr.} + \left(M^+Cl^-\right)_{solution} \tag{2.2}$$

   where M symbols the counterion used in the synthesis of the zeolite and Z symbolizes the SiOAl framework. Reaction 2.2 competes with the acid decomposition of the framework which is induced through the breaking of the SiO-Al bonds and the subsequent dealumination of the zeolite. Only zeolites with high Si/Al ratios can be thus treated this way.

2. The counterions can be exchanged with ammonium or alkylammonium ions followed by careful calcination, for too high temperatures can lead to dehydroxylation:

$$\begin{aligned}\left(M^+Z^-\right)_{hydr.} + \left(NH_4^+\right)_{solution} &\longleftrightarrow \left(NH_4^+Z^-\right)_{hydr.} + \left(M^+\right)_{solution}\\ \left(NH_4^+Z^-\right)_{hydr.} &\xrightarrow{\Delta T} \left(H^+Z^-\right)_{calcined} + NH_3\uparrow\end{aligned} \tag{2.3}$$

3. Water molecules can dissociate under the influence of the strong electrostatic field of multivalent cations leading to a partly dehydrated acid zeolite structure:

$$\left[M^{3+}\left(3Z^-\right)\left(H_2O\right)_n\right]_{hydr.} \longrightarrow \left[\left(2Z^-\right)M^{2+}\left(H_2O\right)\right]_{dehydr.} + \left(H^+Z^-\right)_{dehydr.} \tag{2.4}$$

   Ion exchange with high valence metals and subsequent calcination leads to the elimination of water from the metal hydrate shell.

4. Zeolites containing transition and noble metal ions can be reduced with hydrogen:

$$\left[Me^{2+}\left(2Z^-\right)\right]_{dehydr.} + H_2 \longrightarrow Me + 2\left(H^+Z^-\right)_{dehydr.} \tag{2.5}$$

   The metal remains on the zeolite surface and together with the framework oxygen atoms forms new Brønsted sites.

There are mainly three different types of hydroxyl groups: the terminal Si(OH) which cover and terminate the surface of the zeolite, bridging Si(OH)Al groups present inside the pore system and the hydroxyl groups of the extraframework aluminium. Their number and ratio can be controlled by the ion exchange method and temperature, but is limited by the Si/Al ratio of the parent zeolite.

2.3.2 Generation of Lewis Acid Sites

The simplest way to generate Lewis acid sites would be to prepare the metal ionic form of the zeolite. Each metal ion would than act as a Lewis site. By applying the method described by reaction 2.4 at high temperatures (> 773 K) complete dehydration needs to be achieved in order to obtain bare multivalent cations to compensate the negative charge of the framework:

$$\left[M^{2+}\left(2Z^{-}\right)\left(H_2O\right)_n\right]_{hydr.} \xrightarrow{\Delta T} \left[\left(2Z^{-}\right)M^{2+}\right]_{dehydr.} + H_2O\uparrow \qquad (2.6)$$

In the practice this situation can occur very rarely since for high Si/Al ratios, where the thermal stability is high enough, the distance between the negative charges is too long to allow such an arrangement, while for low Si/Al ratios which would allow charges closer to one another, the thermal stability is low.

Under high temperature conditions two Brønsted sites can convert through dehydroxylation into one Lewis acid center. The zeolite structure is damaged by the formation of an intermediate structure formed by a trigonal aluminium species and a positive silicon ion. The aluminium ion then leaves the framework as AlO$^+$ and can compensates the negative charge on the adjacent aluminium, becoming the "true" Lewis acid site.[30]

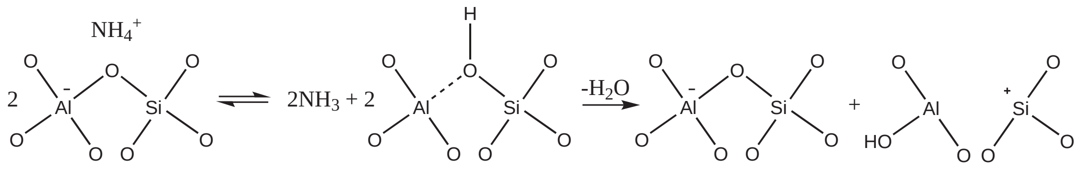

2.3.3 Metal Ion Exchange

The negatively charged framework of the zeolite enables the transport and exchange of the charge compensating cations. The ion exchange can be carried out in solid or liquid phase. The *liquid phase ion exchange* has the advantage that it can be performed on both the protonated form of the zeolite, where it exchanges the protons with cations similar to the reverse reaction 2.3 and on the metal form where it exchanges one metal cation with another.

$$N^{+a}_{solution} + aM^{+}Z^{-} \xrightarrow{\Delta T} N^{+a}Z^{-} + aM^{+}_{solution} \qquad (2.7)$$

with M the charge compensating cation (Na$^+$ or H$^+$) of the zeolite Z which is exchanged by a cation N of charge a. The ion exchange occurs usually at moderate temperatures while the solution with the suspended zeolite is stirred. The solvated ions enter the zeolite structure where they exchange the zeolitic cations which in return become solvated and diffuse out of the framework. The zeolite needs to be dried and calcined to remove water and other solution or organic residues.

Solid state ion exchange can be performed only on the protonated or ammonium form of the zeolite. The dry zeolite is grinded with the chloride salt of the metal that is to be exchanged. While heating up the mixture (temperatures between 573 and 1173 K) the cations are exchanged and HCl is gassed out (reaction 2.8). By the constant removal of HCl from the reaction equilibrium higher exchange ratios can be achieved than in the liquid ion exchange process. Another advantage of the solid state ion exchange process is the avoidance of the cation hydration effect, allowing thus the exchange of ions with high charge density or the use of small-pore zeolites.[29]

$$NCl_a + aH^+Z^- \xrightarrow{\Delta T} N^{+a}Z^- + aHCl \uparrow \tag{2.8}$$

Both methods can theoretically exchange cations of any charge. Practically the cation charge must be compensated by the framework, whose negative charges are given by the aluminium atoms. The Si/Al ratio is thus one of the major factors determining the ion exchange, not only by directing the cation location near an Al atom, but also by limiting the amount of ions that can be exchanged.

In the case of overexchange, when more cations are inserted into the zeolite structure than the number of Al atoms present in the framework, the exchanged cations will remain in their hydrated form and might agglomerate to form clusters or chains after calcination.[1,32] Overexchange is possible due to zeolite-internal framework SiO^- groups which were formed during synthesis and are retained after calcination.[28]

Besides the ion exchange of cations, metals can be introduced into the zeolite also by adsorbing neutral metal compounds or by impregnation. Zeolites with high Si/Al ratios favor the impregnation method if more metal ions need to be introduced in the zeolite than obtainable by ion exchange (when overexchange is desired) but the so obtained ion distribution is less uniform than in the case of ion exchange.[28]

2.4 COPPER EXCHANGED HZSM5

2.4.1 Cation Exchange Sites

A significant fraction of the studies of ZSM5 zeolites is designated to the analysis of their copper exchanged form, because of their use in many different reactions, e.g. the selective reduction of NO_x[33] or the direct oxidation of benzene to phenol by molecular oxygen.[1] The large ZSM5 unit cell offers many possibilities for copper exchange sites. In one unit cell there are 13 different six-rings, 11 different five-rings and one four-ring, all composed of different T-sites. Not all of the rings are truly accessible for cations, for example 5 of the six-rings are located inside the zeolite wall. The relevant sites which are geometrically distinct are pictured in figure 2.2:

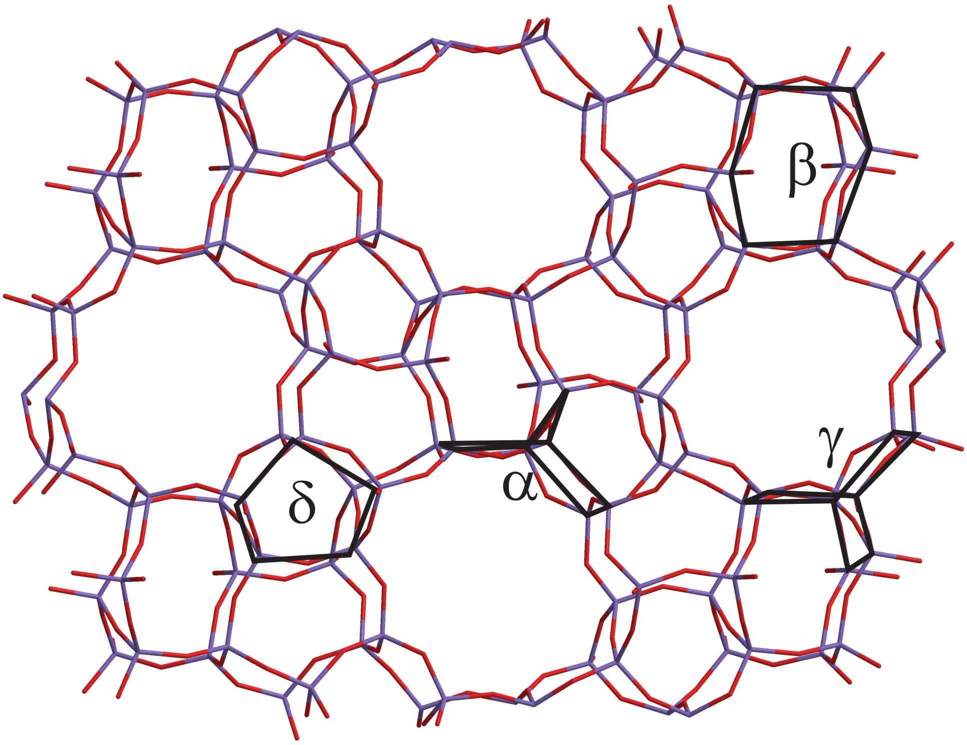

Figure 2.2: The ZSM5 structure with indication of the six-ring sites α, β and γ and the planar five-ring δ.

- Site α is a six-ring located at the surface of the straight channel and is composed of two fused five-rings which create an additional O-T-O bridge.
- Site β is a six-ring alongside the sinusoidal channel. Site γ is a planar six-ring with an additional O-T-O-T-O bridge positioned at the intersection of the channels.
- Site δ includes the planar five-ring of the sinusoidal channel.[34]

The large number of possible cation sites makes it imperative to study and determine the exact position occupied by the exchanged cation. Its location and coordination will have a strong impact on its reactivity and stability. Many studies were devoted to answering that question, either by means of photoluminescence[35], electron magnetic resonance (EPR)[36], X-ray absorption spectroscopy[37] or theoretical calculations.[34,38] Not only the location of the copper ion is essential but also its oxidation state. Ion exchange can directly insert copper ions in different oxidation states, Cu(I) or Cu(II), but air exposure, calcination or other treatments will alter their initial state. Exchanging ions of different oxidation states, might lead to the population of different sites as charge compensation has to be taken into account.

2.4.2 Charge Compensation

Isoelectronic substitution of Al for Si in SiO_4 tetrahedral (T) sites introduces negative charges into the zeolite lattice that are compensated by extra-lattice cations. Monovalent cations like Cu(I) can easily be hosted by the zeolite by coordinating to lattice oxygen adjacent to individual Al sites.[35,39] Divalent cations like Cu(II) or oxocations $(CuO_xCu)^{2+}$ are easily charge compensated by a pair of nearby Al T sites in zeolites with low Si/Al ratio, while for large Si/Al ratios charge compensation can be achieved by OH^- groups.[40,41] In particular overexchanged samples (Cu/Al>1) require exchangeable anions to balance the charge of higher-valent cations. In literature, mainly two types of oxocations can be found, both obtained through the dehydration of two $[Cu(II)(OH)^-]^+$ ions that are located close to one framework Al, to either isolated $Cu(II)O^-$ and Cu(I) plus H_2O[41,42] or to Cu(II)-O^{2-}-Cu(II) oxocations that can condense further under high temperature treatment to form Cu(I)$\cdots$Cu(I) pairs.[43–45] Double-O bridged Cu pairs were suggested to contribute to the NO decomposition[34,46] after density functional theory calculations had shown that they are highly stable in Cu/HZSM5.[38,40] These double-O oxocations were most stable for Cu-Cu separations of 2.5 and 3.5 Å.[47]

The feasibility of such $[CuO_2Cu]^{2+}$ complexes was supported by the statistical analysis of Al distributions and metal ion pairing probabilities.[38] For moderate Si/Al ratios of 23 the probability of an Al-substituted T site having an accessible Al neighbor at a distance between 4.3 and 8.5 Å is 0.65.[47] In part because of the close third-nearest-neighbor Al pairs[48] and in part because the five- and six-membered rings of ZSM5 tend to be more puckered, at a given Si/Al ratio, ZSM5 has a higher probability of short distance (<5.5Å) Al pairs than either ferrierite or mordenite. The copper oxocations supported by these close Al pairs also tend to be more puckered[38] and are likely more reactive than less strained oxocations. Further, the channel structure favors Al pairs that lie along one side of the channel rather than across it, making the oxocations more accessible for small molecules diffusing through the channel.[47] Meanwhile, NMR studies suggest that the Al distribution over the framework T-sites is neither random, as assumed for the theoretical calculations, nor controlled by a simple rule, but depends on the conditions of the zeolite synthesis.[49,50] The different sample preparation methods (starting zeolite type, ion exchange procedure, subsequent vacuum, gas and temperature treatment) lead to a large variety of different characteristics. This makes it very difficult to make a clear general prediction of the copper coordination and oxidation state.

CHAPTER 3

INFRARED SPECTROSCOPY

3.1 MOLECULAR VIBRATIONS

The molecular motions of a diatomic molecule can be described in a very simple way by two balls of mass m attached by a weightless string characterized by the spring constant *k*. This is the model of the classical harmonic oscillator, where the total energy depends on the maximum displacement and the kinetic and potential energy are constantly interconverted. The differential equation for the vibration can be obtained by introducing the distance between the atoms as internal coordinate *r* and μ the *reduced mass* defined as $\mu = m_1 m_2/(m_1 + m_2)$:

$$\mu \frac{d^2 r}{dt^2} + kr = 0 \tag{3.1}$$

The time dependent solution is given by equation:[51]

$$r(t) = r_{max} cos(2\pi\nu t + \varphi) \tag{3.2}$$

with the frequency of the resulting vibration:[51]

$$\nu = \frac{1}{2\pi}\sqrt{\frac{k}{\mu}} \tag{3.3}$$

The potential of a harmonic oscillator is described by a parabola. In reality the potential must by asymmetric towards the distance between the atoms, since the reduction of the distance will induce besides the attractive Coulomb forces also repulsive short range forces which hinder the collision of the atoms. The Morse function is frequently used as an approximation for an anharmonic potential (see figure 3.1):[52]

$$V = D[1 - exp(-\sqrt{k/2D} \cdot r)]^2 \tag{3.4}$$

where D is the *dissociation energy*. With increasing distance the attractive forces between the atoms approach zero and the potential energy reaches a boundary value, the dissociation energy. This simple classical concept must be broadened to a quantum mechanical model by applying the Hamilton operator H to the system and solving the time independent Schrödinger equation:[51]

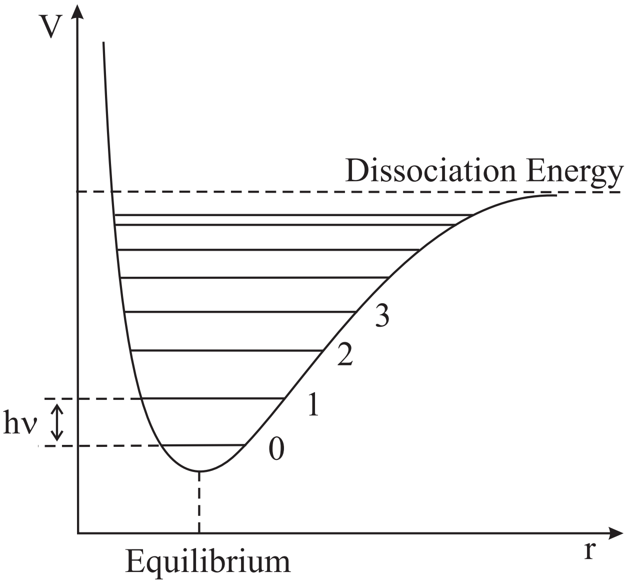

Figure 3.1: 1-Dimensional anharmonic potential and energy levels.

$$-\frac{\hbar}{2m}\frac{d^2\psi}{dr^2} + V(r)\psi = E\psi \tag{3.5}$$

with $\hbar$=h/2π is the Planck constant, ψ the eigenfunction and E the corresponding energy value of the system. For a one-dimensional harmonic oscillator the molecule can exist only in definite energy states, that are equidistant:

$$E_i = h\nu(v_i + 1/2) \qquad \text{with} \qquad v_i = 0, 1, 2, \ldots \tag{3.6}$$

while for the anharmonic oscillator the distances between the energy levels decrease with increasing energy:[53]

$$E_i = h\nu(v_i + 1/2) - \chi h\nu(v_i + 1/2)^2 \tag{3.7}$$

with χ the *anharmonicity constant*. The energy levels are numbered v_i, the *vibrational quantum number*. The potential energy has its lowest value at $v_i = 0$, which is not the energy of the potential minimum.[52] In spectroscopy, term values are generally used rather than energy eigenvalues of eq. 3.6:[54]

$$G(v) = \frac{E_v}{h \cdot c} = \tilde{\nu} \left(v + \frac{1}{2} \right) \tag{3.8}$$

3.2 VIBRATIONAL SPECTRA

From the time-dependent Schrödinger equation which describes the interaction of the oscillator with electromagnetic radiation one can derive the selection rules for the allowed energy transitions, namely $\Delta v = \pm 1$ for a harmonic oscillator and $\Delta v = \pm 1, 2, 3, \ldots$ for an anharmonic oscillator.[51] Transitions into higher terms than ± 1 have a decreasing probability and are called *overtones*. *Combination vibrations* occur when two or more different fundamental vibrations are excited simultaneously:

$$\nu_{combi} = a \cdot \nu_1 \pm b \cdot \nu_2 \pm c \cdot \nu_3 \pm \ldots \tag{3.9}$$

The *normal modes* of vibrations are computed out of the number of degrees of freedom of the molecule (N) without taking into account the translational and rotational degrees of freedom. The number of normal modes is then Z=3N-6. Some of these vibrations that inherently show the same frequency are called *degenerate*. It can also happen that various vibrational modes accidentally posses the same energy and are thus accidentally degenerate. When such a *Fermi Resonance* occurs, the actually weaker overtone can borrow intensity from the fundamental vibration so that two bands with similar intensities result.

3.3 MOLECULAR ROTATION

The rotation of the molecule can be described similarly to its vibration both by classical mechanics and quantum mechanics. Classically, the molecule is depicted as a rigid rotator and its energy is defined using the *moment of inertia* I and the angular velocity ω:

$$E_r = \frac{1}{2} I \omega^2 \tag{3.10}$$

with

$$I = \mu r^2 \qquad \text{and} \qquad \omega = 2\pi\nu_{rot} \tag{3.11}$$

where μ is the reduced mass and ν_{rot} the rotational frequency. The solution of the corresponding Schrödinger equation yields the discrete energy eigenvalues for a linear molecule:[51]

$$E_r = \frac{h^2}{8\pi^2 I} J(J+1) \tag{3.12}$$

The *rotational quantum number* J can take all positive integers as value starting with zero. In contrast to the vibrational state the molecule has no rotational energy in the ground state. The selection rule is $\Delta J = \pm 1$. According to eq. 3.12, the rotational term is defined as:[54]

$$F(J) = \frac{E_r}{h \cdot c} = \frac{h \cdot J(J+1)}{8\pi^2 c I} \tag{3.13}$$

with the rotational constant B:

$$B = \frac{h}{8\pi^2 c I} \tag{3.14}$$

3.4 ROTATION - VIBRATION INTERACTION

The molecules rotate and vibrate simultaneously, with the composed energy of the anharmonic oscillator and the non-rigid rotator. The influence of the centrifugal force leads to an increase of the interatomic distance and of the moment of inertia. Thus the frequency of the rotation ω is periodically changing in phase with the molecular vibration. As the total energy $E = E_r + E_i + E_p$ must of course remain constant, the energy in the vibrating rotor flows constantly between vibrational (E_i), rotational (E_r), and potential energy (E_p). The corresponding term value can be written as:[54]

$$\begin{aligned} T(v,J) = G(v) + F(v,J) = \nu \left(v + \frac{1}{2}\right) - \nu\chi \left(v + \frac{1}{2}\right)^2 \\ + B_v J(J+1) - D_v J^2 (J+1)^2 \end{aligned} \tag{3.15}$$

The rotational and vibrational constants can be written as:[51,54]

$$B_v = B_e - \alpha \left(v + \frac{1}{2}\right)$$

with

$$B_e = \frac{\hbar}{4\pi c I} \qquad D_v = D_e + \beta_e \left(v + \frac{1}{2}\right) \tag{3.16}$$

where D_e is the centrifugal constant and B_e is the rotational constant for the (hypothetical) vibration-free state. α and β are molecule-specific constants, with $\alpha \ll B_e$ and $\beta \ll D_e$.[53]

The same selection rules apply here as in the separate cases with the exception that $\Delta\nu = 0$ is allowed now for $\Delta J = \pm 1$. The fact that both $\Delta J = +1$ and $\Delta J = -1$ occur for each line series leads to an R-branch and a P-branch in the spectrum with a gap at the wavenumber of the prohibited, pure vibrational transition $\Delta J = 0$ known as the Q-branch. Due to the higher order terms in eq. 3.15 the lines in R- and P-branch are not equidistant. The lines in the P-branch drift apart with growing J, while the lines of the R-branch converge.

3.5 ISOTOPIC SHIFTS

Both vibrational and rotational energies depend on the masses of the atoms involved. Therefore, different isomers of a molecule have different term values T(v,J). From eq. 3.13 it is obvious that the rotational constant B_e is inversely proportional to the momentum of inertia, which is dependent of the reduced mass of the molecule (see eq. 3.11). The same is valid for the centrifugal constant D_e, while the vibrational constants contain following relations: $\nu \propto \sqrt{\mu}$ and $\nu\chi \propto \mu$.[54] Recording the spectra of different isotopes can be helpful to identify specific lines. The approximate frequency shift of a vibration of two different isotopic molecules A and B can be obtained from eq. 3.3:

$$\Delta\nu = \nu_A - \nu_B = \nu_A \left(1 - \sqrt{\frac{\mu_A}{\mu_B}}\right) \tag{3.17}$$

3.6 ABSORPTION OF INFRARED RADIATION

Through energy uptake a molecule can be excited to either vibrate or rotate around their state of equilibrium. Both the vibrational and rotational energies are quantized so that the molecule can absorb only energies which correspond to the energy needed for a transition from one energetic level to another:

$$\Delta E = h \cdot \nu \tag{3.18}$$

If the frequency of the electromagnetic radiation to which the molecule is exposed lies in the range of the IR radiation (between 780 nm and 50 μm or corresponding to wavenumbers of 12800 - 200 cm^{-1}) then the molecule can be excited to vibrate. If the energy of the radiation is lower, the molecule can only be induced to rotate (far-IR region: over 50 μm = below 200 cm^{-1}). The wavenumber cm^{-1} is proportional to the frequency and thus to the energy and inversely proportional to the wavelength:

$$\tilde{\nu} = \frac{1}{\lambda} = \frac{\nu}{c} \tag{3.19}$$

Radiation of the corresponding frequency can only be absorbed by a molecule if the excitation to a higher vibrational state is associated to a change in the dipole moment. If a dipole moment is not present from the beginning, those vibrations can be excited for which a dipole moment results from the antisymmetric displacement of the center of charge. Vibrations showing no change of the dipole moment are called infrared inactive. Here it must be noted that the symmetry of a molecule can be broken for example when it adsorbs on a substrate, causing forbidden bands to become IR active and degenerate bands to split.

3.6.1 Absorption of Radiation

A measure for the radiation absorption of a substance is the intensity of its bands in the IR spectrum. IR spectra can be taken either in transmission or reflection mode. In the transmission mode the radiation emitted by the light source is influenced only by the absorption by the sample. The *Lambert law* describes the decrease of the incident radiation intensity I_0 with its path through a material of thickness l, sliced into sheets of thickness dx:[51]

$$-\frac{dI}{dx} = \alpha I \tag{3.20}$$

Integration over the total thickness of the sample gives:

$$I = I_0 e^{-\alpha l} \tag{3.21}$$

where α is the *absorption coefficient*. By taking into account the influence of the concentration of the sample c on its radiation absorption capability the *Lambert-Beer law* can be obtained:[51]

$$I = I_0 10^{-\epsilon(\tilde{\nu})cl} \tag{3.22}$$

$\epsilon(\tilde{\nu})$ is the *extinction coefficient*, which is contrary to α independent of the sample concentration c. The extinction coefficient is a characteristic constant for every substance at a given wavenumber. A linear dependence of the absorption from the concentration can be obtained by introducing the *absorbance* A and *transmit-*

tance T:[51,53]

$$A = -log(T) = \epsilon(\tilde{\nu})cl \qquad \text{with} \qquad T = I/I_0 \tag{3.23}$$

Since absorption bands always spread over a certain frequency range the absorbance is better described by the integrated intensity of the band:[53]

$$A = \int \epsilon(\tilde{\nu})d\nu = \frac{1}{cl}\int log\left(\frac{I_0}{I(\tilde{\nu})}\right)d\tilde{\nu} \tag{3.24}$$

3.6.2 Line Profiles

There are several functions suitable for band fitting which depend on the band shape. When the line broadening is mainly caused by collision processes (*pressure broadening*), the profiles of rotational-vibrational bands can be fitted best by a *Lorentz function*:[51]

$$F_L(\tilde{\nu}) = \frac{A_{max}\Delta B}{(\tilde{\nu}-\tilde{\nu}_0)^2 + \Delta B^2} \tag{3.25}$$

with A_{max} the maximum band absorbance, ΔB the half width at half maximum and $\tilde{\nu_0}$ the wavenumber of the line center.

In the lower pressure region of gases, the *Doppler broadening* effect predominates, which is caused by the movement of the molecules compared to the observer. The center frequency will be shifted accordingly to the speed of the moving molecules and the band shape can be described by a *Gauss curve*:[51]

$$F_G(\tilde{\nu}) = A_{max} \cdot exp(\frac{-(ln2)(\tilde{\nu}-\tilde{\nu}_0)^2}{(\Delta B)^2}) \tag{3.26}$$

The Doppler broadening can exceed the natural line broadening by two orders of magnitude. The final line profile is given by the convolution of all broadening profiles including the apparatus profile.

3.7 FOURIER TRANSFORM SPECTROSCOPY

Generally, infrared spectra are observed in absorption rather than emission. This can be traced to a number experimental subtleties. For example, the spontaneous lifetime of excited vibrational levels is rather long, and hence the excited molecule could diffuse away from the observation region before emitting a photon. There are mainly two conventional ways of measuring adsorption spectra in the IR frequency range besides the new technique of the Fourier-transform (FTIR) spectroscopy:[54]

- A monochromatic radiation source with tunable wavelength is used and the transmitted intensity is measured as a function of the wavelength, whereby the resolution is determined by the linewidth of the radiation source (if it is larger than the adsorption lines).

- A monochromator is used to disperse the radiation of a broadband radiation source that emits a continuous thermal radiation. An interferometer must be used in order to resolve the linewidth of the adsorption lines, with the monochromator being the limiting factor for the spectral resolution.

- A FTIR spectrometer is based on a two-beam interference in a modified Michelson interferometer. A continuous radiation source is used and the gained signals are the Fourier transform of the spectrum.

The use of a Fourier-transform interferometer has many advantages over a conventional grating spectrometer concerning the resolution, measuring time and the signal to noise ratio that will be discussed in detail later.

3.7.1 The Fourier Transform Spectrometer

In figure 3.2 is pictured the schematic diagram of a FTIR spectrometer with a Michelson interferometer. The radiation incident from the spectrally continuous radiation source is split by a semi-permeable beam splitter BS into two partial beams. These are reflected back to the beam splitter by a fixed (M1) and a movable mirror (M2) and are thus superimposed. The shift of the movable mirror causes a path length difference δ (called *retardation*) in the interferometer and thus a *phase difference* ($\Delta\varphi = \varphi_1 - \varphi_2$) between the two partial beams. With the mirror M2 moving continuously the change of the interference amplitude recorded by the detector is called *interferogram*. The principle can be elucidated for a monochromatic incident wave with the wavenumber $\tilde{\nu}$ and I_0 partial beam intensity. At the detector a time average of the intensity is recorded as a cosine signal obtained as a function of the phase difference of the two beams:[54]

$$I(\varphi) = I_0[1 + cos(\Delta\varphi)] \qquad \text{with} \qquad \Delta\varphi = 2\pi\delta\tilde{\nu} \tag{3.27}$$

Depending on the position of the movable mirror the two beams will either add or cancel each other out. For retardations δ=0,λ,2λ... constructive interference will occur while for δ=$\frac{\lambda}{2}$,$\frac{3\lambda}{2}$,$\frac{5\lambda}{2}$ ... destructive interference is observable. By the Fourier transformation of the detected interferogram I(φ) (or I(δ)) the spectrum S($\tilde{\nu}$) is

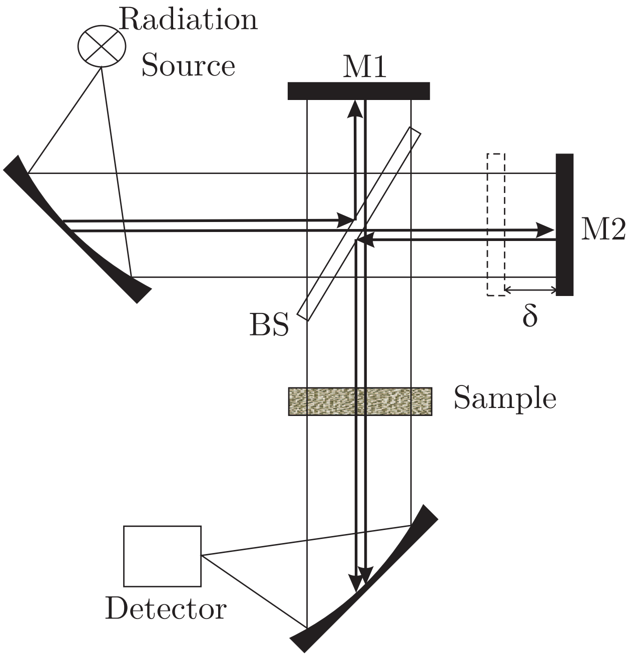

Figure 3.2: Sketch of a FTIR Spectrometer.

obtained with just one line at the wavenumber $\tilde{\nu}$ of the incident monochromatic radiation.

For spectrally continuous radiation the overlap of all the cosine functions of all wavenumbers is recorded by the detector. The Fourier transformation results in the spectrum of the radiation source:[51]

$$S(\tilde{\nu}) = \int_{-\infty}^{+\infty} I(\delta)(2\pi\tilde{\nu}\delta)d\delta \tag{3.28}$$

At $\delta = 0$ all waves are in phase and the maximum of the interferogram is reached, while for higher retardations destructive interference occurs and the signal intensity drops quickly. For the Fourier transformation the path length difference must be known precisely. In order to obtain a continuous path-time function with equidistant time markers, the interferogram of a frequency-constant He-Ne laser is recorded simultaneously to the one of the continuous radiation source.[54]

The advantages of the FTIR spectroscopy are now clear, since the complete spectral range transmitted through the spectrometer is recorded simultaneously, decreasing thus the measuring time and the signal-to-noise ratio (Fellgett-Advantage). The spectral resolution can be adjusted by the path length difference. The resolution of an FTIR spectrometer is equal to that of a grating spectrometer with a grating as large as half the path length difference in the Michelson interferometer. Conventional spectrometers have a very narrow entry slot following the radiation source. Because of the much larger circular opening of FTIR spectrometers, these have a much higher radiation throughput and two order of magnitude higher optical conductance (Jacquinot-Advantage). Because the frequency scale of the instrument is linked to the He-Ne laser, which provides an internal reference, the wavenumber stability of the obtained spectra is much higher (Connes-Advantage).[51]

CHAPTER 4

ELECTRON PARAMAGNETIC RESONANCE

4.1 THE ELECTRON SPIN AND MAGNETIC MOMENT

Elementary particles such as the electron are characterized by an intrinsic mechanical angular momentum called *spin*, which is controlled by the rules of quantum mechanics. The operator for the spin angular momentum is $\vec{S}$. The modulus of $\vec{S}$, the magnitude of the angular momentum, is the observable quantity:[55]

$$\left|\vec{S}\right| = \hbar\sqrt{S(S+1)} \tag{4.1}$$

where $\hbar$ is the Planck constant divided by 2π, S=$\frac{1}{2}$ is the *electron spin quantum number* and $\left|\vec{S}\right| = \hbar\sqrt{3/4}$. The eigenvalues for the projection of the angular momentum onto some specific direction (usually the axes of a Cartesian frame) are M$_S$, with

$$-S \leq M_S \leq +S \tag{4.2}$$

meaning for the electron that M$_S = \pm\frac{1}{2}$. The usual convention is to describe the components S$_Z$ along the z axis of the Cartesian frame, in $\hbar$ units of either 1/2 (α state or *spin up* (↑)) or -1/2 (β state or *spin down* (↓)).[56] In the absence of any particular preferential direction the spin states are degenerate.

Due to its spin (classically seen as a rotating charge), the electron possesses a *magnetic moment* $\vec{\mu_e}$ which is proportional to $\vec{S}$:

$$\vec{\mu_e} = \gamma\vec{S} = -g_e\mu_B\vec{S} \qquad \text{with the } \textit{Bohr magneton} \qquad \mu_B = \frac{e\hbar}{2m_e} \tag{4.3}$$

where $|e|$=1.6021·10^{-19} C and m$_e$=9.1093·10^{-31} kg[57] are the electron charge and mass and μ_B=9.2741×10^{-24} JT^{-1}. The negative sign indicates that for an electron, the magnetic moment is antiparallel to the spin. γ is the *magnetogyric ratio* which converts the angular momentum to the magnetic momentum. g_e is the electron g

factor (Landé factor) which for the free electron has the value 2.0023.[58]

4.2 ELECTRON SPIN IN A MAGNETIC FIELD: THE ZEEMAN EFFECT

Because of its magnetic moment $\vec{\mu_e}$ the electron interacts with an external magnetic field $\vec{B}$. The interaction energy can be written classically as:[56]

$$E = -\vec{\mu_e} \cdot \vec{B} \tag{4.4}$$

If $\vec{\mu_e}$ is replaced by the operator $\vec{S}$ (see eq. 4.3), the Hamiltonian for a free electron in a magnetic field is obtained:[58]

$$H = g_e \mu_B \vec{S} \cdot \vec{B} \tag{4.5}$$

If the axes are chosen such as the direction of the magnetic field (of magnitude B_0) runs along the z axis, the Hamiltonian becomes:

$$H_{ZE} = g_e \mu_B S_Z B_0 \qquad \text{with the eigenvalues:} \qquad E = g_e \mu_B B_0 M_S \tag{4.6}$$

Since $M_S = \pm\frac{1}{2}$ the difference between the two states which are degenerate in zero field, grows linearly with the magnetic field (see figure 4.1) and is called the *Zeeman splitting*. Generally for S>1/2 the magnetic quantum number $-S \leq M_S \leq +S$ leads to 2S+1 energy levels.

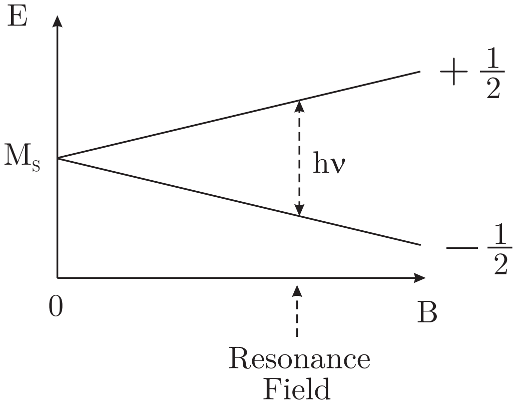

Figure 4.1: The electron Zeeman splitting of the M_S states of a S=1/2 system, at increasing external magnetic field.

Transitions between the two states are called spin inversions, and follow the selection rule $\Delta M = \pm 1$. Such a transition can be induced by the adsorption of electromagnetic radiation if it fulfills the *resonance condition*:[56]

$$h\nu = \Delta E = E_+ - E_- = g_e \mu_B B_0 \tag{4.7}$$

The energy difference between these levels corresponds to frequencies in the GHz range for magnetic fields from a few millitesla to several Tesla. The magnetic field of this radiation has to be perpendicular to the (z) direction of the external magnetic field ($\vec{B}$). The frequency of this radiation is:

$$\nu = g_e(\mu_B/h)B = \gamma_e B \tag{4.8}$$

with $\omega = 2\pi\nu$ the *Larmor frequency* of the spins precessing about $\vec{B}$.

4.3 SPIN-ORBIT COUPLING

When not a free electron is described but an unpaired electron of an atom or molecule, the orbital motion of the electron around the nucleus has to be considered too. The magnetic moment of the electron is then the sum of the contributions of the electron spin $\vec{S}$ and *orbital angular momentum* $\vec{L}$:[55]

$$\vec{\mu_L} = -\mu_B \vec{L} \qquad \text{and} \qquad \vec{\mu_S} = -g_e \mu_B \vec{S} \tag{4.9}$$

The modulus of $\vec{L}$ is quantized and may assume values similar to eq. 4.1 depending on the electron spatial wavefunction $\left|\vec{L}\right| = \hbar\sqrt{L(L+1)}$. The projection of $\vec{L}$ along z may assume 2L+1 quantized values $-L \leq L_Z \leq L$.

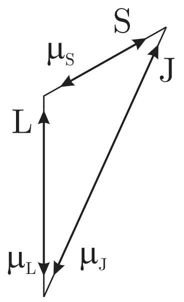

Figure 4.2: The vector addition of the orbital and spin magnetic moments.

The vector addition of the orbital and spin magnetic moments gives the *angular momentum* $\vec{J}$ which is antiparallel to the *total magnetic moment* $\vec{\mu_J}$ (see figure 4.2).

$$\vec{\mu_J} = -g_J \mu_B \vec{J} \tag{4.10}$$

By replacing the vectors by their lengths, where the length of the angular momentum is $\left|\vec{J}\right| = \hbar\sqrt{J(J+1)}$, the magnitude of the magnetic moment becomes:[58]

$$\mu_J = \mu_B \left\{ \frac{3J(J+1) + S(S+1) - L(L+1)}{2[J(J+1)]^{1/2}} \right\} \tag{4.11}$$

with the Land$\acute{e}$ factor:

$$g_J = \frac{3J(J+1) + S(S+1) - L(L+1)}{2J(J+1)} \tag{4.12}$$

This Land$\acute{e}$ factor is valid only for free atoms with a central potential.

The spin-orbit coupling partially restores the orbital angular momentum, even when it is formally quenched. It is a scalar magnetic interaction between the magnetic field generated by the orbital motion of the electron and its spin moment. The effect of the spin-orbit interaction can be described by the Hamiltonian:[58]

$$H_{LS} = \lambda \vec{L}\vec{S} \tag{4.13}$$

where λ is the *spin-orbit coupling constant*, for a particular shell in a particular atom.

The effect of the spin-orbit coupling is a deviation $\Delta g = g - g_e$ of the *g*-factor from the value of the free electron (see eq. 4.3). This leads to a shift of the resonance field intensity given by eq. 4.7. The shift of the *g*-value is large for metal complexes, where the electron moves in the proximity of a heavy atom nucleus, and very small for organic radicals which contain only light atoms. The amount of orbital character in the angular momentum is different for the different directions in a molecule fixed frame and the Hamiltonian 4.13 can be written as $H_{LS} = \lambda[L_X S_X + L_Y S_Y + L_Z S_Z]$. Therefor the value of *g* will depend on the direction of the magnetic field with respect to the molecular axes. The *g*-anisotropy will be discussed in more detail later.

4.4 HYPERFINE COUPLING

The nuclei are characterized by a spin angular momentum $\vec{I}$ and the associated magnetic moment μ_n:[55]

$$\mu_n = g_N \mu_N \vec{I} \qquad \text{with the } \textit{nuclear magneton} \qquad \mu_N = \frac{e\hbar}{2m_p} \tag{4.14}$$

with m_p=1.6726$\cdot 10^{-27}$ kg the mass of a proton and μ_N=5.0507$\times 10^{-27}$ JT^{-1}. The modulus $\left|\vec{I}\right| = \hbar\sqrt{I(I+1)}$ is quantized and the component along z can take values between $-I \leq M_I \leq I$. g_N is the nuclear *g*-factor, which for a proton is 5.5856.

The energy of the nuclear spin is influenced by an external magnetic field similar to the free electron. In analogy to eq. 4.6 the *nuclear Zeeman effect* gives the energy eigenvalues:

$$E_N = -g_N \mu_N B_0 M_I \tag{4.15}$$

The nuclear magnetic moment provides an additional magnetic field which influences the magnetic moment of the electron spin. This electron-nucleus spin interaction is called *hyperfine interactions* since it causes a splitting of the resonance EPR lines into 2I+1 components (see figure 4.3). The Hamiltonian for the hyperfine interaction is:

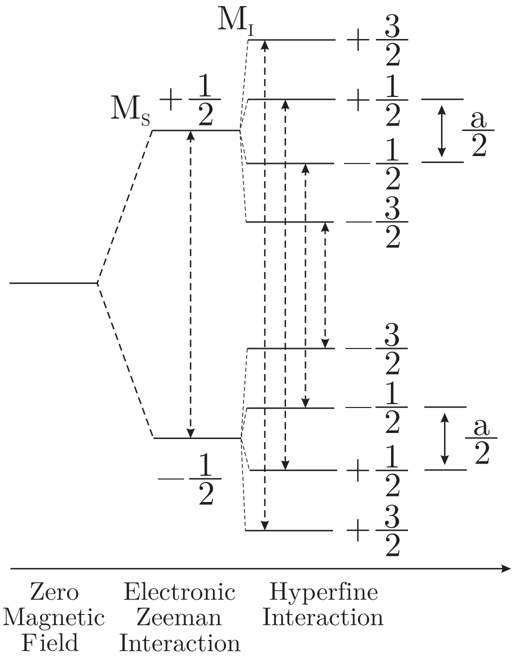
M_I
$+\frac{3}{2}$
M_S $+\frac{1}{2}$
$+\frac{1}{2}$
$-\frac{1}{2}$
$-\frac{3}{2}$
$\frac{a}{2}$
$-\frac{3}{2}$
$-\frac{1}{2}$
$+\frac{1}{2}$
$+\frac{3}{2}$
$-\frac{1}{2}$
$\frac{a}{2}$
Zero Magnetic Field
Electronic Zeeman Interaction
Hyperfine Interaction

Figure 4.3: Zeeman and hyperfine splitting of the energy levels of an atom with S=1/2 and I=3/2 like in the case of Cu^{2+}.

$$H_{HF} = \vec{I} \cdot \underline{A} \cdot \vec{S} \tag{4.16}$$

with $\underline{A}$ the *hyperfine coupling tensor*. By choosing the direction of the external magnetic field B_0 along the *z* direction of the principle axis system of the hyperfine tensor, only the diagonal elements of the tensor remain, which describe the tensor coupling of the two angular momentum vectors in the *x, y, z* directions.

When there is a coupling to more than one nucleus, the nuclear Zeeman and hyperfine interactions have to be summed over all nuclei. By virtue of the symmetry of the molecule some nuclei might be equivalent and can be treated as one nucleus with a total nuclear spin equal to the sum of the nuclear spins of the equivalent nuclei. The energy level scheme can be obtained by successive splitting of the levels for each interacting nucleus with the intensity of the EPR lines given for spin 1/2 species by the Blaise Pascal triangle.[57] For a benzene cation radical, which has 6 equivalent protons, the EPR spectrum contains thus 7 lines.

4.4.1 Contact Hyperfine Interaction

For the hyperfine field, the region external to the nucleus, where it can be described as the field of a magnetic dipole, must be distinguished from the region inside the nuclear volume. The dipolar approximation breaks down when the electron wave function $\Psi(r)$ is non zero at the nucleus, like in the case of s-states. Inside the nucleus the hyperfine field is constant, its energy being called the *contact* (or *Fermi*) contribution:[55]

$$E_{HF} = a\vec{S} \cdot \vec{I} \tag{4.17}$$

with a the *hyperfine coupling constant* that depends on the probability of the electron spin entering the nucleus:

$$a = (8\pi/3) g_e \mu_B g_N \mu_N \left|\Psi(0)\right|^2 \tag{4.18}$$

with $\Psi(0)$ the electron wavefunction at the nucleus.

4.4.2 Dipolar Hyperfine Interaction

The dipolar hyperfine interaction is an interaction between the magnetic moments of the electron and the nuclear spin. If the two moments are far apart their interaction can be treated in analogy to the classical dipolar interaction by calculating the energy of a magnetic dipole in the field of another at a point defined by a vector $\vec{r}$. For an atom with the nucleus at the origin the Hamiltonian becomes:[55]

$$H = g_e \mu_B \gamma \left\{ \frac{3(\vec{I} \cdot \vec{r})(\vec{S} \cdot \vec{r})}{r^5} - \frac{(\vec{I} \cdot \vec{S})}{r^3} \right\} \tag{4.19}$$

4.5 THE HAMILTONIAN

The energy of an atom containing an unpaired electron can be written as:[59]

$$H = \underbrace{H_{el} + H_{CF} + H_{LS}}_{\text{the atomic Hamiltonian}} + \underbrace{H_{SS} + H_{ZE} + H_{HF} + H_{ZN} + H_{II} + H_Q}_{\text{the spin Hamiltonian}} \tag{4.20}$$

with

H_{el} : electronic Hamiltonian
H_{CF} : crystal field Hamiltonian
H_{LS} : spin-orbit coupling Hamiltonian
H_{SS} : spin-spin interaction Hamiltonian
H_{II} : nuclear spin-spin interaction Hamiltonian
H_{ZE} : electronic Zeeman Hamiltonian
H_{ZN} : nuclear Zeeman Hamiltonian
H_{HF} : hyperfine interaction Hamiltonian
H_Q : quadrupole interaction Hamiltonian

(4.21)

The electronic Hamiltonian H_{el} is the sum of the kinetic energy of each electron, their potential energy relative to the nuclei and the interelectronic repulsion energies. The crystal field H_{CF} arises from the electrostatic charges and chemical bonds. The *spin-spin interaction* H_{SS} takes into account the dipolar interaction between the electron magnetic moments in two electron systems with the *nuclear spin-spin interaction* H_{II} the nuclear counterpart. H_{ZN} is the nuclear Zeeman term, the counterpart of the electronic Zeeman term H_{ZE}. The *quadrupole interaction* H_Q considers nuclei with $I \geq 1$ that have a non-spherical charge distribution. Not all the interactions can be observed by EPR spectroscopy depending on the element, molecular structure and physical state.

4.5.1 The General Theory for a Metal Ion

For a metal ion in a crystal field, the Hamiltonian can be written as:

$$H = \underbrace{E(r)_{kin}}_{\substack{Kinetic\\ Energy}} + \underbrace{V_0(r)}_{\substack{Potential\\ Energy}} + \underbrace{V_1(r)}_{\substack{Crystall\\ Field}} + \underbrace{\lambda \vec{L} \cdot \vec{S}}_{\substack{Spin-Orbit\\ Interaction}} + \underbrace{g_L \mu_B \vec{B_0} \cdot \vec{L}}_{\substack{Orbital-Zeeman\\ Interaction}} + \underbrace{g_S \mu_B \vec{B_0} \cdot \vec{S}}_{\substack{Spin-Zeeman\\ Interaction}} \tag{4.22}$$

The crystal field and the spin-orbit interactions are nearly always larger than the Zeeman interactions. Thus the magnetic moment is a small perturbation on the electronic problem. The magnetic properties have to be solved by perturbation methods after the solution of the electronic structure. With respect to the influence of the crystal field and the spin-orbit interaction, it must be distinguished which is stronger, the other one being then treated as a perturbation.

4.5.2 Transition Metal Ions

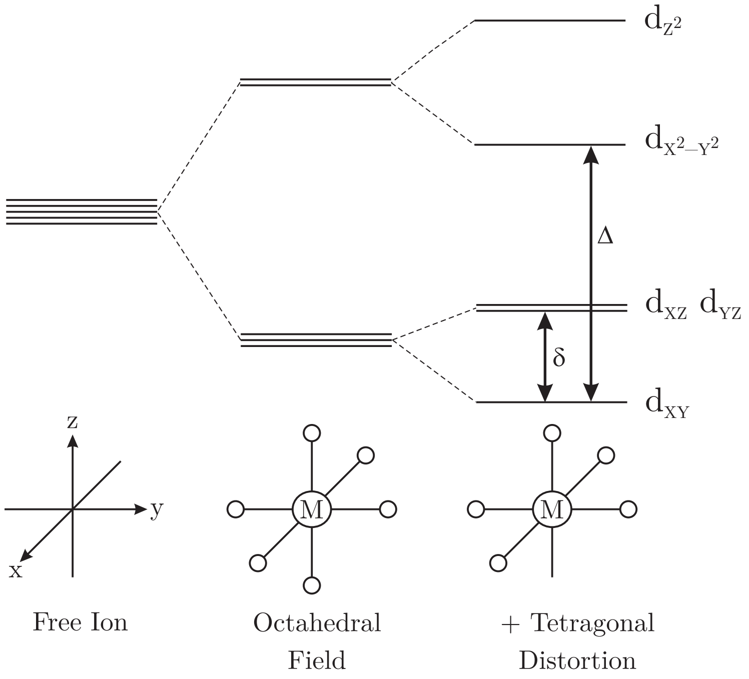

Figure 4.4: Level scheme for the d-orbitals in a tetragonally compressed octahedral crystal field.

In the case of light transition metal ions in solids, like the 3-d elements, the spin-orbit interaction is much weaker than the crystal field. In this case the crystal field problem is solved first and the spin-orbit interaction is treated as a perturbation. A qualitative understanding of the basic aspects can be achieved by considering the imposition of negatively charged ligands around the free ion, placed in a cubic array. For an octahedral arrangement, the five d functions split in two groups of energetically equivalent orbitals, the d_{XY}, d_{XZ} and d_{YZ} orbitals which are further removed from the negative charges and the d_{Z^2} and $d_{X^2-Y^2}$ orbitals. Often, there is a tetragonal distortion of the complex which leads to an additional splitting (see figure 4.4). The main effect is a g-shift proportional to the spin-orbit interaction λ and inversely proportional to the energy difference to the higher lying state. In case of an elongated tetrahedron the axial *g*-factors are:[57]

$$g_\perp = g_{XX} = g_{YY} = g_e - 2\frac{\lambda}{\delta}$$
$$g_\parallel = g_{ZZ} = g_e - 8\frac{\lambda}{\Delta} \tag{4.23}$$

4.6 *g*-ANISOTROPY

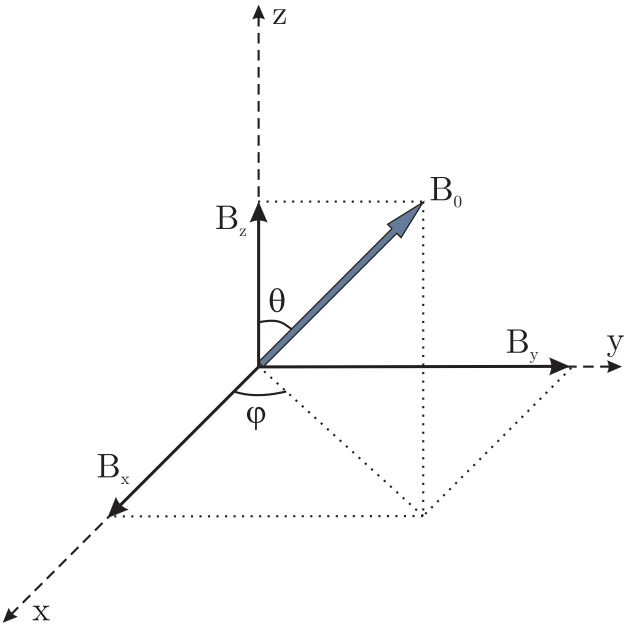

Figure 4.5: Direction cosines of the external magnetic field B_0.

The local symmetry of an unpaired electron center can lead to a anisotropy of the *g*-factor. By ignoring any hyperfine interactions the Zeeman spin Hamiltonian from eq. 4.5 becomes :[57]

$$H = \mu_B(g_{XX}B_X\vec{S_X} + g_{YY}B_Y\vec{S_Y} + g_{ZZ}B_Z\vec{S_Z}) \tag{4.24}$$

where *x,y,z* are the principal axes of an arbitrary Cartesian coordinate system fixed in the crystal, which give the principal axes of the *g*-tensor and the direction cosines c_X, c_Y, c_Z of the magnetic field B_0 (see figure 4.5):

$$\begin{aligned} B_X &= B_0 \cdot c_X = B_0 \cdot sin(\theta) \cdot cos(\varphi) \\ B_Y &= B_0 \cdot c_Y = B_0 \cdot sin(\theta) \cdot sin(\varphi) \\ B_Z &= B_0 \cdot c_Z = B_0 \cdot cos(\theta) \end{aligned} \tag{4.25}$$

The choice of suitable axes is crucial for being able to diagonalize the the *g*-tensor.

The effective value for g for an arbitrary orientation is then:

$$g_{iso}^2 = g_{XX}^2 c_X^2 + g_{YY}^2 c_Y^2 + g_{ZZ}^2 c_Z^2 \tag{4.26}$$

In the case of axial symmetry, with $g_\parallel$=g_{ZZ} along the symmetry axis z and $g_\perp$ = g_{XX} = g_{YY} perpendicular to it, eq. 4.26 becomes:

$$g_{iso}^2 = g_\perp^2 sin^2(\theta) + g_\parallel^2 cos^2(\theta) \tag{4.27}$$

In a single crystal, where the molecules have fixed orientations, the g anisotropy for the *x,y,z* axes can be measured by rotating the sample in the magnetic field. This is not possible for liquids where the fast molecular motion and tumbling averages out the anisotropy and only one g$_{iso}$ value can be measured. Powder spectra present a superposition of the EPR lines of all microcrystals.

4.7 ELECTRON EXCHANGE COUPLING

Spins of neighboring metal atoms or ions may exchange either through direct overlap of their orbitals or via overlap with intervening atoms. The latter is called *superexchange*. Included in the exchange interactions are the contributions from magnetic dipole-dipole coupling between unpaired electrons of the neighboring metal atoms, which for large interatomic distances can become the dominant contribution. The isotropic exchange interaction can be represented by:[60]

$$H_{Ex} = -J\vec{S}_1 \cdot \vec{S}_2 \tag{4.28}$$

Here negative J means a singlet (*antiferromagnetic*) lowest state, and a positive J indicates a high spin state (*ferromagnetic*) as having the lowest energy. Most dimeric complexes are antiferromagnetic. The electrostatic interaction is determined by the antisymmetry requirement of the Pauli exclusion principle which tends to align neighboring spins either parallel or antiparallel to each other. In most cases the spins are also coupled indirectly through spin-orbit interaction and are also affected by the surrounding ligands or lattice, which leads to anisotropic exchange where J is not a constant but a tensor.

4.8 MACROSCOPIC MAGNETIZATION

In a macroscopic system the *magnetization* is an ensemble average of all the magnetic moments over the sample volume. For individual, uncoupled spins this magnetization can be calculated easily. This is valid for nuclear spins even at high densities, while electrons couple strongly if they are close together. The *magnetic moment* per unit volume M of a sample which is exposed to an external magnetic field B_0 is connected to it by the *volume magnetic susceptibility* χ through $M = \chi B_0$. The *bulk magnetization* for a sample containing N spins can be calculated with the use of eq. 4.3 and 4.5 to:[58]

$$\langle M \rangle = \frac{g^2 \mu_B^2 S(S+1)}{3kT} N B_0 \cong \chi \frac{B_0}{\mu_0} \tag{4.29}$$

where μ_0 is the vacuum permeability. This $\chi_C(T) = \frac{C}{T}$ proportionality is called *Curie behavior*. Thus for a Curie paramagnet the temperature dependent $1/\chi$ curve will intercept zero.

If the exchange interactions between the magnetic moments of different atoms is taken into account, the susceptibility is given by the *Curie-Weiss* law, where Θ is the *Curie-Weiss temperature*:

$$\chi_{CW}(T) = \frac{C}{T - \Theta} \tag{4.30}$$

$\Theta > 0 \quad \Rightarrow T_C = \Theta$ ferromagnetic transition

$\Theta < 0 \quad \Rightarrow T_N = |\Theta|$ antiferromagnetic transition

The sign of Θ determines the transition type and magnetic behavior (see figure 4.6). A ferromagnet has a permanent magnetic moment. Below T_C the individual magnetic moments of the molecules are all lined up in the same direction and locked together giving rise to a very large magnetic moment. When exposed to an external magnetic field at constant temperature, the M(B) curve is not linear but shows a hysteresis curve. The temperature of the phase transition to the an-

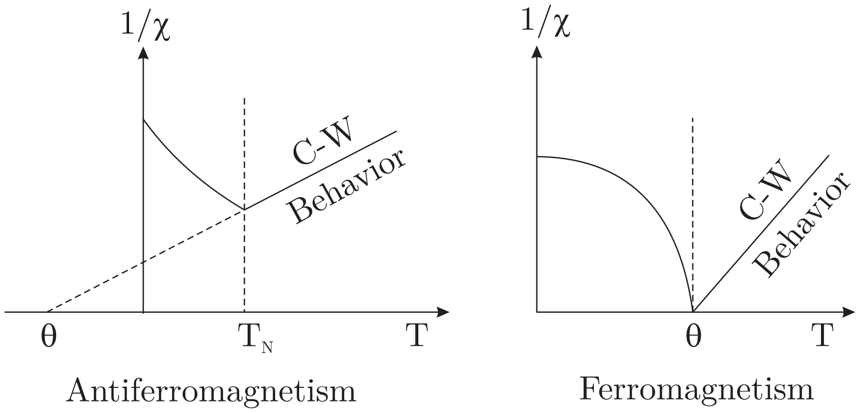

Figure 4.6: Inverse magnetic susceptibility as a function of temperature for a antiferromagnet and ferromagnet.

tiferromagnetic state is called *Néel temperature* T_N. Above this temperature the antiferromagnet exhibits paramagnetic Curie-Weiss behavior. The antiferromagnetic state is a long range order state with the adjacent magnetic moments aligned in opposite directions to each other. The moments of neighboring atoms cancel each other out resulting in relatively small total magnetic moments.

The change in the orbital motion of electrons caused by the applied magnetic field gives rise to a diamagnetic susceptibility which is negative and temperature dependent. *Diamagnetism* is a very small magnetization which opposes the magnetic field and is present in every matter whether it has paired or unpaired electrons. It has a low magnitude so that it is observable only in the lack of a paramagnetic susceptibility, which happens only when the total angular momentum is zero.

CHAPTER 5

EXPERIMENTAL DETAILS

5.1 SAMPLE PREPARATION

The catalyst samples were prepared by conventional exchange methods.[1,5] First, the commercially available NaZSM5 (CU Chemie Uetikon AG) was washed and calcined in air at 773 K for 10 h. The H-form of the zeolite was obtained by liquid ion exchange with aqueous 1 M NH_4NO_3 solution[1] followed by calcination in air at 673 K for 6 h (corresponding to eq. 2.3). HZSM5 samples with a Si/Al ratio in the range of 21 (4.5 Al atoms per unit cell (u.c.)) were used for further ion exchange. The Cu/HZSM5 zeolites were prepared either by liquid state ion exchange with aqueous 0.1 M $Cu(NO_3)_2$ solution of freshly calcined zeolite (see eq. 2.7) or by solid state reaction (see eq. 2.8) with CuCl in flowing N_2 (80 ml/min) at temperatures between 773 and 1273 K.[1] The solid state exchanged samples are labeled with the ion exchange temperature in Kelvin; a Cu/HZSM5 sample exchanged at 973 K is thus called ZSM973 while liquid ion exchanged samples are not labeled.

The physical properties of the samples determined by nitrogen adsorption are given in 5.1. The surface area and the volume of micropores were computed by the Dubinin-Radushkevic method[61] while the mesopore surface area was determined using the BET equation.[62]

The copper content of the discussed samples was determined by X-ray fluorescence and atomic absorption spectroscopy to 5 - 10 wt.% (4.7 - 9.5 Cu/u.c.) for solid state ion exchanged samples dependig on the ion exchange temperature (overexchanged up to a level of Cu/Al=1.5) and around 1.3 wt.% (1.2 Cu/u.c.) for liquid ion exchanged HZSM5 or NaZSM5 samples (Cu/Al=0.34). The copper content of the solid state ion exchanged samples does not show a simple, linear dependence on the temperature at which the ion exchange is performed but rather presents a maximum at 973 K.

Table 5.1: Physical properties of the samples determined from nitrogen adsorption isotherms

Sample	Micropore Properties	Mesopore Properties	Total Pore Volume
HZSM5	Area: 537 m^2/g Volume: 0.19 cm^3/g	524 m^2/g	0.37 cm^3/g
NaZSM5	Area: 397 m^2/g Volume: 0.14 cm^3/g	429 m^2/g	0.30 cm^3/g
CuNaZSM5	Area: 476 m^2/g Volume: 0.17 cm^3/g	464 m^2/g	0.29 cm^3/g
Cu/HZSM5	Area: 376 m^2/g Volume: 0.13 cm^3/g	397 m^2/g	0.29 cm^3/g
ZSM973	Area: 299 m^2/g Volume: 0.11 cm^3/g	312 m^2/g	0.21 cm^3/g

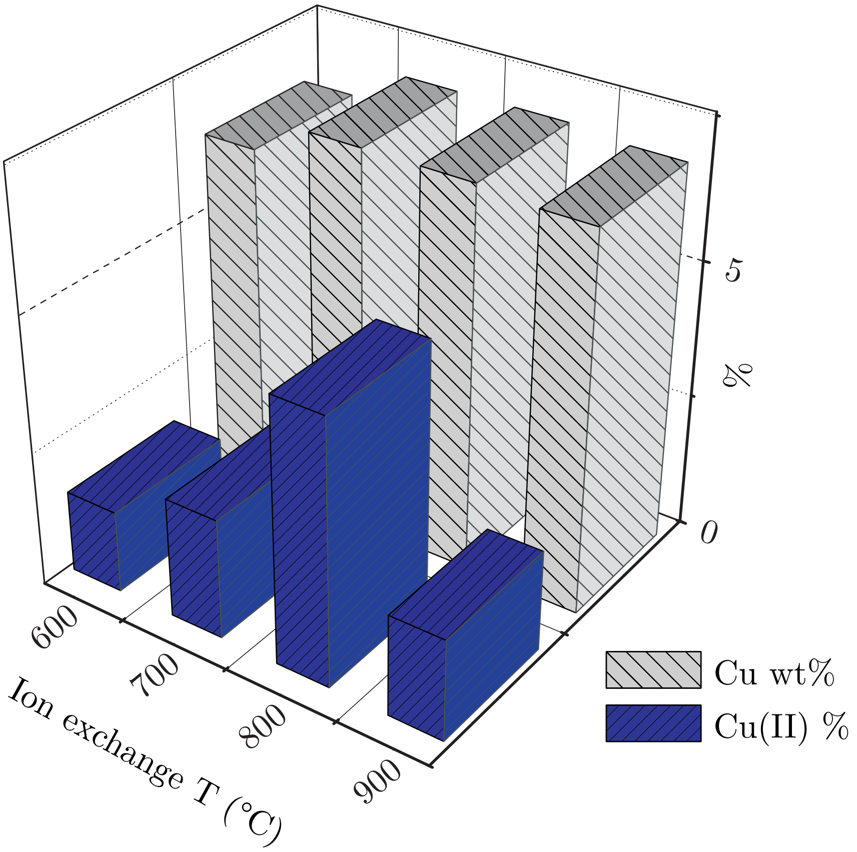

Figure 5.1: Amount of ion exchanged copper in weight percent and percentage of Cu(II) of the total amount of exchanged copper vs. the ion exchange temperature of the samples

5.2 FTIR MEASUREMENTS

Transmission FTIR spectra were recorded in the 400 - 4000 cm^{-1} range on a Nicolet Magna 560 spectrometer using a resolution of 2 cm^{-1} and 50 scans. Self-supporting, pressed zeolite wafers (about 10 mg/cm^2 for the measurements in the range of approximately 1300 to 4000 cm^{-1}) were prepared and placed into the transmission cell equipped with KBr windows. The cell can be evacuated or flooded with different gases and also heated up to 673 K or cooled down to 80 K.

In the range below 1300 cm^{-1} the absorption of lattice vibrations makes the zeolite essentially non-transparent. In order to be able to observe this spectral region too, the experimental setup was modified and the sample cell was placed upon a movable support. This enabled us to move the sample perpendicular to the optical path of the spectrometer, so as to observe only the very thin edge of the pellet (see figure 5.2). By monitoring the framework vibration bands in the spectrum while moving the cell, the proper position of the sample can be determined where these bands become transparent making the spectral region of the lattice vibrations, 400 to 1300 cm^{-1} observable.

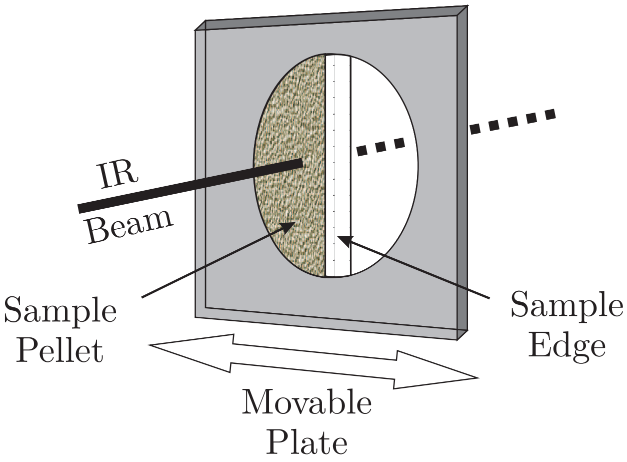

Figure 5.2: Sketch of the sample pellet mounted on a movable plate which enables to move the sample perpendicular to the optical path of the spectrometer, so as to observe only the very thin edge of the pellet.

The activation of the catalyst samples was performed in situ at 673 K for 16 h under vacuum. After the adsorption of the analysis gas, difference spectra of the samples were collected using the plain zeolite spectrum as a background. To allow the comparison of different samples, all the spectra were normalized to the sample's mass and plotted as absorbance per gram over the wavelength.

The pure oxygen gas was adsorbed at different equilibrium pressures at room temperature or 80 K. For the adsorption of benzene a septum inlet was built, to allow the controlled injection of very small benzene amounts by a microliter-syringe. At room temperature, the sample cell was filled with He up to normal pressure and the liquid benzene was injected into the admission line. A 5 minutes equilibration time was used after every injection. By monitoring the gas phase benzene IR lines we determined that this time is sufficient for the benzene gas to adsorb on the sample. A homogeneous distribution of benzene inside the sample is not reached from the beginning. For the ν_{13} C-C vibration band at 1480 cm^{-1} an extinction coefficient of 62±1 l/cm·mol[9] was used for calculating the amount of benzene truly adsorbed on the zeolite. The adsorption bands were fitted using Lorentzian lines.

5.3 EPR MEASUREMENTS

5.3.1 The EPR Spectrometer

Continuous wave electron paramagnetic resonance spectra were recorded with a X-band (9.46 GHz) Bruker EMX spectrometer. Continuous wave EPR records derivatives of absorption spectra by using a magnetic field modulation of 100 kHz with a modulation amplitude between 2 and 4 G. This particular method enjoys the advantages of narrowband detection at the modulation frequency and of better resolution of the derivative as compared to the absorption lineshape.

A helium-cooled Oxford EPR-900 continuous-flow cryostat was used for low temperature measurements. For temperature dependent magnetization measurements the cryostat was slowly warmed up from 3 to 250 K and the EPR spectra were recorded at each temperature after an equilibration time of 2-5 minutes depending on the magnitude of the temperature step. Special care had to be given to the temperature ramp during heating because of the magnetization hysteresis of the samples.

For room temperature measurements a double resonator was used, which allowed the successive measuring of the sample under study and the standard without having to tune the cavity between measurements. This allowed the spin density of the zeolite samples to be determined by the comparison with an ultramarine blue standard sample placed in the second microwave resonator. The general formula for calculating spin concentrations [X] using a standard sample of known concentration [Std] is:[57]

$$[X] = \frac{A_X \cdot R_X \cdot (Scan_X)^2 \cdot G_{Std} \cdot (B_m)_{Std} \cdot (g_{Std})^2 \cdot [S(S+1)]_{Std}}{A_{Std} \cdot R_{Std} \cdot (Scan_{Std})^2 \cdot G_X \cdot (B_m)_X \cdot (g_X)^2 \cdot [S(S+1)]_X} \cdot [Std] \tag{5.1}$$

with

A : area (double integral of signal)

R : integrated fraction of total spectrum

$Scan$: x-increment

G : gain of signal amplifier

B_m : modulation amplitude

This formula is valid if the same microwave power is used, the Q value of the cavity has not changed and the signal is not affected by saturation. If the other experimental parameters are held constant while measuring the sample and the standard, eq. 5.1 is simplified to:

$$[X] = \frac{A_X \cdot (g_{Std})^2}{A_{Std} \cdot (g_X)^2} \cdot [Std] \tag{5.2}$$

The Cu-spectra were recorded in the field region of 2450-3950 G, with 4 mW microwave power and 4 G modulation amplitude. The spectra of gas phase oxygen were recorded in the field region of 8000-9000 G, with 1 mW microwave power and 2 G modulation amplitude.

5.3.2 Adsorption Procedures

The Cu/HZSM5 samples were placed in suprasil EPR tubes and were evacuated at 573 K for 6 h prior to the measurements. The influence of oxygen and benzene was studied independently as well as simultaneously.

First both gases were added to the sample in amounts determined using a standard volume at a given pressure. The sample was cooled in liquid nitrogen in order to ensure that all the gas from the standard volume was adsorbed. In order to simulate reaction conditions both gases were adsorbed consecutively and before-and-after measurements were performed by heating the sample to 573 K for 2.5 h outside the spectrometer and measuring it only after cooling back to room temperature.

The stepwise adsorption measurements showed strong fluctuations in the samples spin concentration, which made it impossible to determine a clear oxidation or reduction trend or a saturation behavior. The fact that the adsorption was performed outside the spectrometer made the comparison of two successive adsorption steps unreliable because of two main reasons: the cavity had to be retuned for each measurement and with every movement the powder grains of the sample rearrange themself, changing the packing structure and density of the sample. In order to estimate the possible error in the spin concentration determination, a sample was measured repeatedly after moving it and retuning the spectrometer. The average error in the determined spin concentration was $2 \cdot 10^{18}$ spin/g. Thus a new setup was built for *in-situ* EPR adsorption measurements (figure 5.3). A pipe system was designed to allow a continuous gas flow through the sample of simultaneous and switchable helium, oxygen and benzene. A flow controller with 200 ml/min was used for the helium carrier gas and a flow controller with maximal 10 ml/min for oxygen. In order to obtain a constant benzene gas flow, helium was bubbled with maximal 10 ml/min through liquid benzene.

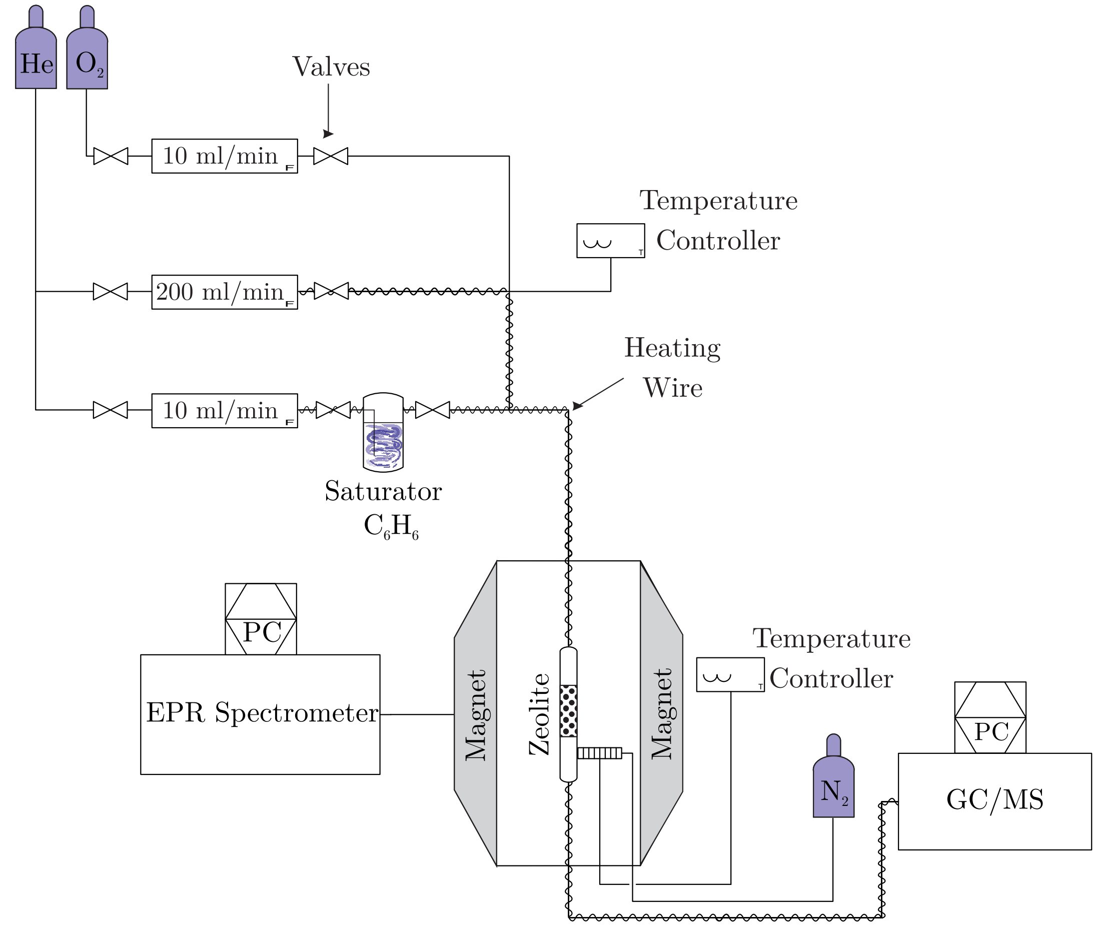
He
O_2
Valves
10 ml/min
Temperature Controller
200 ml/min
Heating Wire
10 ml/min
Saturator C_6H_6
PC
EPR Spectrometer
Magnet
Zeolite
Magnet
Temperature Controller
PC
N_2
GC/MS

Figure 5.3: Sketch of the experimental setup built for continuous flow EPR measurements.

The exact amount of benzene molecules the carrier gas is transporting can be computed by:

$$\frac{dn_B}{dt} = \frac{P_B}{p_0 - P_B} \cdot \frac{dn_C}{dt} \tag{5.3}$$

with the carrier gas molecular flow:

$$\frac{dn_C}{dt} = \frac{p_0}{RT} \cdot \frac{dv}{dt} \tag{5.4}$$

where dv/dt is the gas flow in ml/s, p_0 is the environment pressure (≈ 1000 hPa), T is the temperature and R=8.314472 J/(K·mol) the universal gas constant. dn_C/dt represents the number of carrier gas molecules per second that are passed through the saturator. With P_B=110 hPa the vapor pressure of benzene, the number of molecules which the carrier gas transports in case of complete saturation is then given by dn_B/dt.

The helium gas thus saturated with benzene was then directed towards the sample. Oxygen adsorption was performed at room temperature while for the benzene adsorption both the sample tube and the gas lines had to be heated up to 343 K and 373 K, respectively, to avoid condensation. The sample was always purged with a continuous He flow of 195 ml/min. In order to simulate reaction condition the sample was exposed to a continuous flow of benzene and oxygen while at 573 K.

The zeolite sample was evacuated at 573 K for 6 h prior to the measurements and transferred under inert gas conditions into a modified suprasil tube with a quartz wool stopper (see figure 5.4). This tube was placed in the double cavity resonator. The top end of the tube was connected to the gas pipe coming from the gas flow controllers, while the bottom was connected to a pipe leading to a gas chromatograph with a mass spectrometer detector. Both gas lines were wrapped with heating wire and isolating quartz wool band. A special quartz tube connected to a heater allowed the heating of the sample up to 573 K without the undesired simultaneous warming of the EPR cavity.

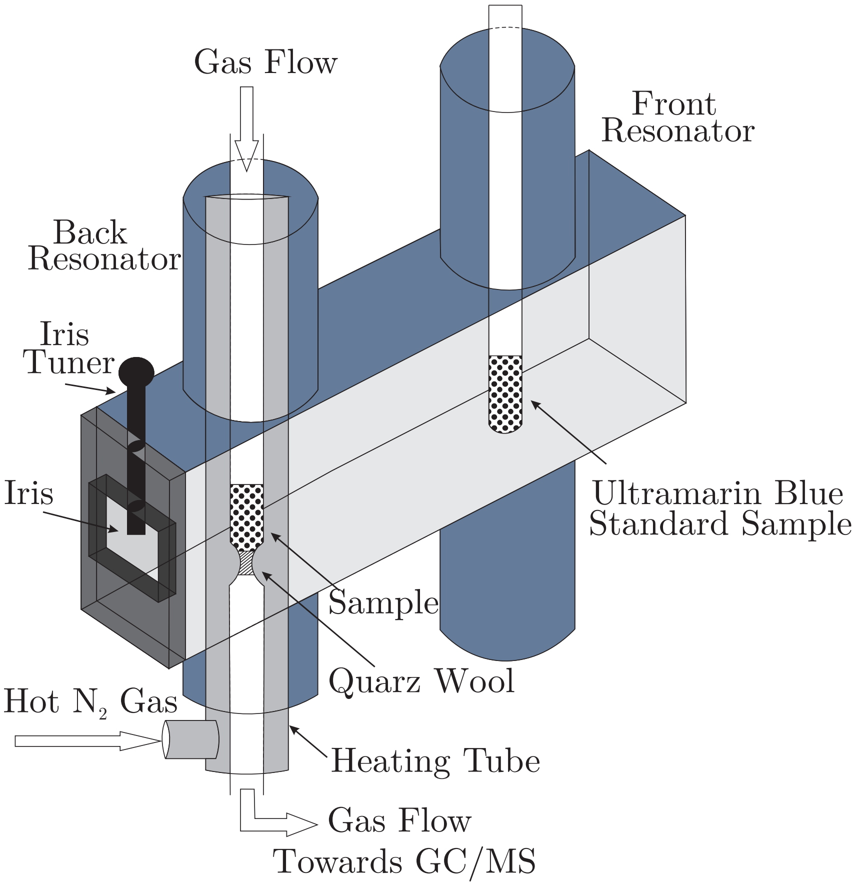
Gas Flow
Front Resonator
Back Resonator
Iris Tuner
Iris
Ultramarin Blue Standard Sample
Sample
Quarz Wool
Hot N_2 Gas
Heating Tube
Gas Flow Towards GC/MS

Figure 5.4: EPR double resonator cavity. The modified suprasil tube for continuous flow measurements is inserted with the heating tube in the back resonator. The standard sample is placed in the front resonator. The iris tunes the microwave for the whole cavity so that the same conditions exist in both resonators.

5.3.3 Numerical Simulations

For the numerical simulations of the Cu(II) paramagnetic species and the benzene radical cation the fine structure interaction was treated as a perturbation of the electron Zeeman level. Because the corresponding energy levels are then well-separated M_S becomes the main quantum number. The Matlab EasySpin package used for the simulations contains separate functions for simulating powder and radical spectra. Spectra are calculated over a triangular orientational grid. For each orientation line positions, and possible widths and intensities, are evaluated.

When calculating the spectra of powders, frozen solutions and single crystals each nucleus is treated independently and added afterwards to the spectra of the others. For the copper ions axial symmetry was used for the g and a anisotropy in the simulation.

Isotropic and fast-motional cw EPR spectra of doublet radicals in solution can be computed also, i.e., of spin systems with an electron spin S=1/2 coupled to an arbitrary number of nuclear spins I≥1/2 with small hyperfine couplings. In the case of the benzene radical cation, where the spin is given by a positive hole delocalized over the π ring, all the protons are equivalent and have the same hyperfine coupling constants. The same is valid for the carbon atoms, if the ^{13}C isotope is considered.

5.4 GAS CHROMATOGRAPHY MEASUREMENTS

Gas chromatography measurements were performed at a HP 6890, G1540A gas chromatograph equipped with a mass spectrometer detector MS 5973 and ion source 59864 B. The HP-1 Methyl Siloxane column of 60 m length and 250×0.25 μm dimensions, was purged with a 1 ml/min He flow. The oven was heated up to 473 K at a rate of 20 K/min.

The zeolite samples were washed in a 1:1 water and acetonitril mixture under stirring at room temperature for 12 h. The mixture was centrifuged and 1 μl of the overlaying liquid was injected into the gas chromatograph. The front inlet was used for the injection measurements. It was heated at 423 K and purged with 32 ml/min He gas in splitless mode. A solvent delay of 4.5 minutes was used in order to prevent filament burnout.

For the continuous flow EPR measurements, the gas flow purged through the EPR sample tube was conducted to the auxiliary 4 pressure controller of the gaschromatograph by means of a heated gas line (423 K). Valve 1, with a loop volume of 0.5 ml, was used for gas sampling. The injection time was set to 2 minutes, time in which the content of the sample loop is purged into the column. The chromatograms were taken at arbitrary times during the EPR measurements. No solvent delay was needed.

5.5 UV-VIS MEASUREMENTS

UV-Vis diffuse reflectance spectra were recorded on a AvaSpec 2048 spectrometer with a Ava-Light-DH-S light source from Avantes and a Oxford Electronics HP-SUV 1000 A optical cable at the Institute for Technical Chemistry, University of Stuttgart. The Cu/HZSM5 samples were placed in large suprasil EPR tubes (10 mm diameter) and were evacuated at 573 K for 6 h. Prior to the measurements the sample tubes were filled with nitrogen inert gas. The optical cable of the UV-Vis spectrometer was inserted into the sample tube and fixed just above the sample. The fixed sample was shielded from external light sources by a dark cover. A copper-free HZSM5 zeolite sample was used as background reference.

5.6 EXAFS AND XANES MEASUREMENTS

XAS measurements were performed at beamline E4 at the Hamburger Synchrotron Strahlungslabor (HASYLAB) under ambient conditions at 293 K. The detailed experimental and data evaluation procedures can be found in literature.[63] Since the copper loading of the liquid ion exchanged samples was an order of magnitude lower than that of the solid state ion exchanged samples, only solid state ion exchanged Cu/HZSM5 samples were analyzed. The solid samples were embedded in an oxygen-free cellulose matrix and pressed into pellets.

CHAPTER 6

INITIAL STATE OF THE CATALYST

The goal of our studies is the understanding of the gas phase oxidation of benzene to phenol using molecular oxygen. First, the initial state of the catalyst has to be fully known before the changes it undergoes during the reaction can be understood. In order to understand the effect that the adsorption has on the ion exchanged samples, we investigated the copper-free and copper-containing HZSM5 samples in their fresh form, directly after the ion exchange procedure. Since any subsequent gas treatment would change the initial state of the cations, only vacuum heat treatment was used for removing water and possible organic residues. Thus, we are starting our analysis one step earlier than most of the other published studies where the samples are analyzed in their fully oxidized form.[1,34,44,64–67]

6.1 FTIR SPECTRA

6.1.1 The Zeolite Framework Vibrations

The FTIR spectrum of a plain HZSM5 zeolite exhibits two main features: the signals of the zeolitic hydroxyl groups in the spectral range of 3750-3600 cm^{-1} and the signals of the framework vibrations below 2100 cm^{-1}. The lattice vibrations are so strong that below 1300 cm^{-1} all the IR radiation is adsorbed and the zeolite shuts (see figure 6.1 dashed line). In order to make the 1300-400 cm^{-1} spectral range observable, the experimental setup was modified to allow the moving of the sample perpendicular to the optical path of the spectrometer. By monitoring the spectrum while shifting the sample towards its edge, one can observe the loss of intensity as a function of the sample thickness. In figure 6.1 the spectrum series depicts the intensity loss while moving the sample from the position of its full thickness (dashed line) towards the edge (dotted line). With decreasing thickness the intensity of all the lines diminishes, making the spectral range of the lattice vibrations observable. Unfortunately at the same time the signal of the

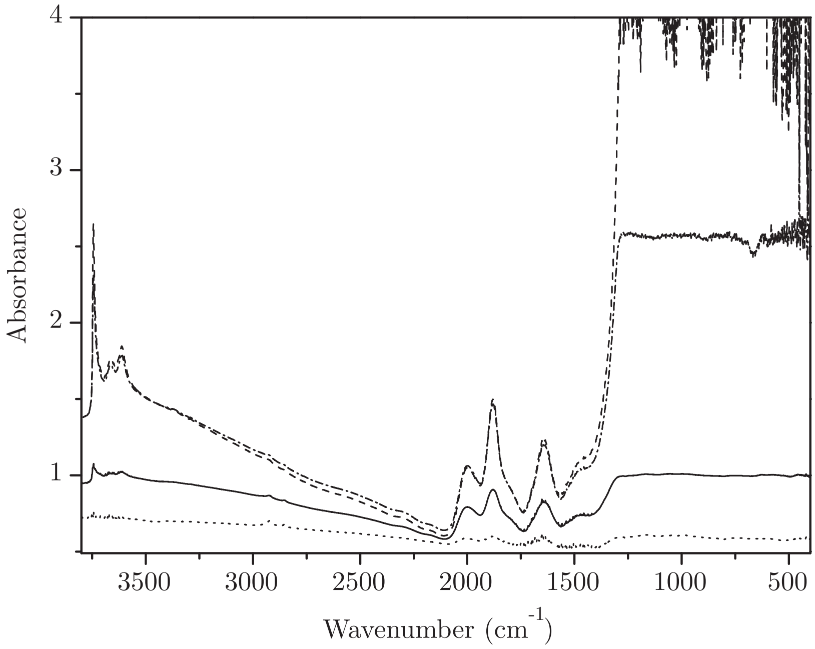

Figure 6.1: FTIR spectrum of a HZSM5 sample at different positions of the sample cell. The spectrum series depicts the intensity loss while moving the sample from the position of its full thickness (dashed line) towards the edge (dotted line).

zeolitic hydroxyl groups is lost. Thus, if all possible informations are to be gained from the 400 - 4000 cm^{-1} spectral range, both alignments (full sample thickness and sample edge) have to be studied for each sample.

6.1.2 The Hydroxyl Groups

The FTIR spectra of thick copper-free and copper-containing HZSM5 samples are identical for the 4000-1500 cm^{-1} spectral range, where the zeolitic hydroxyl stretching vibrations are observed (3750-3600 cm^{-1}). In figure 6.2 the different hydroxyl groups can be distinguished.[68,69] The terminal Si(OH) groups at 3745 cm^{-1} have with 18 cm^{-1} the smallest linewidth. Since they are located mostly on the outer surface of the zeolite crystals terminating the structure they are the most homogeneous. The internal Si(OH)Al groups at 3610 cm^{-1} with a line width of 27 cm^{-1} are more inhomogeneous. The signal of the extra lattice Al(OH) groups at 3664 cm^{-1} with a linewidth of 27 cm^{-1} is rather weak since the number of these sites is determined by the zeolite synthesis process. The position, line width and intensity of these bands will change if they interact with an adsorbate.

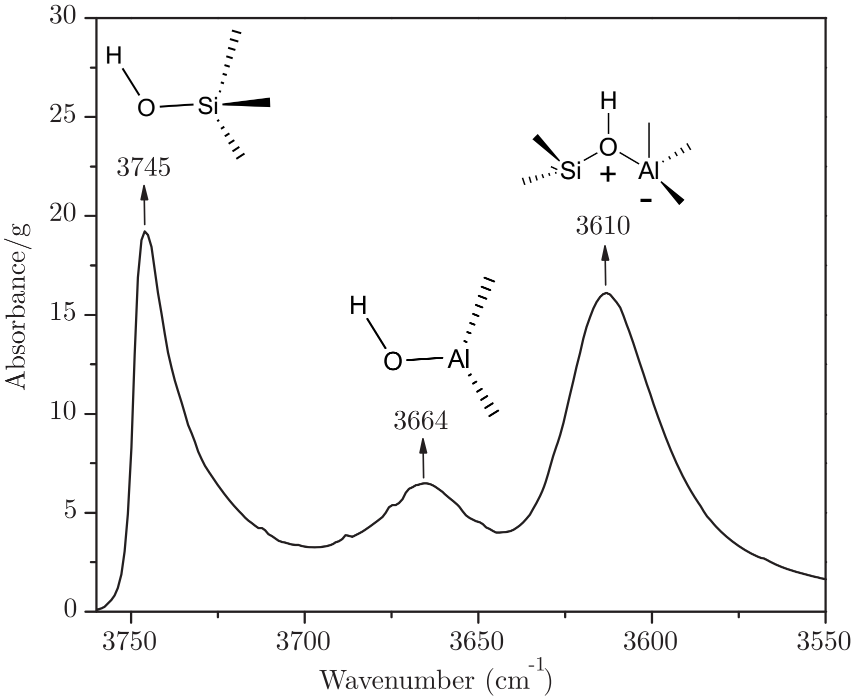

Figure 6.2: The spectral range of the hydroxyl groups of a HZSM5 sample.

6.2 EPR SPECTRA

6.2.1 *g*-Factor Assignment

The fact that the Cu(II) ions are the only EPR active species in the sample facilitates the analysis of the spectra. Thus the information about the surroundings of the ions and their interaction with other species can be obtained. Fresh samples present a mix of Cu(I) and Cu(II) ions. By calibrating the zeolite spectra against an ultramarine-blue reference sample the spin concentration of the sample can be computed via equation 5.2 and thus the amount of copper in the Cu(II) oxidation state. We determined that only 1-5% of the copper ions in the solid state ion exchanged samples were in the Cu(II) oxidation state, while in the samples prepared by liquid ion exchange 78% of the copper ions were Cu(II). Similar to the temperature dependece of the total copper content of the solid state ion exchanged samples, the percentage of copper present in its second oxidation state reaches a maximum at an ion exchange temperature of 973 K (see figure 5.1).

The hyperfine coupling between the 3d unpaired electron and the Cu(II) nuclear spin (I=3/2 for both, ^{63}Cu and ^{65}Cu isotopes, which are not resolved in the present experiments) causes the characteristic hyperfine splitting as described in chapter 4 figure 4.3. Figure 6.3 shows the EPR spectrum of a ZSM973 sample at room temperature indicating an axially symmetric environment with the hyperfine splitting observable on the parallel and the perpendicular components of

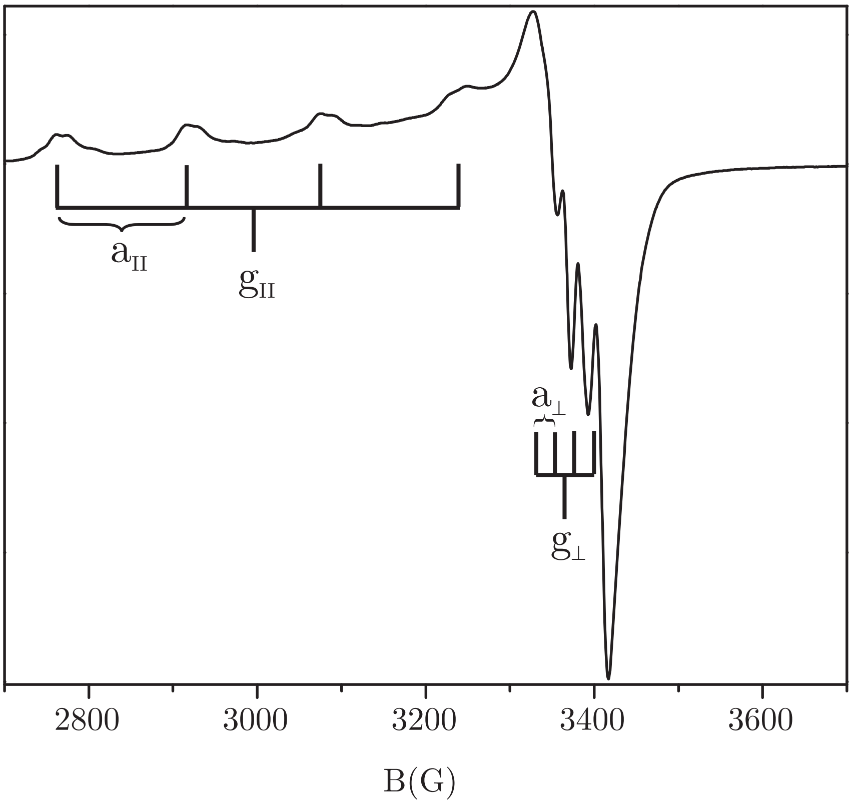

Figure 6.3: Cu(II) EPR spectra with general $g_{||}$ and $g_{\perp}$-factor assignment for a copper ion with axial symmetric coordination. The spectrum was taken with a ZSM973 sample at room temperature, but it is representative for all the samples independent of the ion exchange procedure

the g-factors. The sketch describes how the g-factors and the coupling constants should be read out of the spectrum if only one copper species would be concerned. Taking a closer look at the spectrum it becomes obvious that more than one copper species contributes to the signal.

Due to the overlap of the hyperfine splitting of the different copper species in the $g_{\perp}$ region, the corresponding signals could not be assigned precisely. In contrast, the $g_{||}$ region of the spectra is very well resolved. In all the samples we can distinguish two main signals with $g_{||}$ values of 2.31 ($a_{||}$=157 G) and 2.32 ($a_{||}$=156 G) (see figure 6.4), which had been assigned previously through theoretical calculations to square pyramidal Cu(II) species localized in positions $\alpha3$ and $\alpha4$ in a 6-ring on the channel wall.[67] The weak signal at $g_{||}$=2.28 ($a_{||}$=170 G) was assigned to square planar Cu-sites ($\gamma6$, a 6-ring positioned at the intersection of the two channels). Sometimes a very weak $g_{||}$=2.38 ($a_{||}$=123 G) signal remained from hydrated octahedral copper species if low evacuation temperatures were used.[35,36,67] The location of the α-, β- and γ-sites with respect to the zeolite pore structure is depicted in figure 2.2. The g-factors are influenced not only by copper entering one of these specific sites but also by the coordination geometry. This can be observed when comparing the symmetric $\alpha3$-site with the $\alpha4$-site in figure

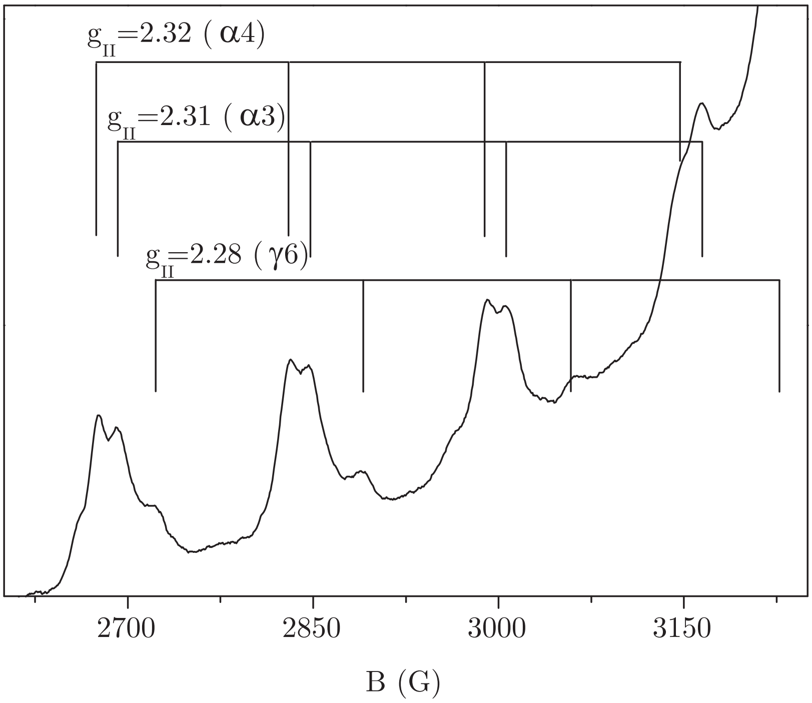

Figure 6.4: Parallel range of the Cu(II) EPR spectra with $g_{\|}$-factor assignment in Cu/HZSM5 zeolites at room temperature. The spectrum was taken with a ZSM973 sample, but it is representative for all the samples independent of the ion exchange procedure.

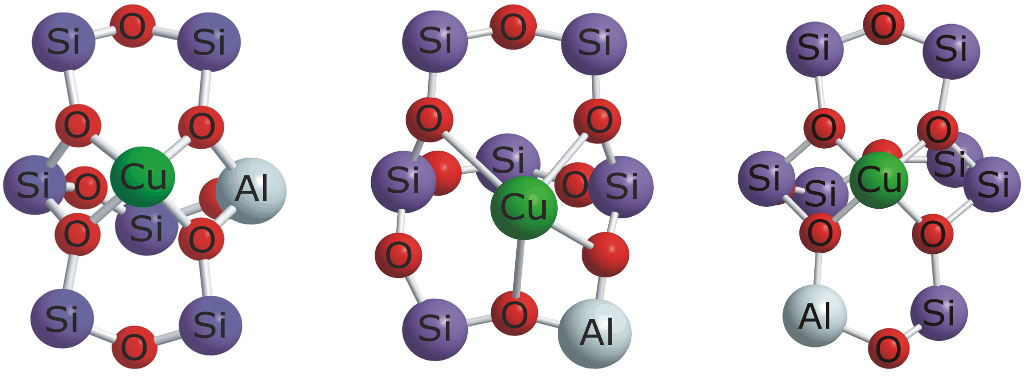

(a) $\alpha 3$ (b) $\alpha 4$ (c) $\gamma 6$

Figure 6.5: Structure of the (a)$\alpha 3$, (b) $\alpha 4$ and (c) $\gamma 6$ sites in Cu/HZSM5[67].

6.5(a) and 6.5(b).

The fraction of the three copper signals varies in the solid state ion exchanged samples with the exchange temperature. With rising exchange temperature the $\gamma 6$ signal diminishes compared to the fraction of $\alpha 3$ which remains mostly constant, while the fraction of Cu(II) localized in $\alpha 4$-sites rises dramatically (see figure 6.6).

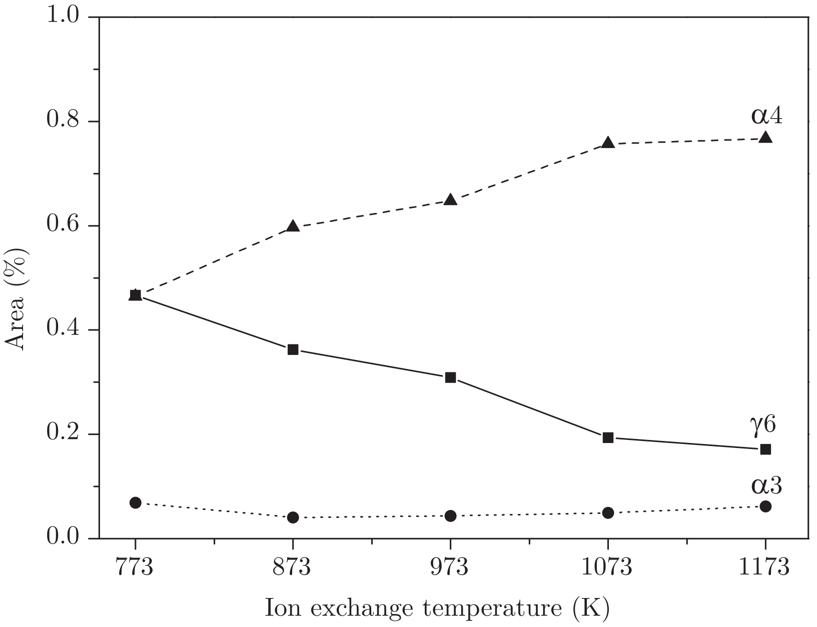

Figure 6.6: Fractions of the Cu(II) sites $\gamma 6$, $\alpha 3$ and $\alpha 4$ as determined from the $g_{\|}$ species assignment in solid state ion exchanged samples at different ion exchange temperatures, measured at room temperature.

6.2.2 Magnetization Plots

Temperature dependent EPR measurements were performed in order to determine the magnetic behavior of the samples. In figure 6.7 the reciprocal of the double integral of the spectrum was plotted against temperature for the ZSM973 sample. Both, liquid and solid state ion exchanged samples show antiferromagnetic behavior (see chapter 4 figure 4.6). Antiferromagnetic interactions can only exist if the copper atoms are located close to each other, for example in Cu-O-Cu units which permit coupling via superexchange over the oxygen bridge. One must distinguish here between a real bulk antiferromagnet where a long range order exists that defines the magnetic properties of the sample and the isolated antiferromagnetically coupled copper dimers. The dip in the magnetization plot does not describe the Néel temperature of the whole sample as would be the case for a bulk antiferromagnet but is related only to the copper dimers. Thus we do not speak of a Néel temperature in the classical way, but make use of the term to describe the copper dimers. The so called Néel temperature of the dimers lies between 25 and 30 K. Above this temperature all samples show Curie-Weiss behavior, proof of the presence of isolated paramagnetic copper ions. At lower temperatures the magnetization plot resembles a superposition of two antiferromagnetic curves with a second Néel temperature at 8 K. This suggests the presence of two antiferromagnetically coupled copper oxide species, one with the Néel temperature of 25 K (complex C1) and the second with the Néel temperature of 8 K

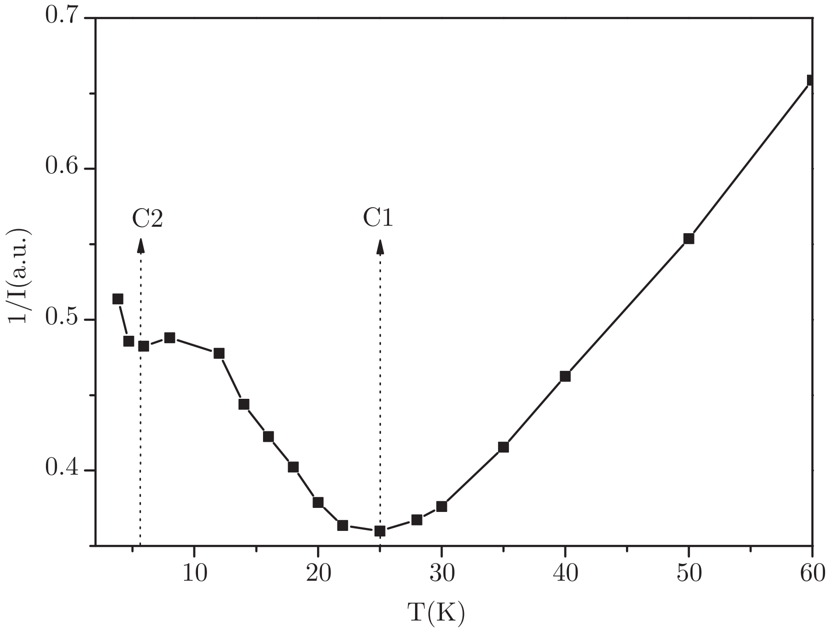

Figure 6.7: Magnetization plot of a solid state ion exchanged ZSM973 sample. The spectrum is representative for all the samples independent of the ion exchange procedure.

(complex C2). Together they make up 10% to 30% of the samples total copper content.

6.3 UV-Vis Spectra

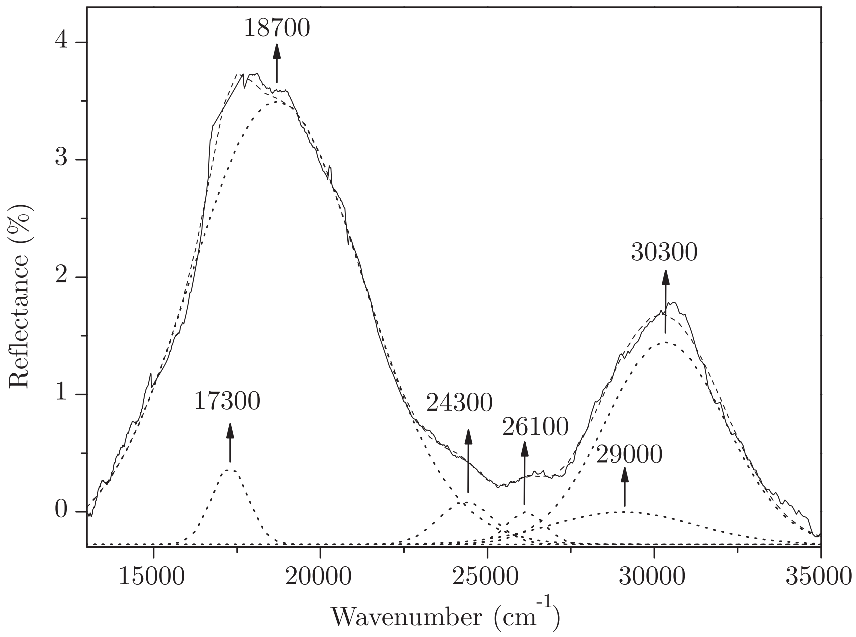

Figure 6.8: Diffuse reflectance UV-Vis spectrum of a fresh solid state ion exchanged sample (ZSM973) (solid line) and the deconvoluted dicopper peroxide bands (dotted lines).

Copper cores in enzymes and synthetic models have been extensively studied and characterized.[70–72] Diffuse reflectance UV-Vis measurements offer the possibility to distinguish between the different possible dicopper oxide complexes (see figure 6.9). The spectrum (figure 6.8) of a solid state ion exchanged ZSM973 sample is characterized by two broad bands at 18000 and 30000 cm^{-1}. The signals are composed of overlapping bands at 17300, 18700, 24300, 26100, 29000 and 30300 cm^{-1} which can be assigned according to literature (see table 6.1) to the planar and bent ($\mu - \eta^2 : \eta^2$-peroxo) and the bis(μ-oxo)-dicopper cores.[70–73] Despite the poor resolution of the bands, which hinders a clear differentiation of the planar and bent ($\mu - \eta^2 : \eta^2$-peroxo)-dicopper cores, the spectrum proofs undeniably the presence of both the ($\mu - \eta^2 : \eta^2$-peroxo) and the bis(μ-oxo)-dicopper complexes in the sample.

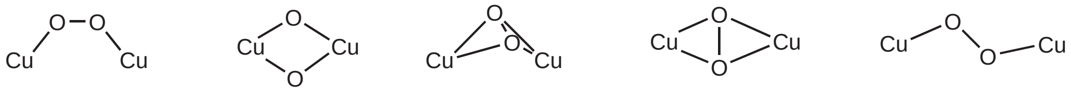

	Cu(cis-μ-1,2-O_2)Cu	Cu(μ-O)$_2$Cu	Cu(μ-η^2:η^2-O_2)Cu bent	Cu(μ-η^2:η^2-O_2)Cu planar	Cu(trans-μ-1,2-O_2)Cu
Cu-Cu	2.51	2.73-2.91	3.2-3.4	3.5-3.8	4.18
Cu-O	1.81	1.79-1.89	~1.92	1.7-2.2	1.81

Figure 6.9: Possible dicopper oxygen complexes in Cu/HZSM5 zeolites with the Cu-Cu and Cu-O bond distances in Å.[38,40,67,73]

Table 6.1: Summary of the structural and spectroscopic properties of the dicopper oxide complexes.[73]

	$[Cu_2(\mu - O)_2]^{2+}$ bis(μ-oxo) -dicopper	$[Cu_2(\mu - \eta^2 : \eta^2 - O_2)]^{2+}$ ($\mu - \eta^2 : \eta^2$-peroxo) dicopper planar	bent
Cu-Cu[a]	2.73-2.91	3.5-3.8	3.2-3.4
Cu-O[a]	1.79-1.89	1.7-2.2	
k_{max}[b]		17000-19800	≈18200
	22300-25000		20400-23800
	30800-32700	27300-29600	≈27800

[a] Interatomic distances in Å ; [b] Wavenumber of maximum absorption in cm^{-1}

6.4 EXAFS MEASUREMENTS

The solid state ion exchanged samples were studied by EXAFS, a courtesy of M. Bauer, and the spectra and results were published.[63] From the adjusted Cu-Cu coordination number it can be deduced that 10% of the copper centers are present as dimers, with a Cu-Cu separation of 3.34 Å. Considering the oxygen shell, the Cu-Cu shell could only be brought into accordance with a CuO_2Cu species[47], where both oxygen atoms of the dioxygen molecule interact with both copper centers. Combining the coordination numbers with the EPR assignments of the copper locations, it could be deduced that the monomeric Cu(I) centers of the sample prepared at 773 K could be found to 20% in the α3-, to 65% in the α4- and to 5% in the γ6-site.[67] For the sample prepared at 973 K the distribution of the Cu(I) centers differs, 20% in the α3-, 35% in the α4- and 40% in the γ6-site. This change is consistent with the one observed by EPR for the Cu(II) distribution over the α3, α4 and γ6-sites which is complementary to the Cu(I) distribution.

6.5 DISCUSSION

The samples contain a mixture of copper oxidation states: Cu(II) which can be observed by EPR and EXAFS and the EPR silent Cu(I) detectable only by EXAFS. By analyzing solid state ion exchanged samples prepared at different ion exchange temperatures, we were able to observe a trend for the copper oxidation states at the different single ion locations in the zeolite. The single copper ions reside at the α3- and 4-sites (planar six-rings with an additional O-T-O bridge located at the surface of the straight channels) and the γ6-sites (planar six-rings with an additional O-T-O-T-O bridge positioned at the channel intersections).[67] With rising ion exchange temperature the copper positioned at the γ6-sites is found mainly in the Cu(I) oxidation state while the Cu(II) amount in the α4-sites rises. For the α3-site the Cu(I)/Cu(II) ratio remains almost unchanged at different exchange temperatures. This means that the highest possible concentration of Cu(II) ions in the samples can be achieved at ion exchange temperatures of about 973 K, a fact confirmed by the EPR spin concentration measurements.

The large amount of EPR silent copper species consists of single Cu(I) ions (detectable by EXAFS) and oxocations. Groothaert et al.[34,46,67] assign the EPR silent species to the antiferromagnetically coupled bis(μ-oxo)dicopper core $[Cu_2(\mu\text{-}O)_2]^{2+}$ with a Cu-Cu distance of 2.87 Å.[34,46,67] Our samples present a larger Cu-Cu separation of 3.34 Å, corresponding to the calculated value for the bent ($\mu - \eta^2 : \eta^2$-peroxo)dicopper core isomer $[Cu_2(\mu - \eta^2 : \eta^2\text{-}O_2)]^{2+}$.[38,40,67] The low energy barrier between the two isomers suggests a facile pathway for the formation or cleavage of an O-O bond[38] which would be an important step for any oxidation reaction. Considering the fact that EXAFS only detects an average of all the Cu-Cu bond distances and that only 10% of the copper centers are present as dimers, the Cu-Cu separation of 3.34 Å could also be assigned to a mixture of the possible dicopper isomers (bis(μ-oxo), planar and bent ($\mu - \eta^2 : \eta^2$-peroxo) dicopper complexes). Goodman et al. were unable to identify an antiferroamgnetic state lower in energy than the ground (triplet) state neither for single nor for double oxygen bridged copper pairs.[38] Experimentally the antiferromagnetic coupling of these compounds has never been observed in the magnetic behavior of Cu/HZSM5 samples until now, because the measurements were performed at too high temperatures.[74]

In order to confirm their existence we performed UV-Vis measurements, which eventually permitted us to distinguish between the bis(μ-oxo)- and ($\mu - \eta^2 : \eta^2$-peroxo) dimers. The bands which would have allowed us to differentiate between the planar and the bent peroxo complexes were unfortunately not resolved so that we cannot make a clear statement about their relative abundance. Thus we have determined that in the fresh, untreated samples a mixture of individual copper units in the positions $\alpha 3$, $\alpha 4$ and $\gamma 6$ exists together with the bis(μ-oxo)- and planar and bent ($\mu - \eta^2 : \eta^2$-peroxo) dimers.

Since we now know the initial state of the catalyst, we can follow the changes which it experiences when oxygen and benzene are adsorbed.

CHAPTER 7

OXYGEN ADSORPTION

7.1 FTIR SPECTRA

7.1.1 The Hydroxyl Groups

Between the liquid and solid state ion exchanged samples, no relevant difference can be observed by means of FTIR, so that we will only differentiate between HZSM5 and Cu/HZSM5 independent of the preparation procedure. When oxygen is adsorbed on the zeolite the symmetry of the molecule is broken and the stretching mode at 1556 cm^{-1} becomes IR active, no matter whether the adsorption is side-on or end-on. Figure 7.1 shows the measured oxygen absorption spectra for the adsorption of both $^{16}O_2$ and $^{18}O_2$ isotopes at 80 K.

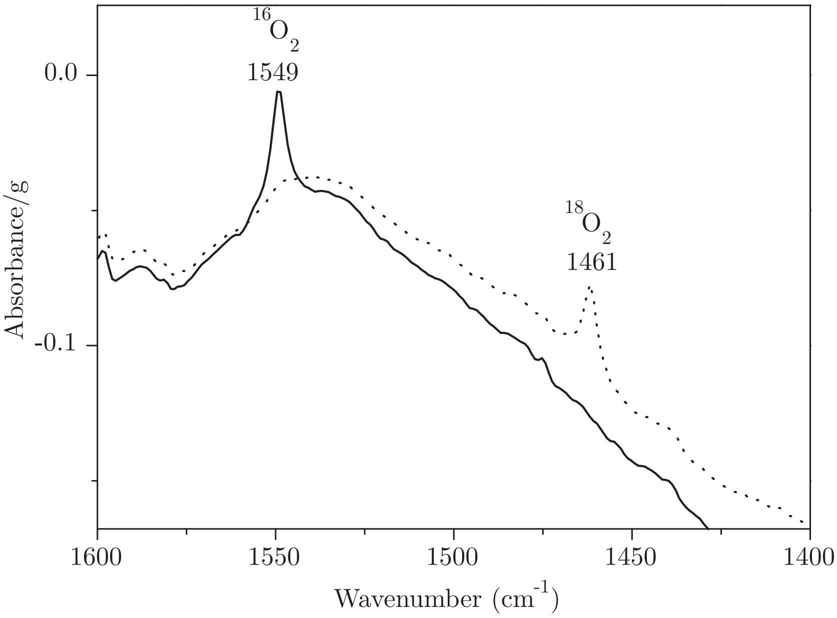

Figure 7.1: $^{16}O_2$ (solid line) and $^{18}O_2$ (dotted line) IR absorption bands after adsorption of 200 mbar equilibrium pressure of oxygen on Cu/HZSM5 at 80 K.

The frequency shift of -88 cm^{-1} between $^{16}O_2$ and $^{18}O_2$ corresponds to that expected for the free molecule considering the mass ratio of the isotopes (see chapter 3 equation 3.17). The frequency shift ($\Delta\tilde{\nu}$ = -7 cm^{-1}) from free dioxygen is too small to be explained by the adsorption on copper centers, which for Cu(I)/HY was predicted to arise near 1283 cm^{-1} for end-bonded oxygen at site II and near 1165 cm^{-1} for side-on bonded oxygen at site III.[75] When the spectra of oxygen adsorbed on Cu/HZSM5 and copper-free HZSM5 are compared, the same adsorption bands at 1549 cm^{-1} and 1461 cm^{-1} appear for $^{16}O_2$ and $^{18}O_2$, confirming that their origin does not lie in the copper oxygen interaction, but rather in the interaction with the Brønsted sites. Even though the small shift of the oxygen band compared to free gas phase oxygen indicates a weak bonding, the interaction is strong enough to be observed not only at 80 K, but also at room temperature.

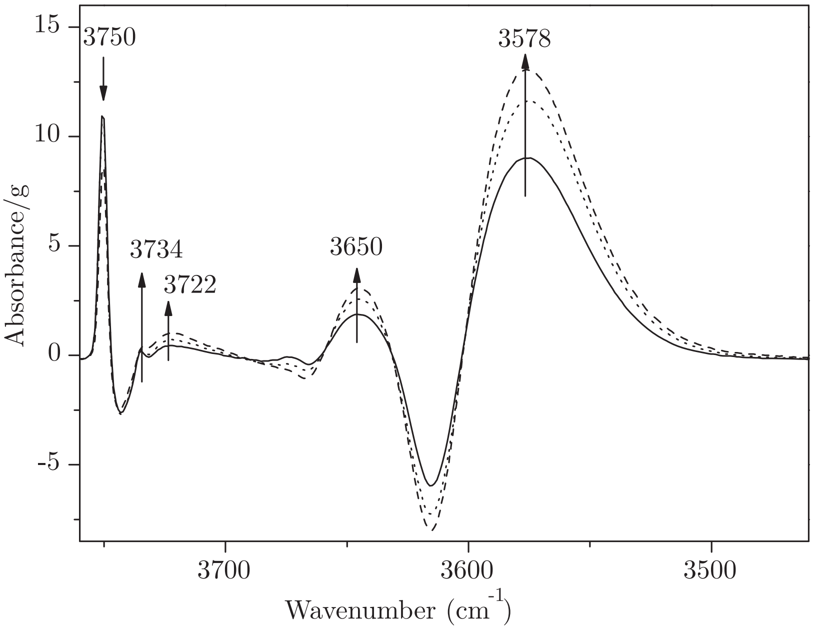

Figure 7.2: Difference spectra in the range of the hydroxyl stretching modes of Cu/HZSM5 during the adsorption of 20 mbar (solid line), 40 mbar (dotted line) and 200 mbar (dashed line) equilibrium pressure $^{16}O_2$ at 80 K.

According to literature[68,69] one can distinguish between the oxygen adsorption on the terminal Si(OH) groups (3745 cm^{-1}), internal Si(OH)Al groups (3610 cm^{-1}) and extra lattice Al(OH) groups (3664 cm^{-1}) (chapter 6 figure 6.2). On adsorption of oxygen, the vibration band corresponding to the terminal Si(OH) groups is blue-shifted by ($\Delta\tilde{\nu}$ = +5 cm^{-1}) and accompanied by the appearance of two weak bands at 3734 cm^{-1} and 3722 cm^{-1} as can be seen in figure 7.2. This small shift is independent of the oxygen pressure indicating a very weak interaction between the adsorbate and this groups. It has been discussed before that its origin lies either in the lowering of the sample temperature, which in our case was not observed, or in the frequency increase of the vibrational-rotational transitions by collision effects.[76] The adsorption line of the extra lattice Al(OH) groups is also red-shifted from 3664 cm^{-1} to 3650 cm^{-1} ($\Delta\tilde{\nu}$ = -14 cm^{-1}) and broadened by 13 cm^{-1} from a linewidth of 28 cm^{-1} to 41 cm^{-1}.

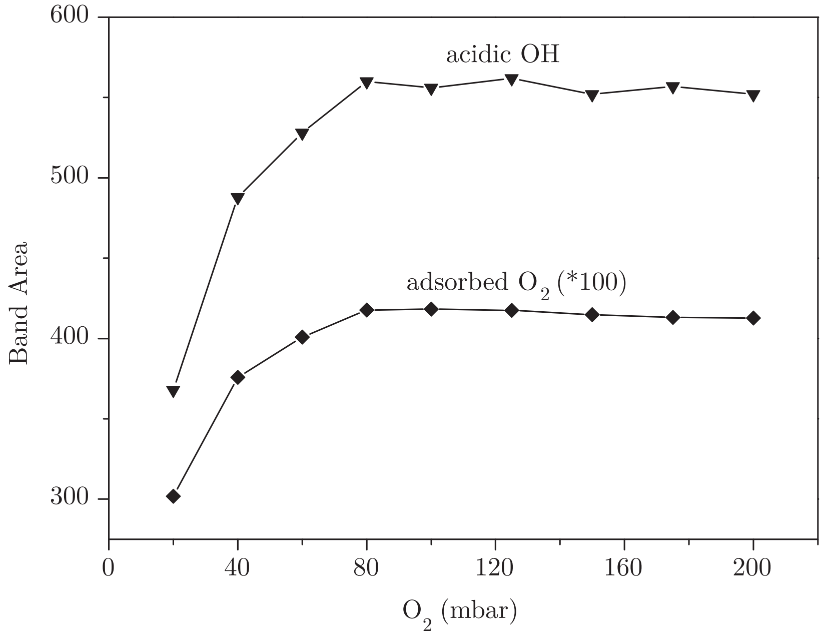

Figure 7.3: Integrated absorption of the $^{16}O_2$ adsorption band at 1549 cm^{-1} and of the hydroxyl groups of Cu/HZSM5.

The signal corresponding to the internal Si(OH)Al groups shows the strongest response to oxygen adsorption. It is red-shifted from 3610 cm^{-1} to 3578 cm^{-1} by ($\Delta\tilde{\nu}$ = -32 cm^{-1}) and broadened by 22 cm^{-1} from a linewidth of 27 cm^{-1} to 49 cm^{-1}. The large linewidth of these Si(OH)Al bands (figure 6.2 and 7.2) suggests that they have some inhomogeneity, which is then accentuated by the oxygen adsorption that causes the lines to broaden even more. This is not surprising if one considers the large number of different 5- and 6-rings located in a HZSM5 super-cell and the more or less random Al distribution. Steric hindrance could lead to a preferential oxygen adsorption on some hydroxyl groups and to different adsorption strengths, facts that could explain the growth and broadening of the acidic OH-signal. Consistent with this assumption is the behavior of the terminal Si(OH) groups, which are more homogeneous (initial linewidth of 16 cm^{-1}) and suffer little steric hindrance thus showing only a small shift and almost no broadening during the oxygen adsorption.

The integrated absorbance (band area) of the acidic hydroxyl group shows a linear correlation with that of the O_2 band at 1549 cm^{-1}, indicating the formation of the 1:1 H-bonded complex reported before.[77] In figure 7.3 the absorption integrated over the range (3660-3460 cm^{-1}) of the acidic hydroxyl group and of the oxygen adsorption line at 1549 cm^{-1} are plotted against the oxygen pressure showing the same saturation behavior.

The change in the zeolitic OH vibrations caused by the adsorbed oxygen is the same on both copper-free and copper-containing HZSM5, which is a clear evidence for dioxygen adsorption at these groups. Since the number of acidic OH groups does not change the observed behavior must mean that the transition dipole moment and thus the extinction coefficient is enhanced on oxygen adsorption. A model for end-on oxygen adsorption on the internal Si(OH)Al groups is plausible.[77] The same behavior was observed during the adsorption on Na containing ZSM5 zeolites, so these samples will be disregarded.

7.1.2 The Zeolite Framework Vibrations

In order to determine whether oxygen adsorbs not only on the Brønsted sites but also on the copper centers, it would be desirable to observe the stretching mode of the adsorbed oxygen. However, this band is strongly shifted against that of the free molecule, and therefore masked by framework vibrations. The ZSM5 zeolite possesses three major framework vibration types: external asymmetric stretching vibrations (1255 cm^{-1}), internal asymmetric stretching vibrations (1010 cm^{-1}) and internal symmetric stretching vibrations (825 cm^{-1}). The internal asymmetric stretching vibration is sensitive to the charge of the exchanged cation and shifts with the copper charge to 1025-1015 cm^{-1} for Cu(0), to 970-960 cm^{-1} for Cu(I) and to 915-925 cm^{-1} for Cu(II).[66,69,78]

For very thin wavers it may nevertheless be possible to observe the oxygen mode directly. In figure 7.5 three peaks are presented which appear after the oxygen adsorption on the copper-containing HZSM5 zeolite. The weak signal at 1161 cm^{-1} was assigned to a side-on bonded species described as a hybrid between Cu(I)-O_2 and Cu(II)-O_2^-, which maintains the small O-O separations and the triplet ground state characteristic of molecular oxygen. The calculated Cu-O distance is 1.94 Å.[40,75] An end-on bound copper-oxygen would be energetically less favorable by about 104 $kJ \cdot mol^{-1}$.[79] The rather weak signal at 1161 cm^{-1} was considered significant despite its low intensity which is of the same order of magnitude as the noise, due to its reproducibility in several measurements.

The oxidation of the ion exchanged copper to Cu(II) causes the internal asymmetric stretching lattice vibration to shift (figure 7.4) giving rise to a strong band at 915 cm^{-1}. The band around 850 cm^{-1} was assigned by means of theoretical calculations to a copper ($\mu - \eta^2 : \eta^2$)-peroxo complex Cu(II)-O_2^{2-}-Cu(II).[40] Such a complex can be formed from two individual Cu(II)-O_2^- species in close proximity

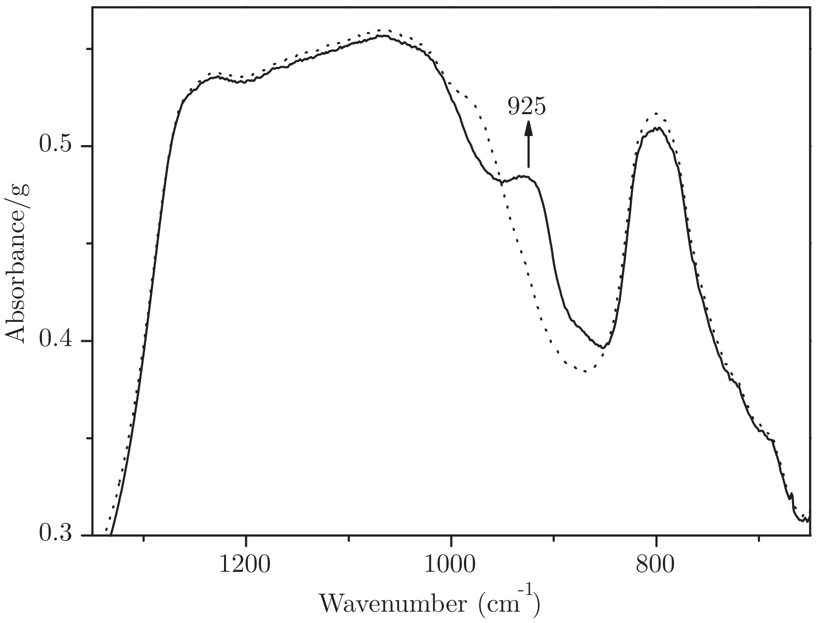

Figure 7.4: Lattice vibration bands before (dotted line) and after $^{16}O_2$ (solid line) adsorption on Cu/HZSM5 at room temperature and 200 mbar oxygen equilibrium pressure.

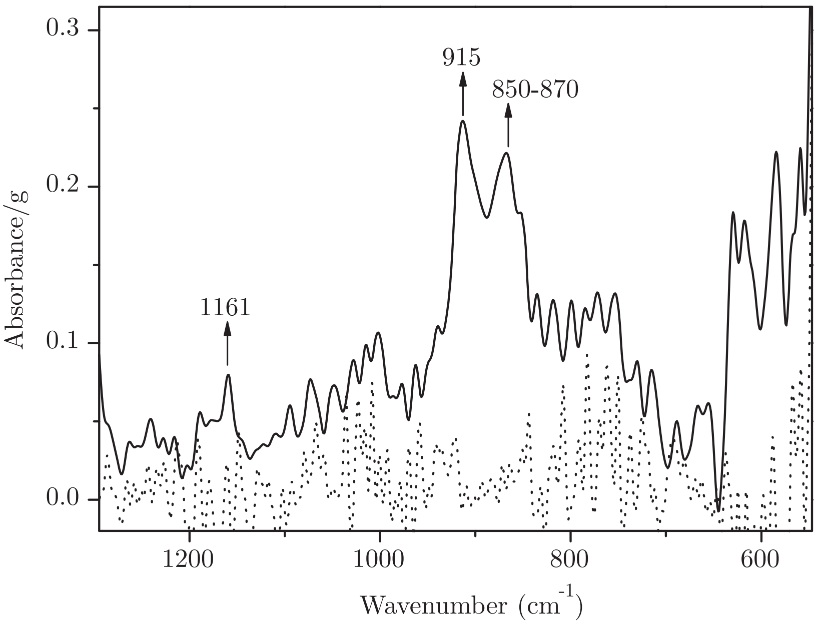

Figure 7.5: $^{16}O_2$ (solid line) and $^{18}O_2$ (dotted line) absorption bands on Cu/HZSM5 in the zeolite framework vibration region at room temperature and 200 mbar oxygen equilibrium pressure.

according to

$$2Cu(II)O_2^- \longrightarrow Cu(II) - O_2^{2-} - Cu(II) + O_2 \tag{7.1}$$

(as expected under conditions of high copper loadings and low Si/Al ratios).

The Cu-Cu distance was calculated to 3.42 Å and the Cu-O distance to 1.86 Å[38,40] which agrees with the values determined by EXAFS (see chapter 3.3). The superoxide complex Cu(II)-O_2^--Cu(II) was computed to be energetically less favorable and present only at the channel intersections. The corresponding IR frequency of 1049 cm^{-1} was not observed. The rise of the bands at 1161, 915 and 850 cm^{-1} on oxygen addition can be explained both by the formation of new copper oxide complexes but also by the perturbation of already formed species.

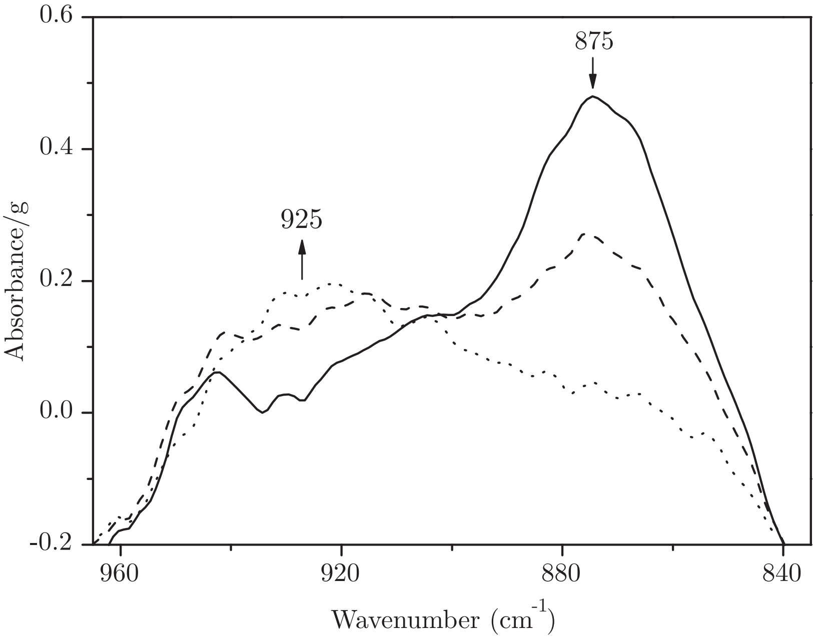

Figure 7.6: Absorption bands on Cu/HZSM5 in the zeolite framework vibration region at room temperature after the adsorption of 400 mbar oxygen equilibrium pressure (solid line) and subsequent evacuation for 15 minutes (dashed line) and 250 minutes (dotted line).

When the sample was degassed after oxygen adsorption, the signal around 920 cm^{-1} caused by the shift of the lattice vibrations due to the oxidation of copper to Cu(II) grew slightly, while the copper peroxide band around 875 cm^{-1} diminished. This could indicate that some of the dicopper oxygen complexes split into Cu(II)-O_2^- units (reverse of reaction 7.1). The intensity loss of the peroxide band surpasses the gain that the 920 cm^{-1} band exhibits, meaning that not all complexes split into single copper units. This supports the assumption that this band appears partly from a perturbation of the peroxide species caused by the adsorbed oxygen. When the oxygen is removed some of the peroxides return to their initial state causing the band to disappear.

The shifts of the band at 925 cm^{-1} in figure 7.4 and 7.6 to 915 cm^{-1} in figure 7.5 comes from the subtraction of the background. The peak in figure 7.4 appears as a shoulder on a downward curve, whose subtraction then leads to the narrower and shifted peak in figure 7.5, while the spectra in figure 7.6 were taken on a different sample, which inherently had a slightly different background and different oxygen equilibrium pressure.

All bands appearing in the region of the zeolite framework vibration range vanish when the $^{18}O_2$ isotope was used for the adsorption, a fact that suggests isotopic scrambling with the framework. Alternatively, the vibration of the copper oxide complexes may be coupled to the zeolite framework vibrations leading to a large number of possible stretching frequencies in mainly the same spectral region.[75] In the experimental FTIR spectra an average of all these frequencies or just the most intensive ones are observed, the others being overlapped by the lattice vibrations. In order to exclude the possibility that the oxygen adsorption might irreversibly change the catalyst, multiple adsorption-desorption cycles were performed with both oxygen isotopes.

7.1.3 Coadsorption of CO, CO_2, N_2 and H_2

7.1.3.1 Adsorption of Impurities

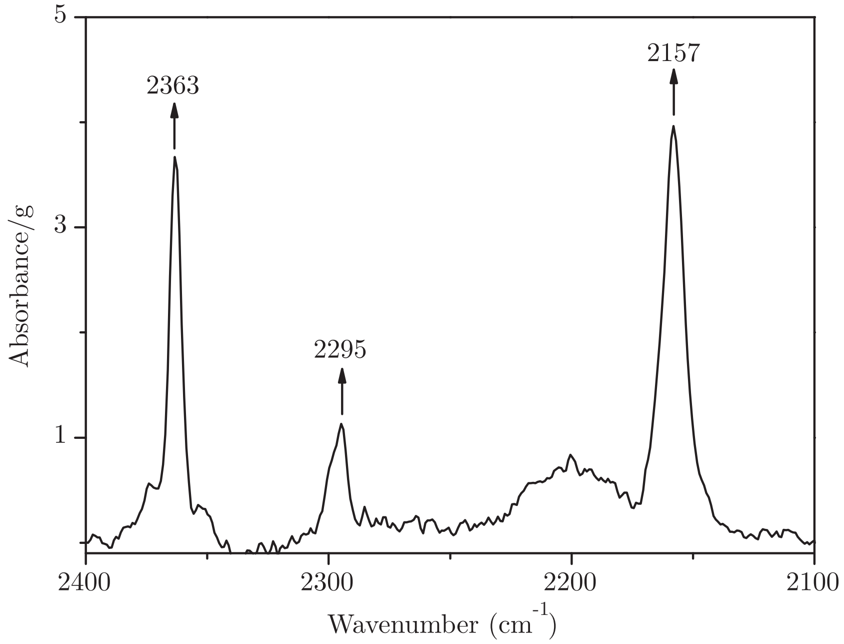

Figure 7.7: Absorption bands of carbon mono- and dioxide and nitrogen impurities on Cu/HZSM5 at room temperature.

When oxygen is adsorbed on Cu/HZSM5 samples three weak signals appear above 2000 cm^{-1} pictured in figure 7.7. The 2295 cm^{-1} peak was assigned by Sarkany et. al.[80] to a dicopper peroxide complex. We tested this assumption by studying the adsorption of different gases which could exist as impurities in the oxygen gas on copper-free and copper-containing HZSM5 samples. Pure nitrogen gas does not adsorb on copper-free samples, but when copper is present it binds to it giving rise to the 2295 cm^{-1} signal. The signal at 2363 cm^{-1} proved to belong to adsorbed carbon dioxide, while the signal at 2157 cm^{-1} arises from the adsorption of carbon monoxide. In ZSM5 zeolites the stretching frequency of CO adsorbed on Cu(I) is not site specific. The shape of the band is independent of the copper loading, predominant oxidation state or surface coverage.[81,82]

7.1.3.2 Adsorption of Hydrogen

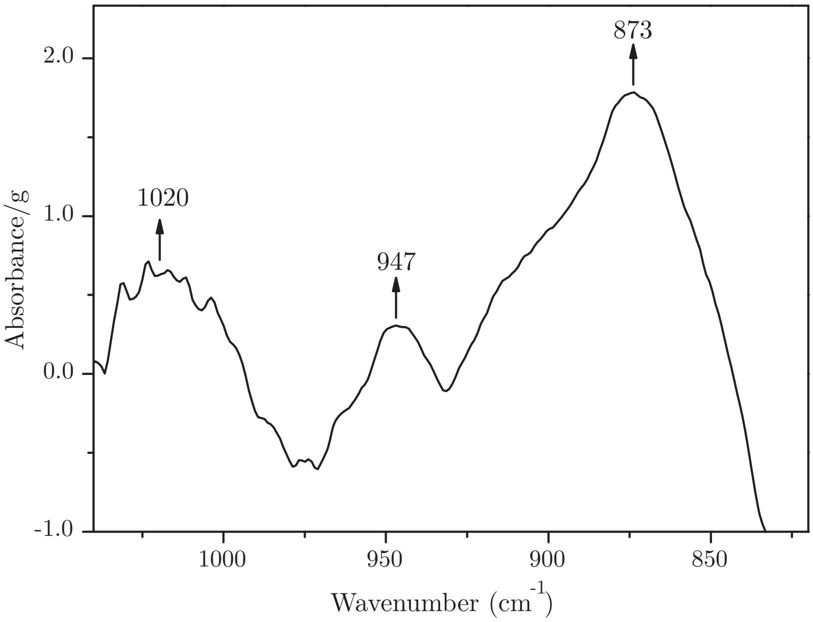

Figure 7.8: Absorption bands on Cu/HZSM5 in the zeolite framework vibration region at room temperature after the adsorption of 60 mbar hydrogen equilibrium pressure.

The adsorption of hydrogen was studied in order to test the behavior of the zeolite framework stretching vibrations. When oxygen was adsorbed the shift of the internal asymmetric stretching vibration to 915-925 cm^{-1} could be observed. This corresponded to the expected shift when copper is oxidized to Cu(II). On adsorption of hydrogen, copper is expected to be reduced to Cu(I). This fact is reflected by the shift of the framework vibrations towards higher wavenumbers. In figure 7.8 the rise of a band at 947 cm^{-1} is observable, which can be assigned to the expected reduction of copper to Cu(I). Intriguing is the rise of a broad feature around 1020 cm^{-1} which seems to indicate the reduction to Cu(0). Such a copper species would be hard to stabilize in the framework and might rather originate in copper ions which have not entered the zeolite but have remained on the surface. The signal around 873 cm^{-1} indicates that hydrogen too perturbs the dicopper peroxide complexes. Through the interaction with the hydroxyl groups water is formed, observable through a band at 1630 cm^{-1}. The signals of the perturbed OH groups become negative and broaden while broad signals around 2460 and 3000 cm^{-1} appear, assigned to the vibrations of hydroxonium ions and perturbed OH groups[68].

7.2 EPR Spectra

7.2.1 Single Dose Adsorption

When oxygen is adsorbed on the copper-containing HZSM5 samples the spectrum is broadened and the hyperfine splitting is lost due to spin exchange between the oxygen molecules and the Cu(II) ions (see figure 7.9).

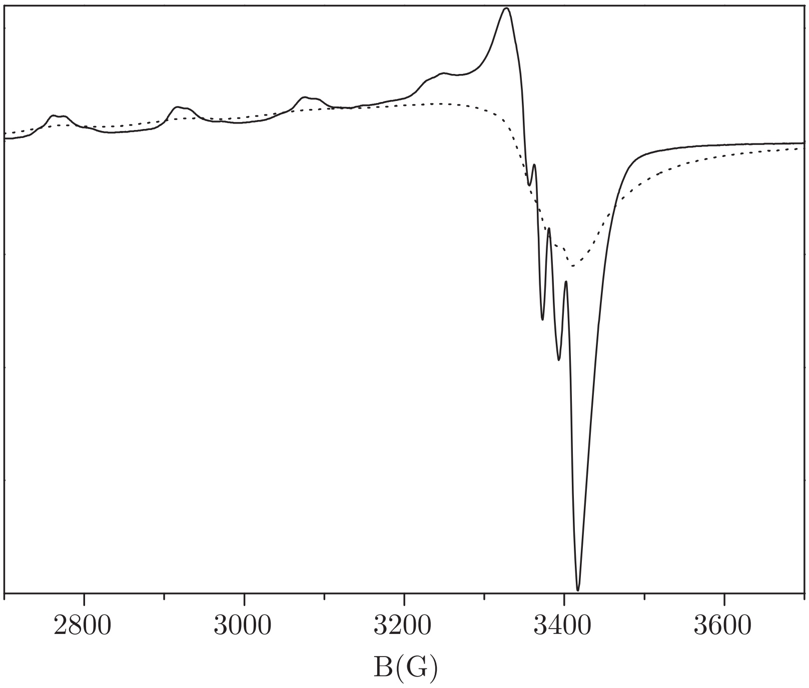

Figure 7.9: Cu/HZSM5 zeolite before (solid line) and after the adsorption of 100 mbar equilibrium pressure O_2 (dotted line) at room temperature. Spectra representative for both liquid and solid state ion exchanged samples.

The subsequent evacuation of the sample and oxygen desorption restores the initial EPR spectrum. The copper-oxygen spin exchange line broadening becomes observable only when the amount of oxygen added to the sample equals that of Cu(II) ions, for $4.6{\cdot}10^{-6}$ mol/g of copper $3{\cdot}10^{-6}$ mol/g oxygen are needed for detectable spin exchange. The order of magnitude corresponds to the oxygen amount needed in order to have all the Cu(II) ions interacting with at least one oxygen molecule. The spin exchange between Cu(II) and oxygen makes it impossible to determine which copper sites are involved in the oxygen adsorption. On the other hand it proves that all the Cu(II) sites are accessible for the interaction with oxygen.

In liquid ion exchanged samples the spin exchange occurs only above 25-30 K accompanied by the appearance of EPR lines of gaseous oxygen. In solid state ion exchanged samples the EPR lines are broadened by the spin exchange with oxygen over a temperature range from 4 to 300 K while no oxygen EPR lines are visible. Considering that the same oxygen amount was adsorbed on both samples, their different behavior must originate in the different copper concentrations and predominant oxidation states. The liquid ion exchanged samples have a ten times lower copper loading than the solid state ion exchanged samples, and about 80% of it is Cu(II). Thus the amount of oxygen given to the liquid state ion exchanged samples exceeds the copper amount, and free oxygen gas can be found in the sample tube.

The spin-rotation coupling of the triplet oxygen molecule gives rise to a large number of EPR lines which are spread over a large frequency range and only partly detectable by X-band EPR (see figure 7.10).[57,83]

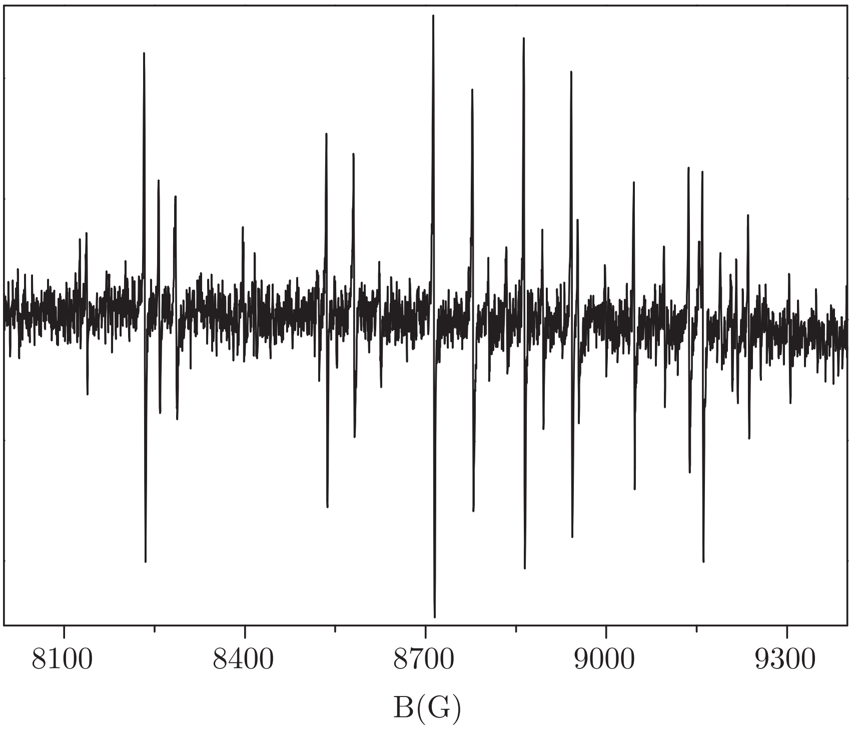

Figure 7.10: EPR lines of 10^{-8} mol·g^{-1} of molecular oxygen in Cu/HZSM5.

Detection is possible only in a certain pressure range, since with growing pressure the lifetime of the rotational states is shortened and the lines are getting broader. Dioxygen was added stepwise to the sample, using a standard volume and a pressure gauge until the gas phase oxygen EPR lines appear. The amount of oxygen which has been given to the sample up to that point is about $3{\cdot}10^{-8}$

mol/g. The appearance of these lines indicates that oxygen is no longer fully adsorbed by the sample but is accumulating in the EPR tube.

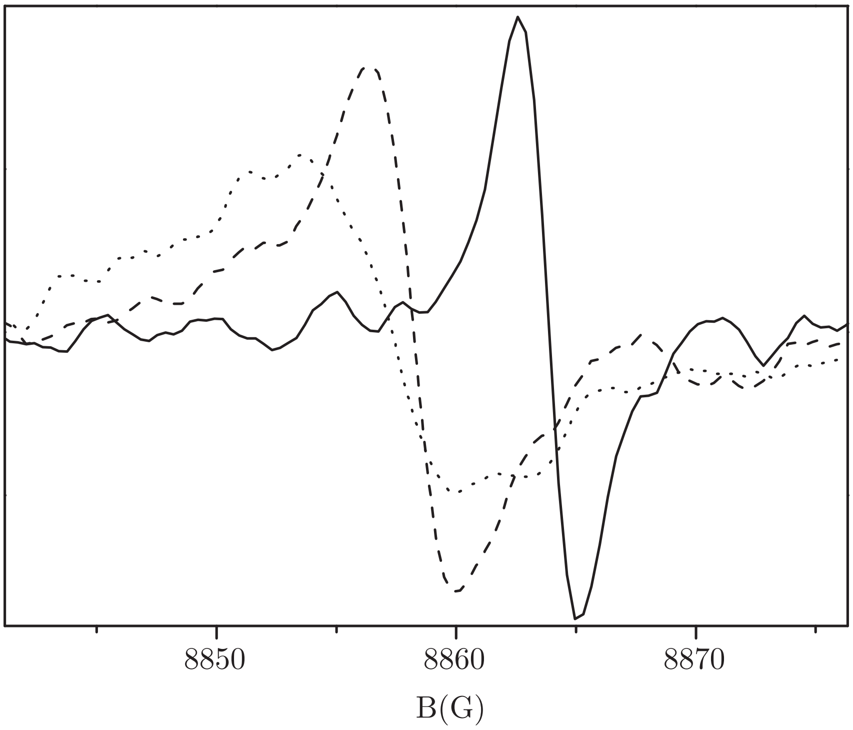

Figure 7.11: EPR lines of 8.28·10^{-8} mol·g^{-1} of molecular oxygen (solid line), 9.90·10^{-8} mol·g^{-1} (dashed line) and 14.85·10^{-8} mol·g^{-1} (dotted line) in Cu/HZSM5.

The widths of the EPR lines are determined by spin-spin relaxation lifetime which corresponds to the collisional lifetime. This means that with rising pressure, the mean free path length of the molecules diminishes and the width of the EPR lines grows as can be seen in figure 7.11. The linewidth of a single EPR line given has to be transformed from magnetic field units into frequency units:

$$\Delta\nu = \frac{\Delta B \cdot \nu}{B} \tag{7.2}$$

where ν is the fixed observing frequency and H the resonance field. The so gained linewidth is inversely proportional to the spin-spin relaxation life time. Considering the Maxwell velocity distribution of a gas molecule of molar mass M at a given temperature T and R=8.314472 J/(K·mol) the gas universal constant, the most probable velocity is given by:

$$v = \sqrt{\frac{2RT}{M}} \tag{7.3}$$

By multiplying the velocity with the lifetime the mean free path length is obtained. From the linewidth of the sharp EPR line obtained after the adsorption of 8.28·10^{-8} mol·g^{-1} of oxygen a mean free pathlength around 100 μm can be determined. This proves that these molecules are moving outside the zeolite lattice. At this point a rise in the spin concentration of the sample in the range of 4.5·10^{-6} mol/g can be determined. It is very intriguing that more copper seems to be oxidized to Cu(II) than the amount of oxygen adsorbed by the sample. Our FTIR results indicated that some antiferromagnetically coupled copper oxygen complexes can be split by the oxygen adsorption into separate Cu(II)O_2^- units, but this would not be enough to explain the large change in the spin density of the sample, thus a not further specified catalytic effect may have to be implied.

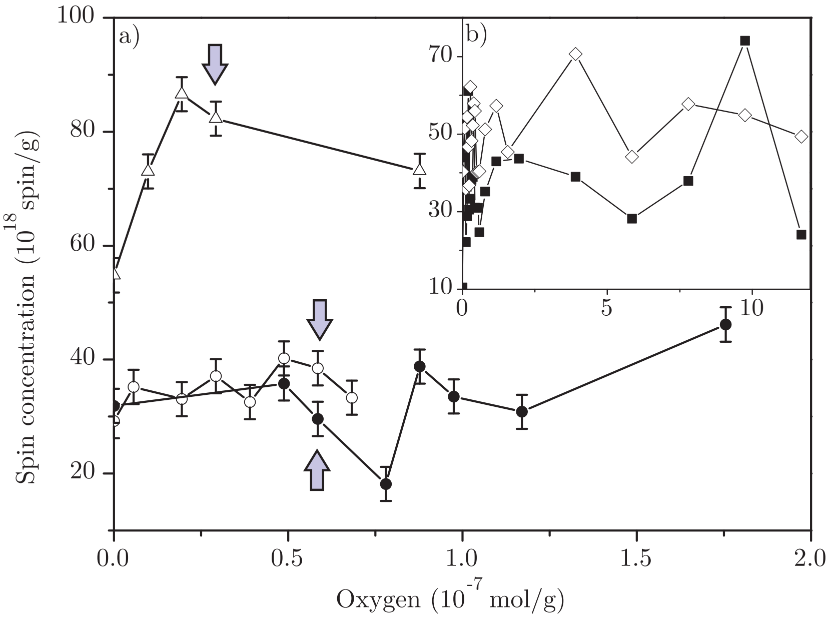

Figure 7.12: Spin concentration change of a solid state ion exchanged Cu/HZSM5 sample during the stepwise adsorption of aliquots of 9.75·10^{-9} mol/g of oxygen (open triangle). Oxygen was adsorbed in equal amounts on a second sample (open circles) which was then degassed and exposed again to the same procedure (full circles) (integration range 2450-3950 G). The arrows indicate the point at which the samples stop adsorbing and the oxygen gas phase signal appears.

By plotting the spin concentration of the sample over the amount of added oxygen the change of the oxidation state of copper can be correlated to the the oxygen adsorption (see figure 7.12). The arrows indicate the point at which the sample stops adsorbing the oxygen and the gas phase signal appears. Until that point the spin concentration of the sample rises constantly. After the appearance of oxygen in the gas phase the spin concentration of the samples seems to change chaotically. The reproducibility of this behavior was tested by degassing one sample and performing the adsorption on it again (open and full circles in figure 7.12). These fluctuations are much larger than the determined error caused by the movement of the sample (marked by the error bars in figure 7.12), so that they could not be explained only by the experimental setup.

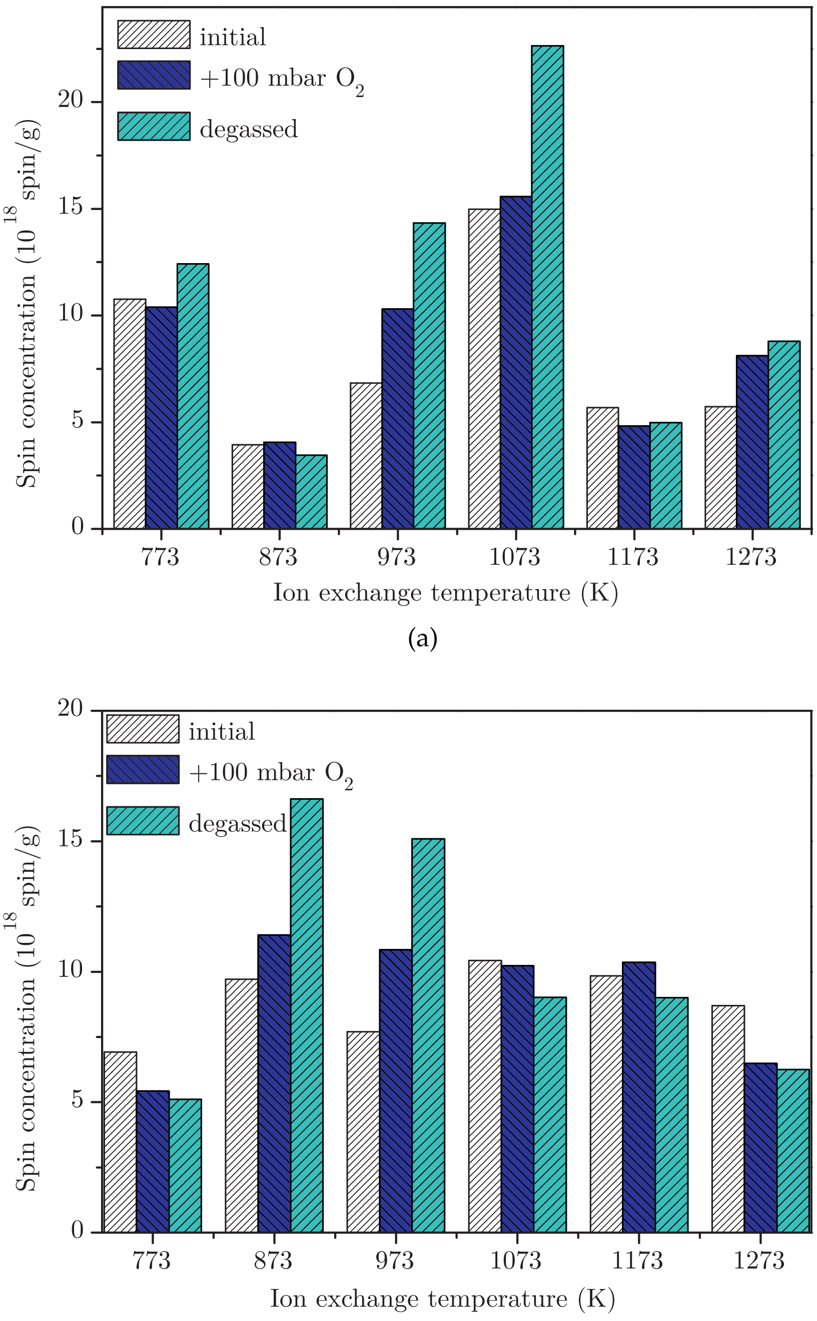

(a)

(b)

Figure 7.13: Spin concentration of two different charges of solid state ion exchanged Cu/HZSM5 samples (a) and (b) in their initial state (white bars), after the adsorption of 100 mbar equilibrium pressure of oxygen (blue bars) and subsequent degassing for 180 minutes at room temperature (cyan bars).

As was described previously the temperature at which the solid state ion exchange was performed influences the amount and oxidation state of the exchanged copper ions. Thus we analyzed the oxygen adsorption on samples exchanged at temperatures ranging between 773 and 1273 K. In figure 7.13 the spin concentration of two different charges of solid state ion exchanged samples is plotted as a function of their exchange temperature. Both batches (a) and (b) present the same ion exchange temperature dependence, with a spin exchange maximum for temperatures in the range of 973-1173 K. Oxygen adsorption caused the oxidation of most samples in both charges. In the first charge (figure 7.13(a)) the subsequent degassing of the samples caused an even stronger rise in the spin concentration of the samples than the oxygen adsorption did. This behavior was observed in the second charge only on two samples (figure 7.13(b)). It becomes clear that even though a trend for the change in the copper oxidation state can be guessed these measurements are unreliable. The cause is the fact that the larger the adsorption steps, the stronger the already discussed fluctuations of the spin concentration become (see figure 7.12(b)). These fluctuations make it impossible to determine a clear oxidation trend or a saturation behavior by this kind of adsorption measurements.

7.2.2 Continuous Flow Measurements

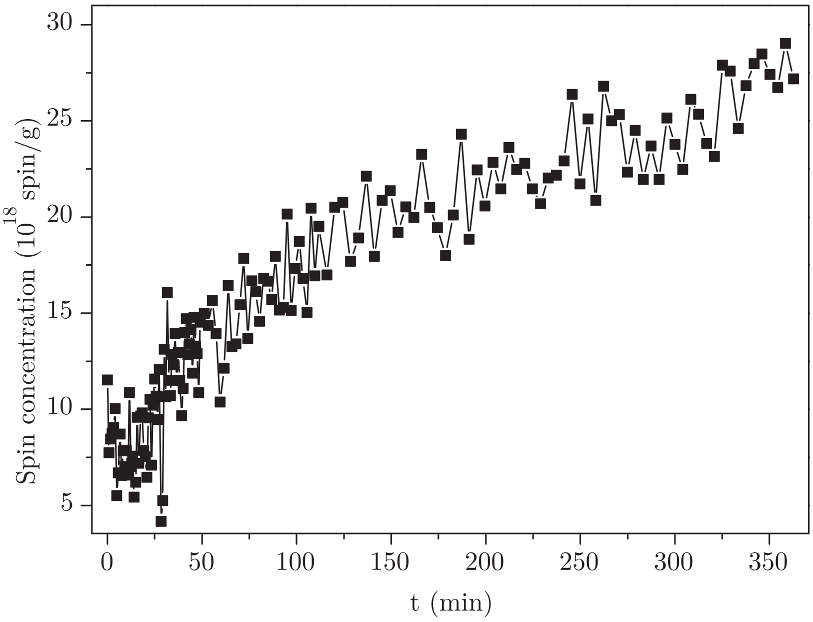

Figure 7.14: Spin concentration change of a solid state ion exchanged Cu/HZSM5 (ZSM973) under 2 ml·min^{-1} continuous flow of oxygen at room temperature, with 200 ml·min^{-1} continuous flow of helium as carrier gas (integration range 2450-3950 G).

Because of the strong fluctuations in the samples spin concentration observed during the stepwise adsorption of oxygen continuous flow adsorption measurements were performed. These measurements also showed fluctuations, but much weaker, proving that their origin lies not in a setup problem but rather in the dynamic character of the adsorption. The *in-situ* adsorption allowed an accurate observation of the oxidation process (see figure 7.14). All samples independent of their ion exchange procedure or temperature showed clear oxidation curves but no clear saturation points could be determined. This could be caused by the simultaneous and continuous further drying of the sample through the helium carrier gas, which thus increases the amount of reactive copper. Eventually saturation would be reached but the time needed exceeded the available experimental time.

7.2.3 Magnetization Plots

In figures 7.15(a) and 7.15(b) the reciprocal of the double integral of the spectra was plotted against temperature for the same ZSM973 sample before and after oxygen adsorption and subsequent desorption. The difference in the magnetization curve of the sample with adsorbed oxygen between the two plots is caused by the time gap of one day between the measurements. Both, liquid and solid state ion exchanged samples contain antiferromagnetically coupled dicopper complexes, one with the so called Néel temperature of 25 K (complex C1) and the second with the Néel temperature of 8 K (complex C2). The samples were then treated with 100 mbar O_2 equilibrium pressure at room temperature and the magnetization was measured again over the same temperature range under the same conditions as before. As seen in figure 7.15(a) the C1 species has been disturbed by the oxygen adsorption and its signal almost vanishes making the plot to resemble a single antiferromagnetic curve. Subsequent evacuation of the sample and oxygen desorption does not restore the initial magnetization behavior of the sample (see figure 7.15(b)), indicating that the C1 copper oxygen complexes were destroyed during the adsorption of oxygen while the C2 copper complexes remained unchanged. The copper complex C1, which was destroyed by the oxygen adsorption, has the higher Néel-Temperature and thus the stronger antiferromagnetic coupling. Considering also the FTIR results, we can assume that the peroxide type copper-oxygen (C1) complex is the active species, while the other copper oxide (C2) remains unchanged by the oxygen adsorption. The spin concentration of the samples rises during the oxygen adsorption due to the formation of individual Cu(II)-O_2^- units. The subsequent desorption causes also a slight rise in the spin density, a fact that could be explained by the dissociation of the antiferromagnetically coupled ($\mu - \eta^2 : \eta^2$-peroxo)-dicopper complexes into individual Cu(II)-O_2^- units. The EPR behavior of the liquid ion exchanged samples equals that of the solid state ion exchanged samples. The former ones were omitted from the graphs for the sake of clarity.

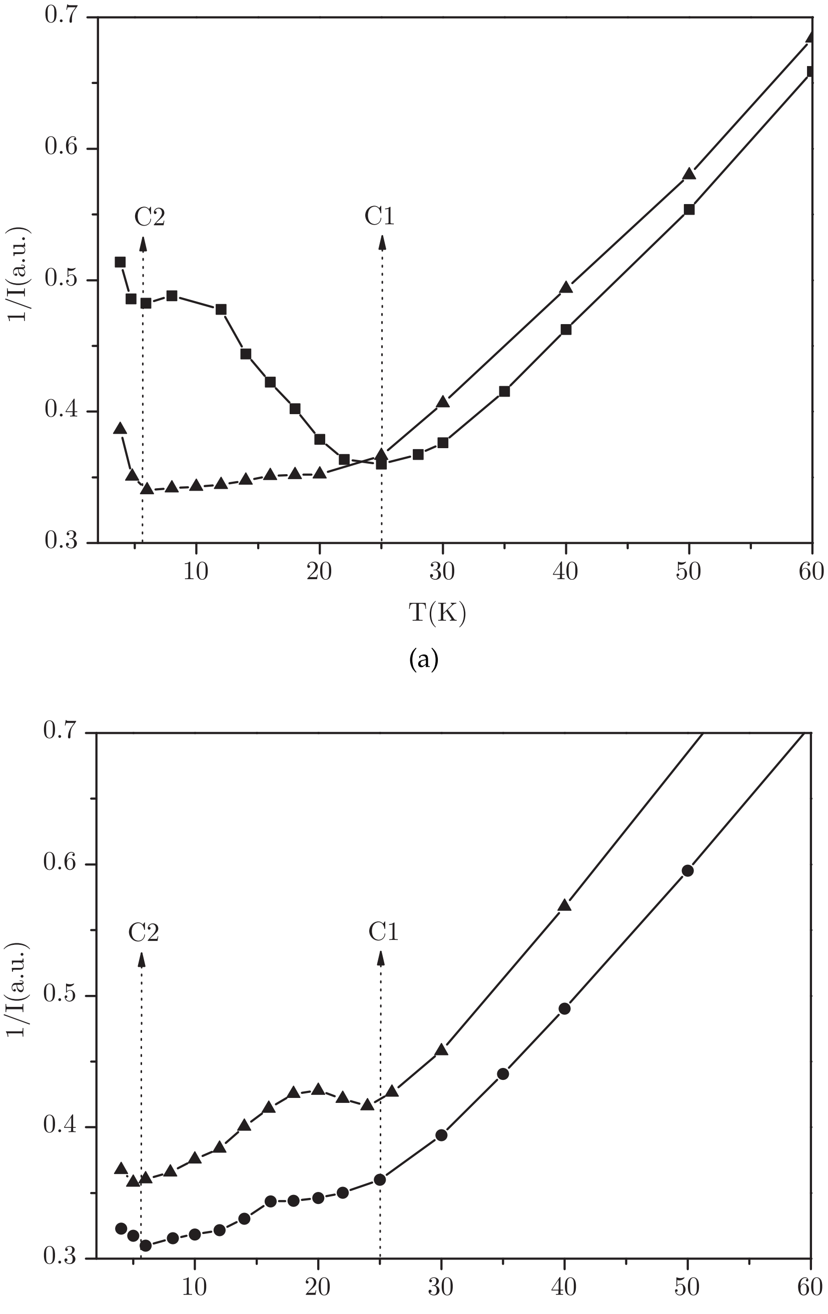

(a)

(b)

Figure 7.15: (a) Magnetization plot before (squares) and after 100 mbar oxygen adsorption (triangles) on solid state ion exchanged ZSM973. (b) Magnetization plot after oxygen adsorption (circles) and subsequent desorption (triangles) on solid state ion exchanged ZSM973.

7.3 DISCUSSION

Oxygen adsorbs on the samples both on the copper centers and the zeolitic hydroxyl groups at room and low temperatures. Oxygen adsorbs on all hydroxyl groups, forming a 1:1 H-bonded complex, with the internal Si(OH)Al groups showing the strongest interaction. The adsorption of oxygen on copper leads to the formation of Cu(II)-O_2^- units, both from the oxidation of individual Cu(I) ions on which oxygen binds side-on and the irreversible cleavage of one of the dimeric complexes. FTIR cannot distinguish between the dicopperoxide complexes, but on oxygen adsorption it clearly shows their interaction through the rise of the broad 850 cm^{-1} band. There is no indication here whether some dicopper complexes are formed or are just perturbed by the adsorption. The oxygen desorption causes the disappearance of this band accompanied by the rise of the Cu(II) content of the sample, leading us to the assumption that some complexes are split into individual Cu(II)-O_2^- units. The EPR measurements support this assumption, not only through the determined rise of the spin concentration of the samples both during oxygen adsorption and desorption, but also through the magnetization measurements. Thus we conclude that while oxygen interacts with all the dicopperoxide complexes only one is cleaved into the individual Cu(II)-O_2^- according to the reverse of reaction 7.1.

The presence of the dicopper complexes, their interaction with oxygen and the oxygen interaction with the hydroxyl groups make the Cu/HZSM5 zeolite very interesting for catalytic oxidation reactions. The activation of oxygen over ($\mu - \eta^2 : \eta^2$-peroxo) dicopper complexes in zeolites may be similar to the breaking of the O=O double bond by the analogous complex in Tyrosinase.[84] The Cu-Cu separation is crucial, in general the shorter the Cu-Cu distance the longer is the O-O bond.[85] When the O-O bond is broken this may permit oxygen to form a new bond, which in the presence of benzene as a substrate could lead to the formation of the C-O bond with benzene and thus to phenol or to complete combustion. Also in hemocyanin the peroxo-dicopper performs the reversible binding of oxygen.[86] The presence of the hydroxyl groups could support a radical mechanism for the phenol formation. The fact that they also interact with oxygen even at room temperature leads to a catalytic bifunctionality.

CHAPTER 8

BENZENE ADSORPTION

8.1 FTIR SPECTRA

8.1.1 Band assignment

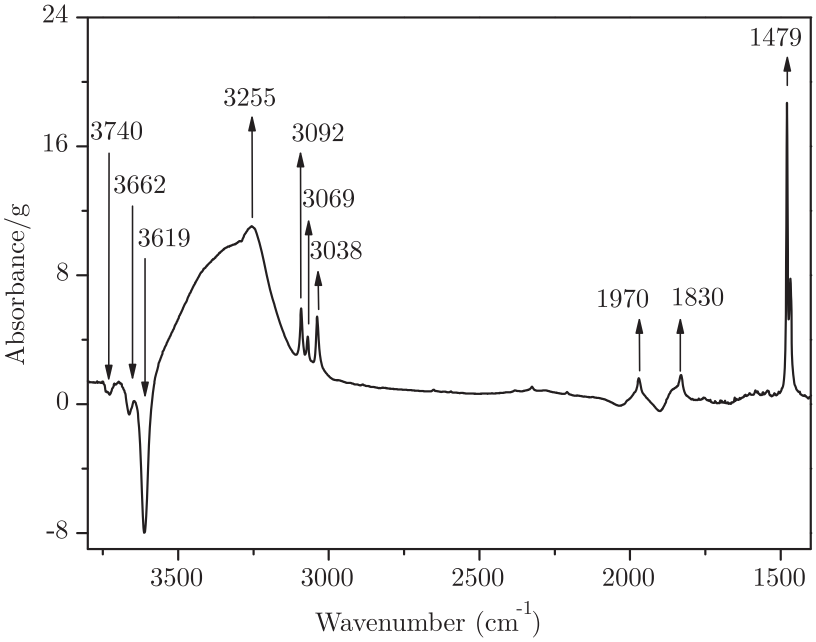

Figure 8.1: Benzene IR absorption bands after adsorption of 0.025 mbar equilibrium pressure of benzene on Cu/HZSM5 at room temperature.

The adsorption of benzene on HZSM5 zeolites has been studied by both experimental[9–18] and theoretical methods.[19] It is widely accepted that the benzene molecules interact with the hydroxyl groups of the zeolite, the terminal Si(OH) groups (3745 cm^{-1}), internal Si(OH)Al groups (3610 cm^{-1}) and extra lattice Al(OH) groups (3664 cm^{-1}). On benzene adsorption the intensity of these bands decreases, and they are slightly red-shifted to 3740 and 3662 cm^{-1}. On Cu/HZSM5 the signal of the terminal Si(OH) groups almost disappears, while the signal of the internal Si(OH)Al groups is broadened by 31 cm^{-1} from a linewidth of 27

cm^{-1} to 58 cm^{-1} and blue-shifted from 3610 cm^{-1} to 3619 cm^{-1} ($\Delta\tilde{\nu}$ = +9 cm^{-1}). It overlaps with the signal of the extra lattice Al(OH) groups. The interaction of benzene with the hydroxyl groups leads to the appearance of a broad absorption signal between 3250 and 3450 cm^{-1} on both copper-free and copper-containing HZSM5 simultaneously with the negative OH-bands. The inhomogeneity of the hydroxyl groups is accentuated by the benzene adsorption. This leads to the appearance of several overlapping bands near 3255, 3359, 3420 and 3172 cm^{-1} which form this broad signal.[16,87] By observing the perturbation of the hydroxyl groups at growing benzene loadings we can establish the order in which they interact with the guest molecule, first the terminal Si(OH) followed by the internal Si(OH)Al groups.

Table 8.1: Assignment of observed spectrum of benzene adsorbed on Cu/HZSM5 and wavenumber shift relative to the gas phase.[88]

in-plane vibrations			out-of-plane vibrations		
Assignment[a]	Observed $\tilde{\nu}$ (in cm^{-1})	Shift $\Delta\tilde{\nu}$ (in cm^{-1})	Assignment[a]	Observed $\tilde{\nu}$ (in cm^{-1})	Shift $\Delta\tilde{\nu}$ (in cm^{-1})
ν_{14}	1037	-1	ν_4	672	-4
ν_{13}	1468	-16		686	+10
	1479	-5	ν_{19}	845	-2
ν_{16}	1582	-4		860	+13
$\nu_{10}+\nu_{18}$	1755	0	$\nu_7+\nu_{20}$	1397	+4
$\nu_{14}+\nu_{17}$	2209	-1.5	$\nu_4+\nu_{11}$	1518	-10
$\nu_{17}+\nu_{10}$	2324	0		1545	+17
$\nu_3+\nu_{14}$	2381	-1	$\nu_{11}+\nu_{19}$	1810	-4
$\nu_6+\nu_{16}$	2596	+1		1817	+2
$\nu_6+(\nu_2+\nu_{18})$	2615	0		1830	+15
$\nu_3+\nu_{17}$	2652	-1		1850	+45
$\nu_3+\nu_{13}$	2822	0	$\nu_7+\nu_{19}$	1955	-5
$\nu_9+\nu_{16}$	2886	0		1963	+3
$\nu_9+(\nu_2+\nu_8)$	2904	-5		1970	+10
ν_{12}	3036	0	$\nu_{16}+\nu_{20}$	1985	-3
ν_{15}	3055	-2	$\nu_6+\nu_7$	2002	-2.5
$\nu_2+\nu_{13}+\nu_{18}$	3069	-2			
$\nu_{13}+\nu_{16}$	3091	0			

[a] Herzberg notation

As can be seen in figure 8.1 a large number of benzene IR lines are observed. The frequency of the observed bands, their assignment and shift compared to the frequency of the gas phase IR bands[88] are listed in table 8.1. Only some of the bands show a strong perturbation due to adsorption on the zeolite. The in-plane vibration bands and their combination bands are slightly red shifted by -1 to -5 cm^{-1} or not shifted at all on both copper-free and copper-containing HZSM5. The only exceptions seem to be the fundamental C-H stretching vibration (ν_{12}) and combination C-C stretching vibrations ($\nu_2+\nu_{13}+\nu_{18}$, $\nu_{13}+\nu_{16}$) with band maxima at 3036, 3069 and 3091 cm^{-1}. While the intensity of these bands increases progressively with the amount of adsorbed benzene, the band maxima are slightly blue shifted (≈1 to 2 cm^{-1}). No change was observed in the frequency of these bands on exchanging the protons in HZSM5 with Na$^+$ or Cu^{2+}. The fact that the in-plane vibrations are not or only very little perturbed during the adsorption process indicates that the molecule can vibrate in this plane as freely as in the gas phase.

In contrast, the out of plane fundamental or combination vibrations either split up or are blue shifted (figure 8.2 (a) and (b)) indicating that they are strongly altered either by a chemical bond or spatial constraint. The ν_4 fundamental out of plane vibration splits into two bands at 672 and 686 cm^{-1} when benzene adsorbs on HZSM5. When the proton is exchanged with a Na$^+$ ion the two bands are overlapped by a band at 695 cm^{-1} with a shoulder at 702 cm^{-1}. On Cu/HZSM5 the first band to appear in that region is the blue shifted ν_8 at 707 cm^{-1} ($\Delta\tilde{\nu}$ = +5 cm^{-1}) followed at higher benzene doses by the ν_4 lines. Since the ν_8 ring deformation vibration is IR inactive in the gas phase and its signal appears only on copper exchanged samples, it can be assigned to the benzene-copper interaction. In figure 8.2 (b) the rise of these three bands can be observed at different benzene doses of 4.4 molecules/u.c., 6.5 molecules/u.c. and 14.4 molecules/u.c..

8.1.2 Site population as a function of benzene loading

8.1.2.1 Filling of the Zeolite Pores - the ($\nu_7+\nu_{19}$) and ($\nu_{11}+\nu_{19}$) Bands -

The out-of-plane C-H vibrations near 1960 cm^{-1} ($\nu_7+\nu_{19}$) and 1815 cm^{-1} ($\nu_{11}+\nu_{19}$) split into three sets of bands when gaseous benzene is adsorbed on both copper-free and copper-containing HZSM5. At first only the blue shifted ($\Delta\tilde{\nu}$ = +10 and +15 cm^{-1}) group A at 1970 and 1830 cm^{-1} is observable, followed for benzene loadings higher than 2.5 molecules per unit cell, by the red shifted ($\Delta\tilde{\nu}$ = -5 and -4 cm^{-1}) group B at 1955 and 1810 cm^{-1}. At a loading of about 5 molecules per unit cell the intensities of the two pairs of bands, group A and B, is equal. Higher loadings cause a further increase of group B and the appearance of the weaker but strongly blue shifted shoulders at 1985 and 1850 cm^{-1}, group C.

For liquid ion exchanged Cu/HZSM5 samples the order of appearance of the groups remains the same as for copper-free HZSM5, namely A, B and C as broad unresolved shoulder. CuNaZSM5 samples, whose spectra are not included in the figures for the sake of clarity, behave similarly to the Cu/HZSM5 samples both in the order and number of lines and the loadings at which they appear. The spectrum of the solid state ion exchanged ZSM973 is quite broad, with only

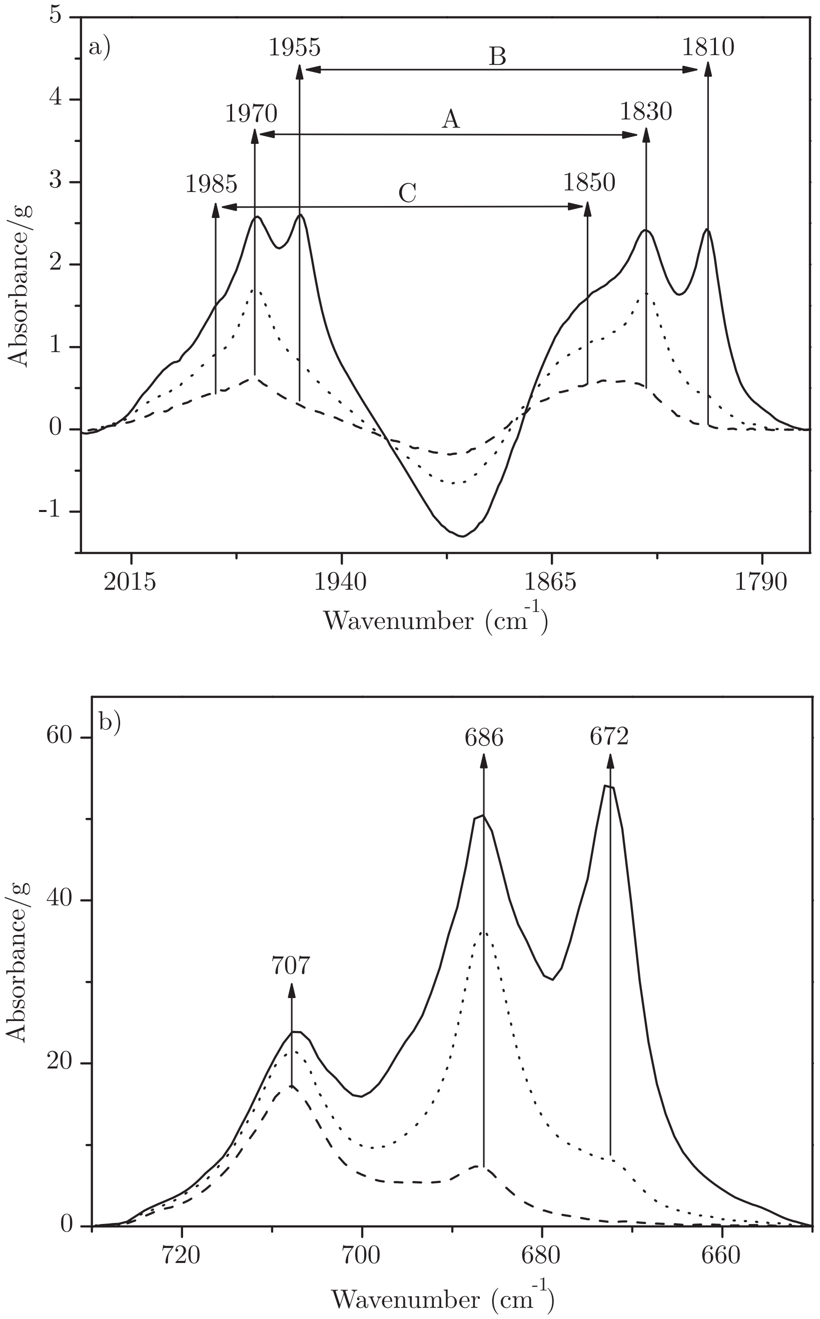

Figure 8.2: Out of plane vibrations of benzene on Cu/HZSM5 after the adsorption of 4.4 molecules/u.c. (dashed line), 6.5 molecules/u.c. (doted line) and 14.4 molecules/u.c. (solid line) (a) Splitting of the $(\nu_7 + \nu_{19})$ and $(\nu_{11} + \nu_{19})$ combination vibrations. (b) Splitting of the (ν_4) band and the blue shifted (ν_8) at 707 cm^{-1}.

group B clearly resolved. Solely on NaZSM5 the appearance order of the bands is reversed with group C appearing first, followed by the very weak group A and the stronger bands of group B. Table 8.2 gives the benzene loadings at which the bands appear in the different samples.

The behavior of these vibrations has been treated in literature as an indication

Table 8.2: Benzene loadings at which the split $(\nu_7 + \nu_{19})$ and $(\nu_{11} + \nu_{19})$ combination vibrations of benzene appear first, in molecules/u.c..

Sample	Group A (1970 and 1830 cm^{-1})	Group B (1955 and 1810 cm^{-1})	Group C (1985 and 1850 cm^{-1})
HZSM5	<0.5	2.5	>4*
Cu/HZSM5	0.1	3	>4*
ZSM973	0.2	2.1	>4*
CuNaZSM5	0.1	2.8	0.1
NaZSM5	2	4	0.1

*These bands appear as shoulders making it difficult to determine the exact moment of their appearance. The values given here are the ones at which the the lines are seen with confidence.

to the location of the adsorbed benzene in the copper-free HZSM5 pore structure. It has been proposed that in the low-loading range (1-4 molecules/u.c.) most of the benzene molecules could reside at the channel intersections. The framework is not greatly altered even when the intersections are essentially full.[14] With rising loadings (5-6 molecules/u.c.) the benzene molecules would move into the sinusoidal channel segments and then (> 6 molecules/u.c.) into the midsections of the straight channels.[13] This adsorption order is not stringent since even at loadings as low as 1.6 molecules/u.c. a small fraction of benzene may exist in the straight channels of HZSM5 though a larger fraction is localized at the channel intersections.[15] Some contradictory observations have also been reported, where the benzene molecules first occupy the straight channels and only at higher loadings (> 4 molecules/u.c.) enter the channel intersections.[11] The stacking structure of the benzene molecules inside the pores has also been discussed without a clear outcome. A clustered state of benzene with the molecules packed side by side with their planes parallel to the channel wall[15] forming 1D 'strings'[11] has been considered as well as almost vertically positioned molecules.[14]

The exchange of the cation is known to influence the channel size and pore volume and thus change the number of trapped benzene molecules at a particular location. We observed that in all samples except NaZSM5 the $(\nu_7 + \nu_{19})$ and $(\nu_{11} + \nu_{19})$ out of plane combination vibrations of benzene split into three sets of bands, with the high frequency pair A (1970 and 1830 cm^{-1}) appearing first followed by the lower frequency pair B (1955 and 1810 cm^{-1}) for loadings in the range of 2.1 to 3 molecules/u.c.. The appearance of this new set of bands can be interpreted as benzene molecules finding new adsorption sites, while the red shift indicates that these sites have a slightly larger free space to accommodate the molecules. At the same time the second signal from the split ν_4 out of plane vibration visible till then only at 686 cm^{-1}, appears at 672 cm^{-1}, experiencing also a low frequency shift. A further increase of the benzene loading leads to the appearance of the blue-shifted shoulders indicating the squeezing of the molecules. The larger the blue shift the stronger is the squeezing of the molecule. This means that the shift of group C is generated by a stronger spatial constraint than the one responsible for the shift of group A. Simultaneously the C-H stretching vibrations at 3036, 3069 and 3091 cm^{-1} become blue shifted.

Thus we conclude that for copper-free and copper-containing HZSM5 the benzene migration seems to take the following route. The benzene molecules enter the zeolite structure through the straight channels. When the benzene loading grows to 2 molecules/u.c. the second molecule enters the channel intersections. In the channel intersections up to 4 molecules/u.c. can be stabilized, a further increase of the loading pushing the molecules into the sinusoidal channels. This means that only one benzene molecule resides at each intersection as there are only 4 intersections/u.c.. Intriguing is the fact that on the NaZSM5 samples the behavior of the molecules seems to be exactly opposite, the molecules seemingly going from the sinusoidal into the straight channels and only at higher loadings into the channel intersections. In figure 8.3 the intensities of the C-H out of plane vibrations of benzene on NaZSM5, Cu/HZSM5 and ZSM973 at a loading of 5.5 molecules/u.c. show a clear difference between the samples and thus the adsorption sites.

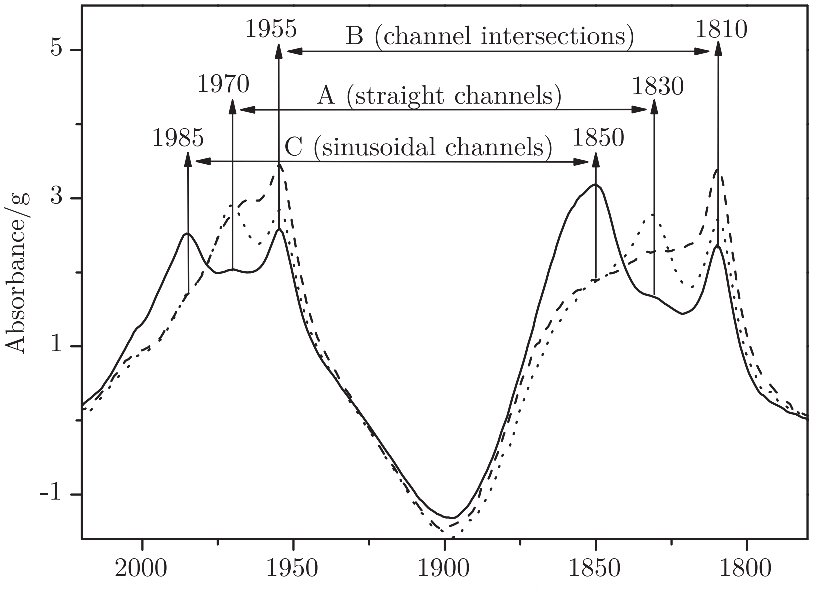

Figure 8.3: Splitting of the ($\nu_7 + \nu_{19}$) and ($\nu_{11} + \nu_{19}$) combination vibrations of benzene on Cu/HZSM5 (dotted line), CuZSM5700 (dashed line) and NaZSM5 (solid line) at a loading of 5.5 molecules/u.c. at room temperature.

8.1.2.2 Copper vs. the Hydroxyl Groups - the ν_{13} Band -

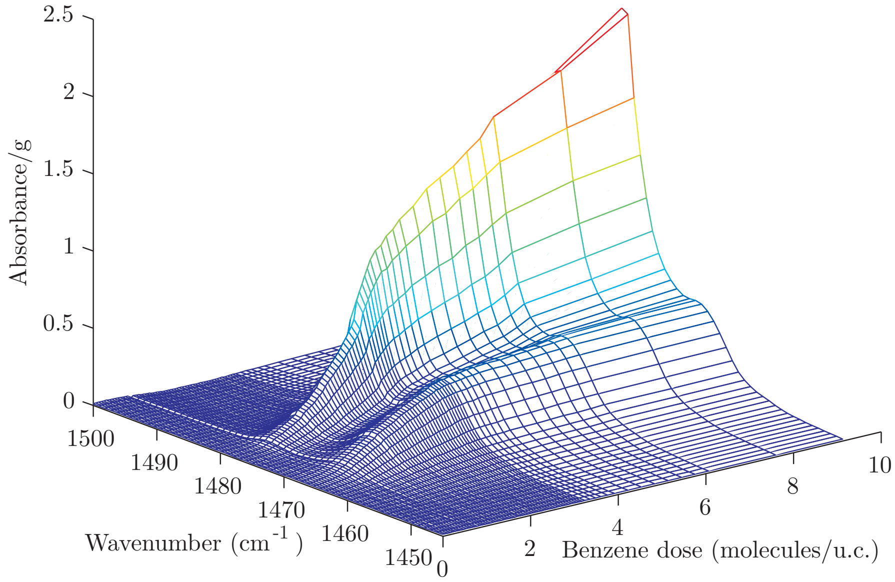

Figure 8.4: Splitting of the ν_{13} C-C stretching vibration of benzene into the adsorption on the OH groups (1479 cm^{-1}) and on copper (1468 cm^{-1}) on Cu/HZSM5 at room temperature

In order to better understand the adsorption process not only on the hydroxyl groups of the zeolite but also on the exchanged copper ions we observed the ν_{13} C-C stretching vibration of benzene on copper-free and copper-containing zeolites. On copper-free HZSM5 as well as on NaZSM5 the ν_{13} vibration appears at 1479 cm^{-1}, red shifted compared to the gas phase vibration by $\Delta\tilde{\nu}$ = -5 cm^{-1}. When adsorbed on copper-containing HZSM5, independent of the ion exchange method, a second line appears at 1468 cm^{-1} ($\Delta\tilde{\nu}$ = -16 cm^{-1}) as can be seen in figure 8.4. The copper-benzene interaction leads to a larger shift to lower wavenumbers than the benzene-OH interaction, proving the stronger binding and a weakening of the C-C bond. Also after desorption or heating of the sample the line corresponding to the copper-benzene interaction prevails while the other one diminishes. In order to distinguish beyond doubt the benzene adsorbed on the hydroxyl groups (1479 cm^{-1}) from gaseous benzene (1484 cm^{-1}) we observed also the ν_{14} C-H bending vibrations (1037 cm^{-1}). This signal appears only at high pressures (above 20 mbar equilibrium pressure) with unresolved rovibrational P- Q- and R-branches. Up to that point no gas-phase benzene is observable and the 1479 cm^{-1} band can be accurately assigned to benzene adsorbed on the OH groups of the zeolite.

8.1.3 IR-derived site-specific adsorption isotherms

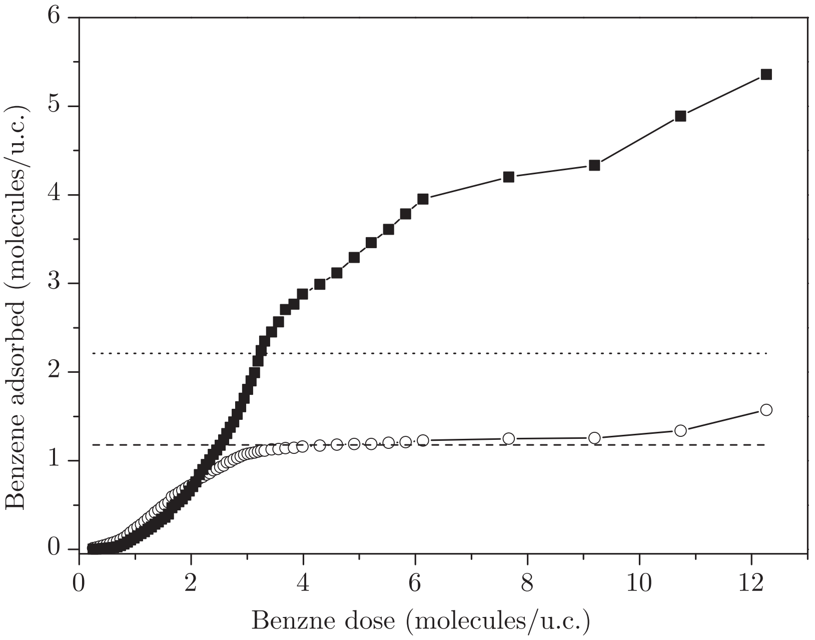

Figure 8.5: IR-derived adsorption isotherm of benzene adsorbed on copper (open circles) and OH groups (filled squares) on Cu/HZSM5. The amount of Cu/u.c. in the sample is indicated by the dashed line, the H^+/u.c. amount by the dotted line.

For a quantitative evaluation of the adsorption, the 1479 and 1468 cm^{-1} vibration bands were fitted by Lorentzian lines (eq. 3.25) in dependence of the equilibrated benzene dose given to the sample. For both lines equal extinction coefficients were assumed (62±1 l/cm·mol[9]), since they originate in an IR-allowed benzene ring mode which is only slightly perturbed at the two adsorption sites. The areas and half widths of the fitted curves were used to determine the absorbance amplitude from which the concentration of the absorbing substance can be computed by equation 3.23. The resulting IR adsorption isotherms describe not only the total adsorption on all sites like conventional adsorption isotherms, but they distinguish adsorption at the different sites. Thus the benzene adsorption on the hydroxyl groups can be observed independently and simultaneously with the adsorption on the copper centers (figures 8.5, 8.6 and 8.7). This separation of adsorption sites is not valid for NaZSM5 samples, since the interaction of the Na ions with benzene does not lead to an individual IR band so that only the overall adsorption on both OH groups and Na centers can be measured (figure 8.8).

Adsorption on molecular sieve zeolites usually shows a type I isotherm shape,

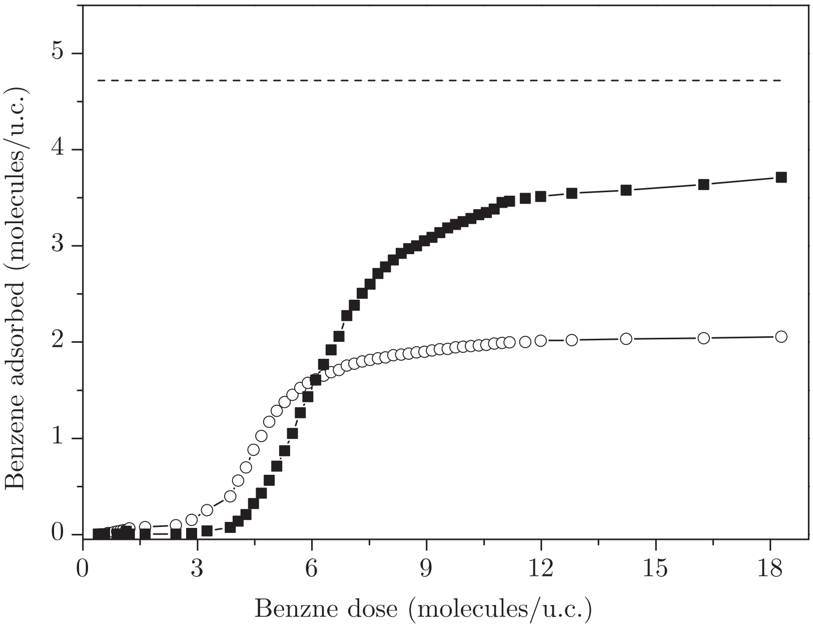

Figure 8.6: IR-derived adsorption isotherm of benzene adsorbed on copper (open circles) and OH groups (filled squares) on ZSM973. The amount of Cu/u.c. in the sample is indicated by the dashed line.

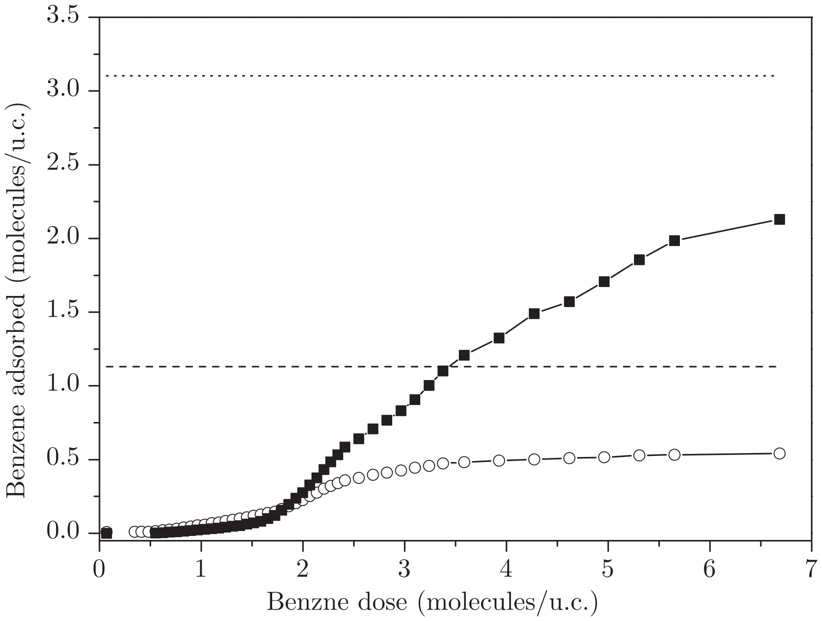

Figure 8.7: IR-derived adsorption isotherm of benzene adsorbed on copper (open circles) and OH groups (filled squares) on CuNaZSM5. The amount of Cu/u.c. in the sample is indicated by the dashed line, the H^+/u.c. amount by the dotted line.

where the amount adsorbed increases continuously with pressure, asymptotically approaching a limit that corresponds to the complete filling of the pores with molecules.[89] Our isotherms show a very slow rise of adsorbed molecules before the typical type I isotherm slope begins. This slow rise is caused by the

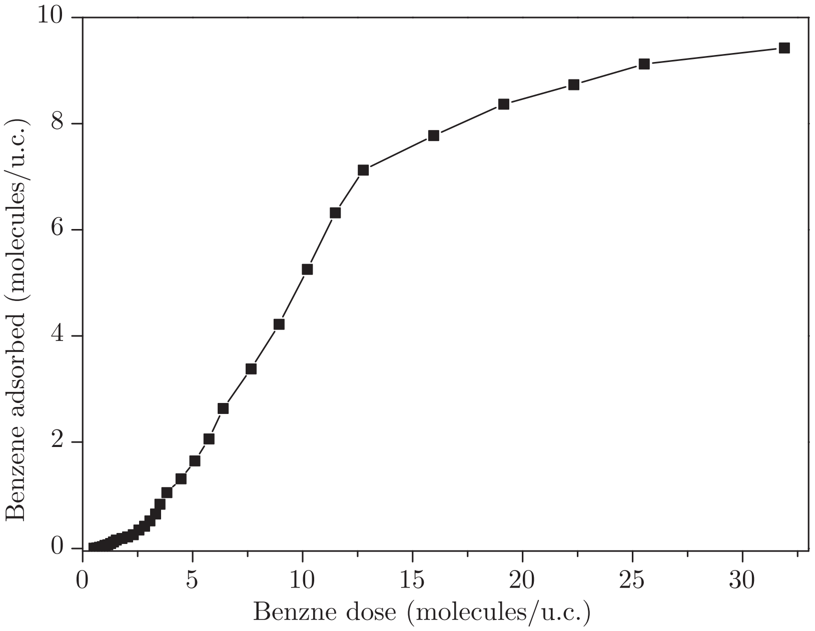

Figure 8.8: IR-derived adsorption isotherm of benzene adsorbed on OH groups (filled squares) on NaZSM5.

small benzene amounts that are given to the sample, which do not permit a homogeneous benzene distribution inside the sample from the beginning. The saturation limit for NaZSM5 and liquid and solid state ion exchanged Cu/HZSM5 lies in the range of 4 - 10 benzene molecules/u.c.. The amount of benzene given to the sample up to saturation depends on the pore volume (see table 5.1). The benzene density in the zeolite pores remains with 0.27 g/cm^{-3} for Cu/HZSM5 and 0.41 g/cm^{-3} for NaZSM5, well below the value of liquid benzene, which is 0.88 g/cm^{-3}. Thus condensation effects can be ruled out. The CuNaZSM5 sample shows a lower adsorption capacity than the rest of the samples, which is surprising considering that the pore volume is similar to that of the other samples while the mesopore area is larger. The presence of both copper and sodium ions seems to hinder or slow down the adsorption process.

8.1.3.1 Adsorption on the Hydroxyl Groups

While on all samples the adsorption on copper follows smoothly a Langmuir isotherm, the adsorption on the hydroxyl groups shows a more step-like character (figure 8.5 and 8.7). We can correlate the isotherms with the behavior of the out of plane vibrations of benzene. The steps in the isotherms occur at a bit higher loadings than the appearance of the 1970 and 1830 cm^{-1} bands and their splittings. This discrepancy is caused by two factors: one is a measure of uncertainty in deciding when the new lines appear first and second is the fact that the isotherms are computed over the integral intensities of the 1479 and 1468 cm^{-1} vibration bands. For example, on the Cu/HZSM5 the group A appears around 0.5 molecule/u.c. followed by group B for loadings higher than 2 molecules/u.c. on the hydroxyl groups, while group C grows continuously as broad shoulders. The isotherm shows steps at 1.8 - 2, 2.8 - 3 and 4 molecules/u.c. on the hydroxyl groups. If we consider it as a summation of the local isotherms of the straight and sinusoidal channels and the channel intersections then the steps indicate the filling of the pores in these particular locations. Thus they confirm the already described adsorption route of benzene on the hydroxyl groups.

8.1.3.2 Adsorption on Copper

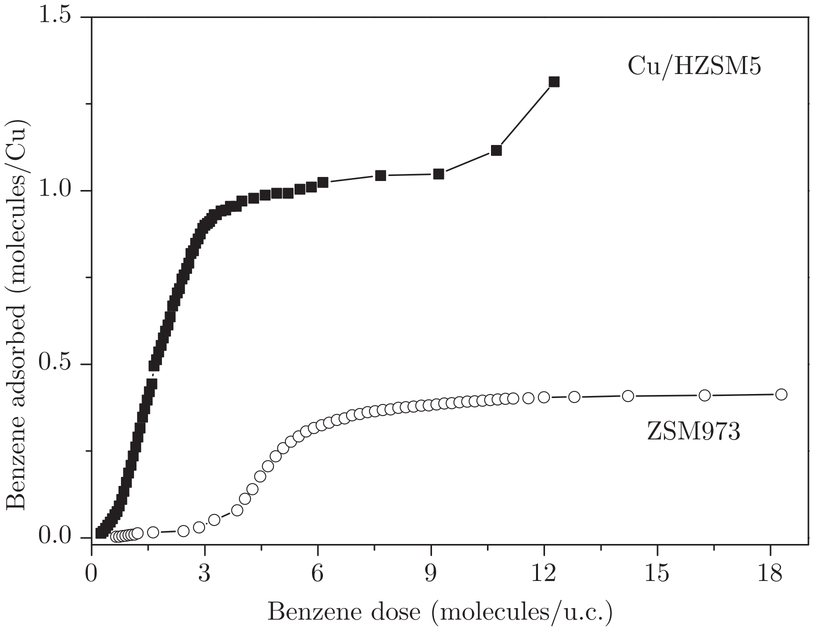

Figure 8.9: Benzene adsorption isotherms plotted as molecules adsorbed on the total amount of copper on Cu/HZSM5 (filled squares) and ZSM973 (open circles).

The adsorption isotherm for the copper centers exhibits a less pronounced step-like character. The benzene adsorption on the copper centers precedes the benzene-OH interaction and for loadings as high as 3 molecules/u.c. for solid state ion exchanged samples it surpasses it. For liquid ion exchanged samples, already at a benzene loading of 1.5 molecules/u.c. the number of benzene molecules adsorbed on copper centers equals the number of molecules adsorbed on the hydroxyl groups. Copper is the slightly preferred adsorption site for benzene, but the copper centers are quickly saturated. Comparing the adsorption isotherms of benzene on copper and hydroxyl groups with the assignment of the molecule's location, we can determine that the saturation limit is reached while the benzene molecules are accumulating in the channel intersections and that no or only very little copper-benzene interaction seems to occur in the sinusoidal channels. The overall adsorption order for Cu/HZSM5 zeolites is thus Cu > terminal Si(OH) > internal Si(OH)Al.

In figure 8.9 the benzene adsorption isotherms are plotted as benzene molecules per copper ion. Saturation is reached for loadings of 0.4 molecules/Cu on the solid state ion exchanged sample. On the liquid ion exchanged samples which contain lower amounts of copper the saturation limit is reached at a benzene to copper ratio of 1. The difference in the maximum benzene loading on copper of the two samples lies in the ion exchange procedure, which exchanges different amounts of copper ions with different oxidation states. In case of liquid ion exchanged samples, the predominant copper oxidation state is Cu(II) (0.9 Cu(II)/u.c. from 1.2 Cu/u.c.), while for solid state ion exchange, the copper ions exist mostly in the Cu(I) oxidation state (0.3 Cu(II)/u.c. out of 4.7 Cu/u.c.)(see section 3.2). The benzene adsorption on copper should reduce the oxidation state from Cu(II) to Cu(I), but not all copper seems to interact with benzene. This would mean that there is a maximal amount of copper that can interact with benzene. Any further increase in the copper concentration of the sample doesn't improve the benzene adsorption capacity of the zeolite. The extra copper ions might not interact with benzene at all, being secluded in the sinusoidal channels or having entered the zeolite framework.

8.1.4 Zeolite framework vibrations

The bands at 860 and 845 cm^{-1} in figure 8.10 correspond to the ν_{19} benzene vibration. The negative band around 920 cm^{-1} indicates the reduction of Cu(II) ions. Only a small peak can be observed around 960 cm^{-1}, which would be caused by Cu(I). At the same time two signals arise at 870 and 884 cm^{-1} which could be related to the perturbation of the dicopper peroxide complexes Cu(II)-O_2^{2-}-Cu(II).[38,73] As in the case of the oxygen adsorption the dicopper complexes interact with the adsorbent but from the FTIR spectra alone, the strength of the interaction cannot be determined. At this point a simple spatial perturbation of the complexes is as plausible as a direct binding interaction.

8.2 EPR SPECTRA

8.2.1 Single Dose Adsorption

Benzene adsorption causes a continuous amplitude decrease of the $g_{\|}$=2.31 and 2.32 signals. The $g_{\|}$=2.31 signal is affected first, suggesting that the α4 Cu(II) ions

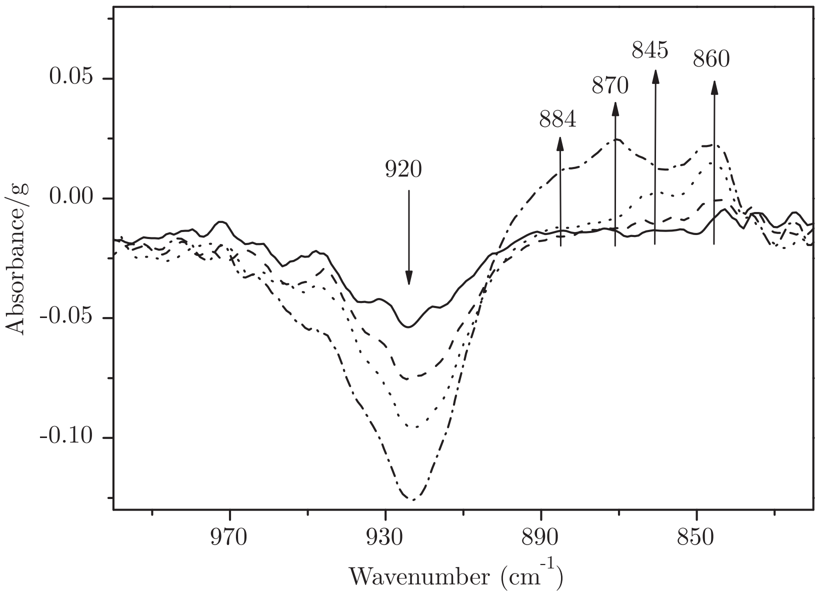

Figure 8.10: IR bands in the zeolite framework vibrations region after the adsorption of benzene on Cu/HZSM5 at 0.25 (solid line), 0.5 (dashed line), 1 (dotted line) and 10 mbar (dash-dotted line) benzene equilibrium pressure at room temperature.

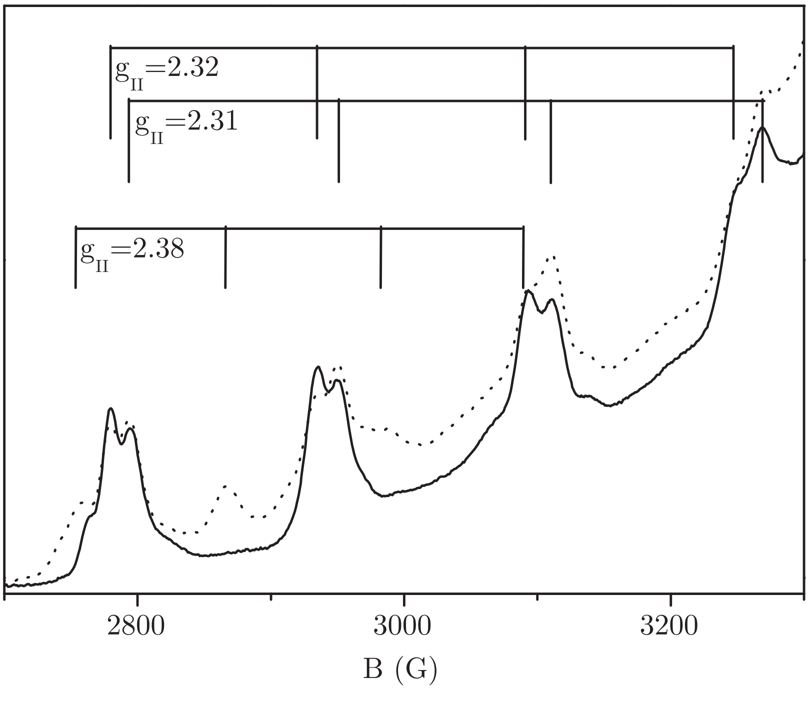

Figure 8.11: Parallel range of the Cu(II) EPR spectra with $g_{\|}$-factor assignment in Cu/HZSM5 zeolites at room temperature before (solid line) and after the adsorption of 6 molecules/u.c. (dotted line). The spectrum was taken with a ZSM973 sample, but it is representative for all the samples independent of the ion exchange procedure.

interact first with the benzene molecules, followed then by the $\alpha3$ Cu(II) ions, until the signals of both species disappear. At the same time a new signal with

$g_{\|}$=2.38 grows in, which corresponds in value to hydrated octahedral copper ions.

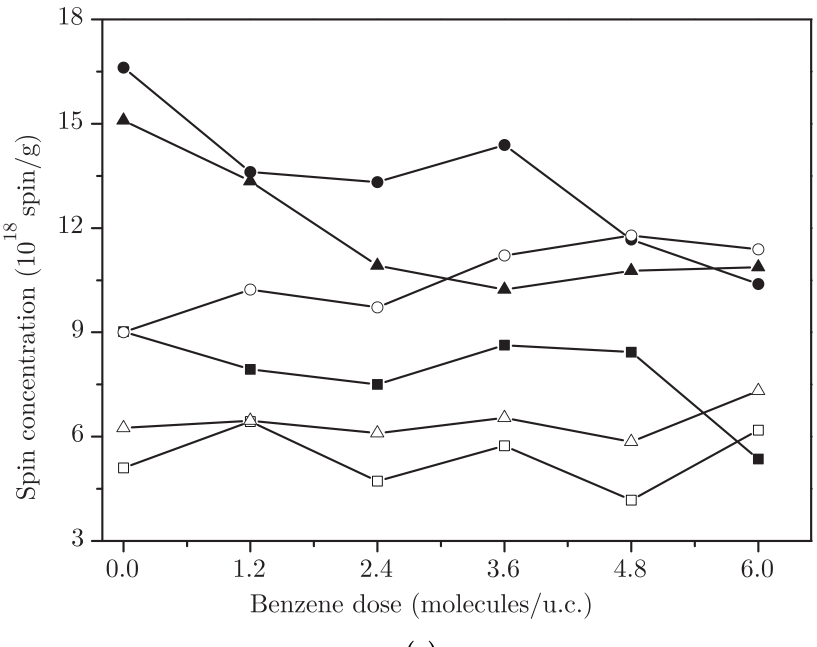

(a)

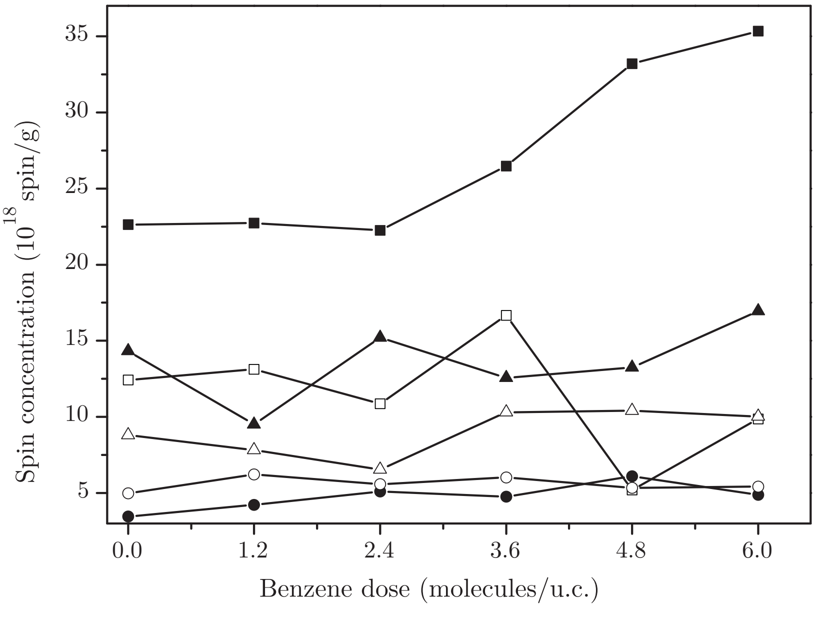

(b)

Figure 8.12: Spin concentration of two different charges (a) and (b) of solid state ion exchanged samples (ZSM773 (open square), ZSM873 (full circle), ZSM973 (full triangle), ZSM1073 (full square), ZSM1173 (open circle), ZSM1273 (open triangle)) as a function of the adsorbed benzene dose (1.2 molecules/u.c.) at room temperature. The error bars of $2{\cdot}10^{18}$ spins/g are not plotted for the sake of clarity.

The spin concentration of different samples was determined before and after the step-wise adsorption of 1.2 molecules/u.c. per aliquot of benzene (see figure

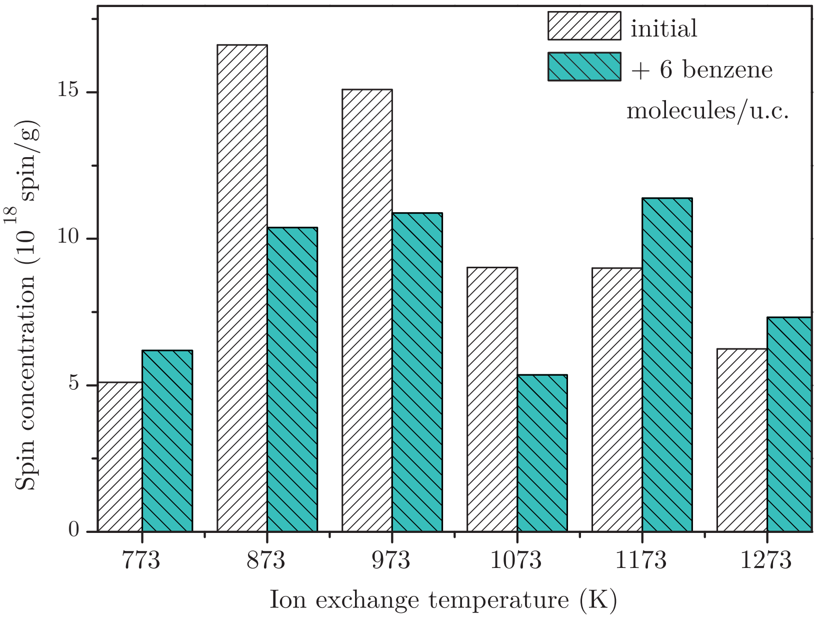

(a)

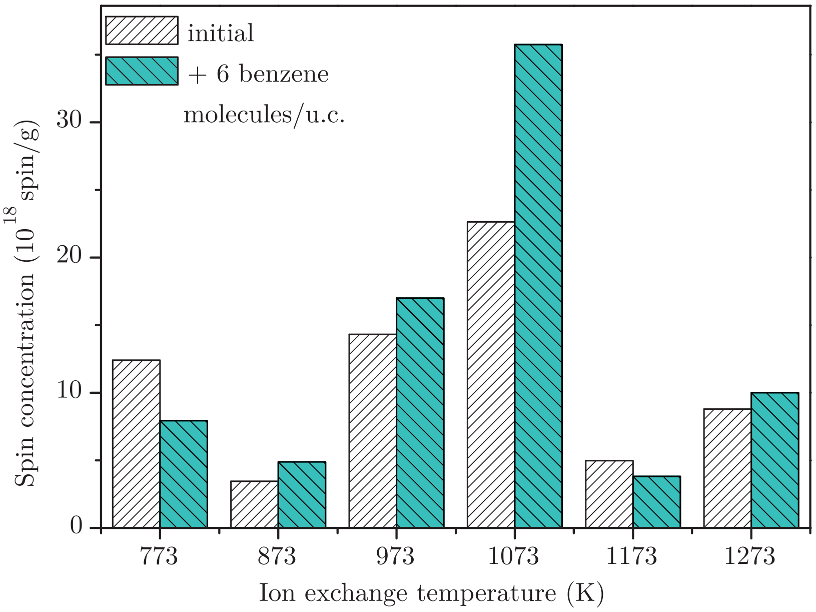

(b)

Figure 8.13: Spin concentration of two different charges (a) and (b) of solid state ion exchanged samples as a function of the ion exchange temperature before and after the adsorption of 6 molecules/u.c. of benzene at room temperature.

8.12). It became obvious that as in the case of the oxygen adsorption, this kind of adsorption process is unreliable. Only three samples in the first charge (figure 8.12 (a) ZSM873, ZSM973, ZSM1073) showed a reduction trend while the others seem to remain constant or even to be oxidized (ZSM1173 in figure 8.12 (a) or

ZSM1073 in figure 8.12 (b)). The fluctuations in the spin concentration are not as strong as in the case of oxygen, but rather lie inside the error margin of $2 \cdot 10^{18}$ spins/g. Still they might falsify the results.

This becomes even more obvious if one compares the initial spin concentration of the samples with the one after the adsorption of 6 molecules/u.c. of benzene (figure 8.13). Samples, exchanged at the same temperature but in different charges behave differently. Considering the fact that the changes of the spin concentration are hardly larger than the error margins, it could be assumed that these changes are due to the handling of the sample and are not caused by the adsorbed benzene and that the spin concentration in fact remains constant. Either the amounts of benzene given to the sample are too small to cause a change in the spin concentration that surpassed the error margins, or the amounts are too large and the sample is directly saturated. Thus it became crucial to find another more reliable adsorption method.

8.2.2 Continuous Flow Measurements

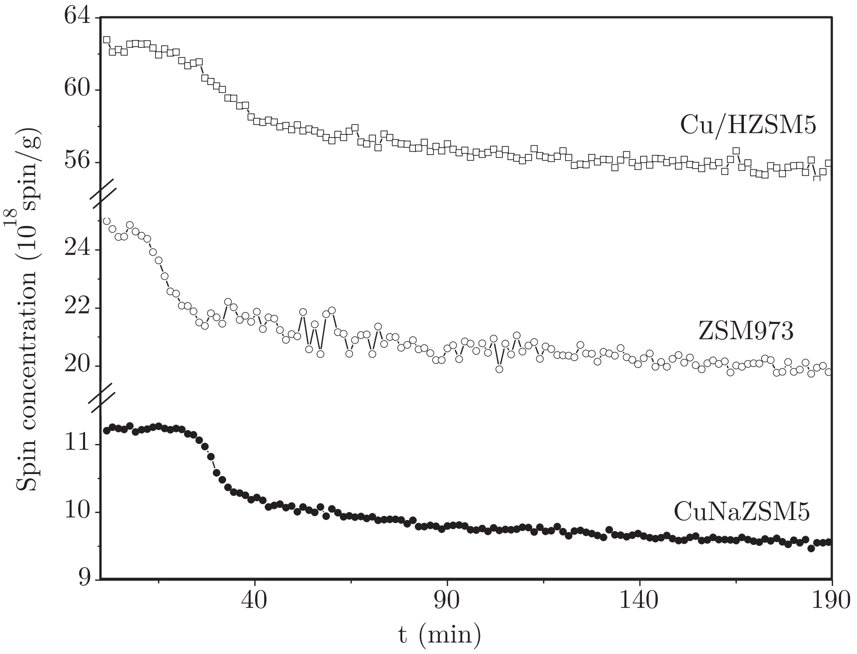

Figure 8.14: In situ spin concentration determination for a benzene continuous flow of $1.5 \cdot 10^{-5}$ mol/s at 343 K for Cu/HZSM5 (squares), ZSM973 (empty circles) and CuNaZSM5 (filled circles). Values contain both the Cu(II) and the radical spins. Note the change of scale for the three curves.

As in the case of oxygen, benzene continuous flow adsorption measurements were performed, only that in this case the gas and the sample had to be heated up at 343 K in order to prevent condensation. After the benzene flow is switched on, the spin concentration of the samples remains almost constant for a certain amount of time needed for the benzene molecules to reach and enter the sample (figure 8.14). When the adsorption process takes place the spin concentration decreases fast. After 40 minutes a certain level of saturation is reached as can be seen in figure 8.14.

For the solid state ion exchanged sample ZSM973 the amount of Cu(II) is only 6% of the total copper content of the sample. Thus the spin density of the sample is lower and the reduction of the few Cu(II) ions is achieved faster. For the liquid ion exchanged sample the Cu(II) concentration is higher but the total copper amount in the sample is lower than for ZSM973. Only $5{\cdot}10^{18}$ spins/g of the ZSM973 sample is reduced by benzene and $8{\cdot}10^{18}$ spins/g of the Cu/HZSM5 and $1.6\ {\cdot}10^{18}$ spins/g of CuNaZSM5 samples. This means that ca. 80 % of Cu(II) is not accessible to benzene due to the experimental conditions which make the core of the sample inaccesible for the benzene gas flow. Still a clear reduction process could be observed independent of the sample preparation method.

8.2.3 The Benzene Radical Cation

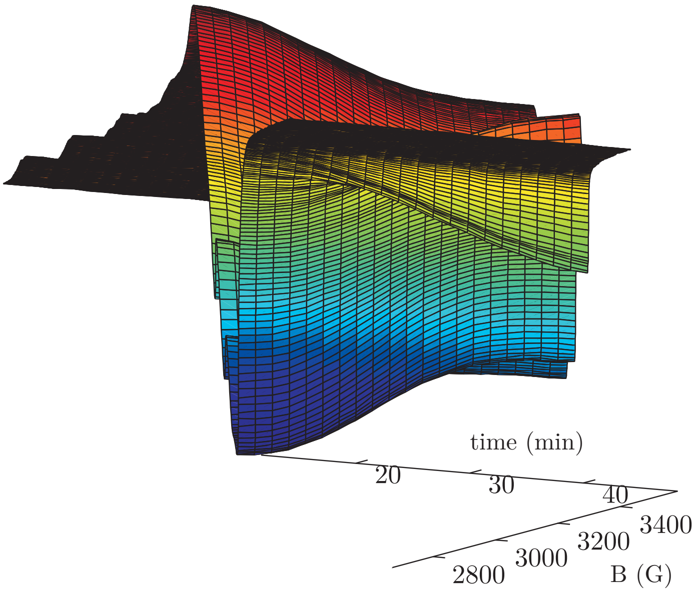

Figure 8.15: Cu/HZSM5 EPR spectra under a continuous benzene flow of $1.5{\cdot}10^{-5}$ mol/s at 343 K.

While the sample was exposed to a continuous flow of $1.5{\cdot}10^{-5}$ mol/s of benzene the intensity of the copper EPR signal diminishes while another signal grows in at higher magnetic fields (figure 8.15). The new signal has the typical hyperfine septet of a benzene radical cation. In figure 8.16 a, the measured spectrum for a Cu/HZSM5 sample exposed to the benzene flow for 28 minutes is compared with the simulated isotropic benzene radical cation spectrum. The anisotropy in the negative part of the spectrum is caused by the overlap of the radical signal with a zeolite framework electron defect signal. Still the simulation is in good agreement with the experiment. The values for the hyperfine coupling constant a=4.45 G and g=2.0027 correspond to the expected values.[56] On HZSM5 (figure 8.16 b) the benzene adsorption leads also to the formation of the benzene radical cation, with a=4.45 G and g=2.003. The intensity of the signal is lower and the linewidth is half as large as on Cu/HZSM5, showing a higher rotational mobility. The HZSM5 sample was saturated with benzene but the spin concentration of the sample lies only at 10^{14} spins/g. This means that for copper-free HZSM5 only about 10^{-6} radicals per unit cell are formed. On CuNaZSM5 the same benzene radical cation signal appears as in the Cu/HZSM5 samples. Only on copper-free NaZSM5 samples the benzene adsorption does not lead to the formation of a benzene radical cation.

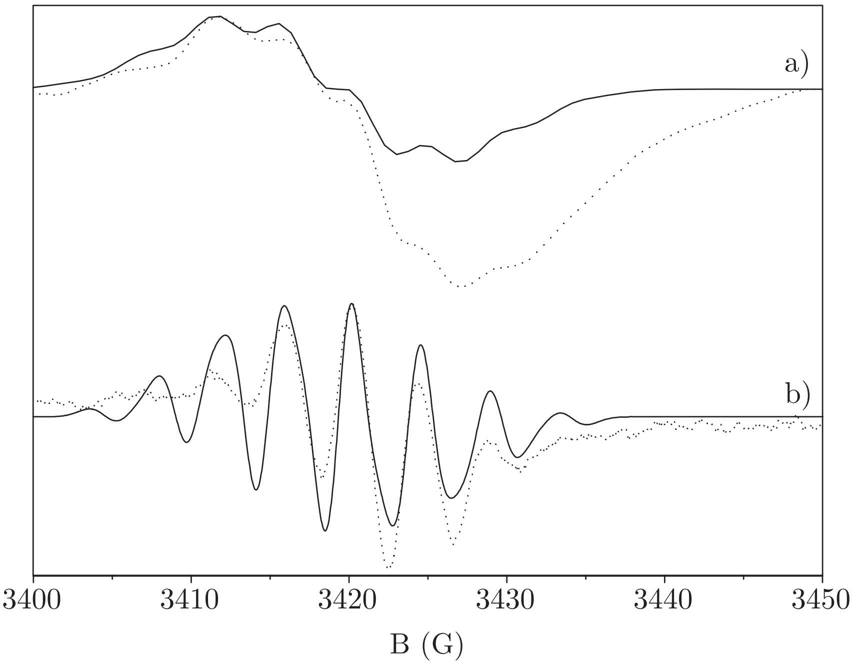

Figure 8.16: Benzene radical cation signal measured (dotted lines) and simulated (solid lines) on Cu/HZSM5 (a) and HZSM5 (b).

In figure 8.17 the radical signal on liquid ion exchanged samples (Cu/HZSM5, solid line) is compared to the one on solid state ion exchanged samples (ZSM973, dotted line) measured at 373 K. In both cases the radical signal overlaps with a zeolite framework electron defect signal. This makes it difficult to determine if the

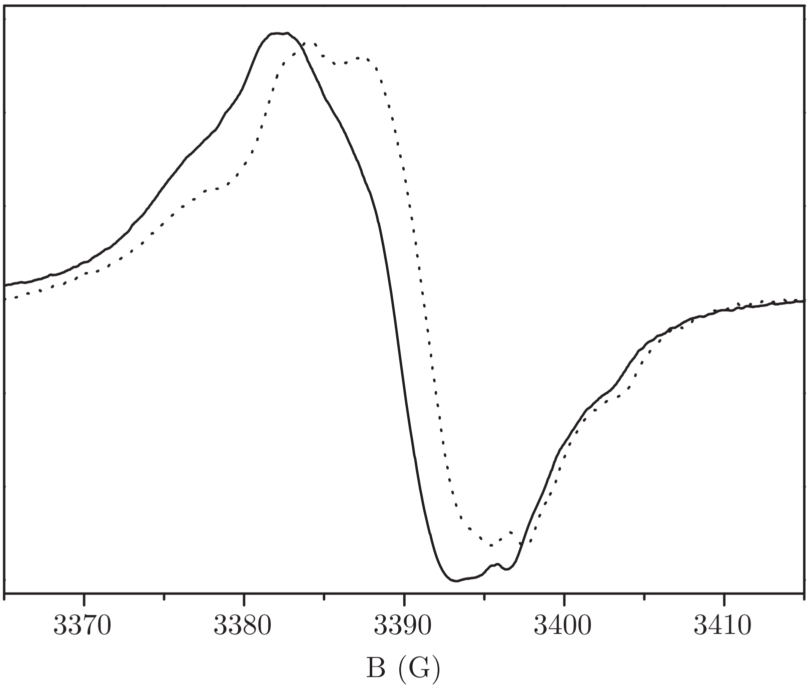

Figure 8.17: Normalized benzene radical cation measured on Cu/HZSM5 (solid line) and ZSM973 (dotted line) at 373 K after the adsorption of 100 mbar equilibrium pressure of benzene

differences between the two spectra are due to different environments or due to a different amount of electronic defects. In the presence of oxygen the linewidth of the septet broadens on both samples. The signals are normalized for a better visualization and comparison, but the radical signal on the liquid ion exchanged samples is actually much stronger than on solid state ion exchanged samples, a fact that might be correlated to the different amounts of Cu(II) ions available in these samples.

It is conceivable that the copper reduction goes along with benzene oxidation under the formation of benzene radical cations:

$$C_6H_6 + Cu(II) \rightarrow C_6H_6^{\bullet +} + Cu(I) \tag{8.1}$$

or

$$\begin{aligned} &C_6H_6 + [Cu(II)(\mu - \eta^2 : \eta^2 - O_2^{2-})Cu(II)]^{2+} \rightarrow \\ &\rightarrow C_6H_6^{\bullet +} + [Cu(II)(\mu - O_2^{\bullet -})]^{+} + Cu(II) \end{aligned} \tag{8.2}$$

Equation 8.1 involves the reduction of the Cu(II) ions which can be observed in situ while benzene is passed through the sample (figure 8.15). While the reduction saturates, so does the signal of the benzene radical cation confirming their interaction and supporting equation 8.1. On all samples only about $\approx 10^{17}$ spins/g (10^{-3} radicals/u.c.), ten times less than the number of Cu(II) ions ($\approx 10^{18}$ spins/g) are detected as radicals. The others may have terminated quickly.

8.2.4 Magnetization Plots

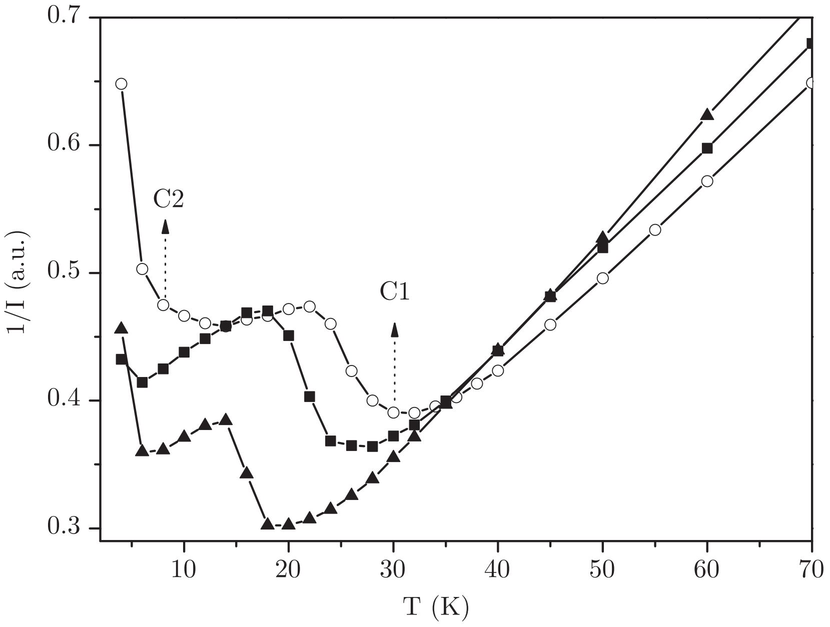

Figure 8.18: Magnetization plot before (circles) and after the adsorption of 0.1 molecules/u.c. (filled squares) and subsequent further adsorption of 0.4 molecules/u.c. (filled triangles) of benzene on Cu/HZSM5.

Temperature dependent EPR measurements were performed in order to determine the magnetic behavior of the samples and thus the behavior of the two dicopper complexes (C1 and C2) before and after benzene adsorption (figure 8.18). Benzene adsorption on the sample causes a shift of the so called Néel temperature of the C1 complex from 30 to 20 K, while the Néel temperature of the second complex C2 remains at 8 K. Compared to the adsorption of oxygen where the C1 signal disappeared, benzene adsorption does not destroy the dicopper complexes even though some interaction exists. The Néel temperature shift of C1 can either be explained by some weak interaction of the dicopper peroxide with the benzene molecules or by an increased spatial constraint of the complex due to the accumulation of benzene molecules in the zeolite pores. Neither possibility supports equation 8.2 which includes the dissociation of the dicopper complex. At the same time the other peroxide complex (C2) is not affected by the adsorption of neither benzene nor oxygen. Either this complex possesses a higher stability or a more secluded location inside the pore structure of the zeolite.

8.3 DISCUSSION

During the adsorption of benzene a fraction of Cu(II) is reduced to the EPR silent Cu(I) as can be seen both by the EPR in situ measurements and the FTIR framework vibrations. The fact that with EPR only the reduction of a small amount of Cu(II) is observed, might be caused by the experimental conditions. While for the FTIR experiments a very thin sample pellet was held at room temperature and an appropriate equilibration time was used for each measurement, the EPR measurements were performed under a continuous benzene flow at deep-bed conditions in the sample tube at 343 K in order to prevent condensation. It is conceivable that zeolite crystals in the center of the sample are less exposed to the gas flow and no benzene-copper interaction takes place in that fraction of the sample.

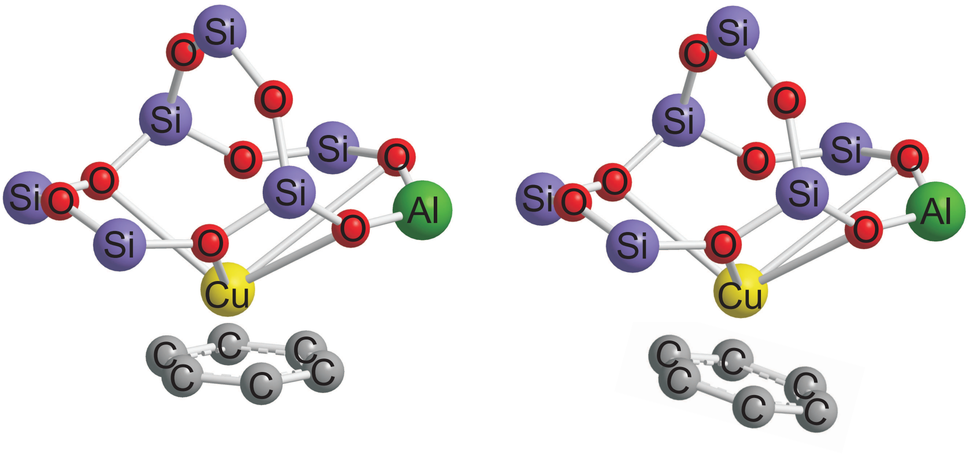

Figure 8.19: Sketch of a copper ion in the $\alpha3$ position interacting with a benzene molecule over its delocalized π-orbitals.

Interesting is also that ten times less benzene radicals are formed than Cu(II) is oxidized. Either not all radicals can be detected due due to fast recombination processes or not all benzene molecules interact the same way with copper. Only Cu(II) ions in favorable locations may interact strongly enough with benzene to form the benzene radical cation. It is interesting to notice that the Cu(II) ions which are not reduced by the benzene adsorption do suffer an environment change, observable through the change of the $g_{\|}$-factors.

The interaction of the single copper ions with the benzene molecules leads to a C-C bond weakening, as seen from the red shifted ν_{13} IR band and thus the activation of the molecule. It could be the result of π back-donation of d-electrons of Cu^{+} to π orbitals of carbon atoms in benzene. The LUMO orbital of benzene has only little antibonding character so that the electron transfer leads to only a small weakening of the C-C bond and thus only a small red shift ($\Delta\nu$ = -16 cm^{-1}).[20,21]

DFT calculations suggest that the zeolite framework gains a significant share of electrons in spite of its generalized anionic ligand character. Bridging oxygens accept part of excess electron density getting back their share from weakened O-Cu$^+$ bonds, while on the other hand the electron-rich basic framework donates electrons to the cation which in turn reinforces its back-donation capacity.[22] The almost non-existent shift of the C-H in-plane vibrations, compared to the large shift and splitting of the out of plane vibrations indicates that the benzene molecule interacts with copper over the delocalized π-orbitals as pictured in figure 8.19 and not via a C-H bond as it has been observed with ethane.[90] A tilted configuration is also plausible as it has been described by DFT calculations.[22]

The benzene cation radical formation on copper-free HZSM5 samples and the OH - benzene interaction are not yet clearly understood.[91] Theoretical calculations indicate that the nucleophilic character of benzene is increased inside the zeolite ring, suggesting the possible formation of a $\sigma - C_6H_7^+$ transition state for the transfer of the zeolite acid hydrogen toward the hydrocarbon molecule[17,19] or the formation of $[O_2^- \cdots C_6H_6^+]$ pairs[92] facilitating the cracking of benzene.

We studied also the effect that benzene adsorption has on the antiferromagnetically coupled copper oxide species, the bis(μ-oxo)- and ($\mu - \eta^2 : \eta^2$-peroxo) dimers. One of the dimers (C1) proved to be sensitive to both the adsorption of benzene (see 8.18) and oxygen (see 7.15(a)). While oxygen can dissociate the dimer, its interaction with benzene is not so strong. The second dimer C2 is insensitive to the adsorption of either benzene or oxygen.

CHAPTER 9

COMPETITIVE ADSORPTION OF OXYGEN AND BENZENE

The adsorption of oxygen and benzene was studied first independently of each other in order to be able to point out the active catalytic sites among the different adsorption sites. It was observed that both benzene and oxygen adsorb on the hydroxyl groups of the parent zeolite and the ion exchanged copper ions, a fact that could lead to a bifunctionality of the catalyst. They also interact with the dicopper peroxide complexes with oxygen being able to dissociate one of the complexes. While oxygen adsorption oxidizes the Cu(I) ions to Cu(II), benzene reduces the Cu(II) ions to Cu(I) providing an important premise for a catalytic cycle. Pure benzene adsorption on both copper-free and copper-containing HZSM5 zeolites leads to the formation of benzene radical cations. A radical mechanism for the oxidation process is thus plausible. For the desired oxidation reaction of benzene to phenol both benzene and oxygen must interact with the catalyst at the same time. This can be achieved either by adding both reactants simultaneously to the catalyst sample or by inserting them one after the other.

9.1 FTIR SPECTRA

9.1.1 Competitive Adsorption at Room Temperature

We are starting our study of the competitive adsorption of the reactants by analyzing first their consecutive adsorption on the zeolite at room temperature. There was no difference between the spectra of solid and liquid state ion exchanged samples so that we will present in this part the results obtained on one liquid ion exchanged sample only. The Cu/HZSM5 sample was exposed to 1 mbar equilibrium pressure of benzene at room temperature. The recorded benzene adsorption spectrum in figure 9.1 (a) presents a large number of vibration bands which have been discussed in detail in the previous chapter. The interaction of the benzene molecules with the hydroxyl groups of the zeolite is observ-

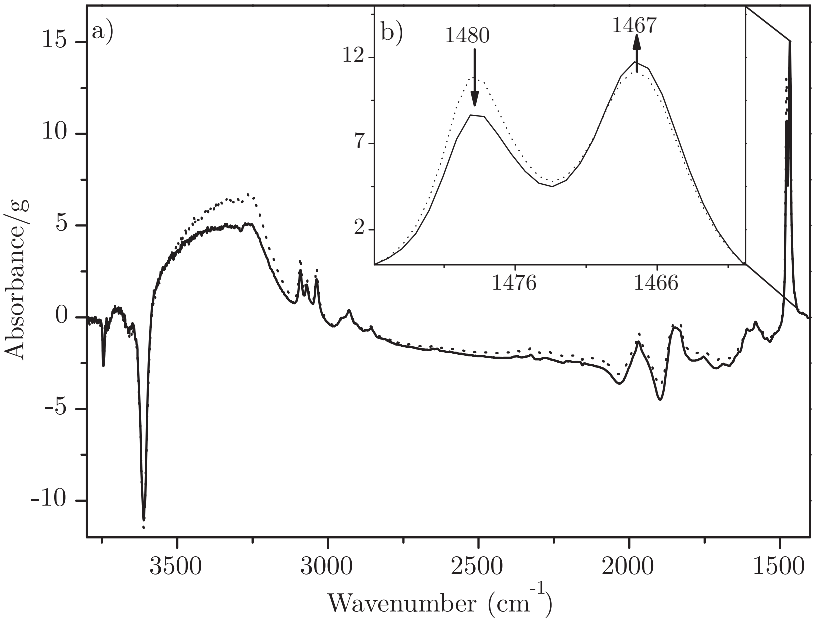

Figure 9.1: IR absorption bands after adsorption of 1 mbar equilibrium pressure of benzene on Cu/HZSM5 at room temperature (dotted line) and subsequent adsorption of 50 mbar equilibrium pressure of oxygen (solid line) (a) with the split ν_{13} C-C benzene stretching vibration enlarged (b).

able through the decrease of the intensity of the bands of the terminal Si(OH) groups (3745 cm^{-1}), bridging Si(OH)Al hydroxyl groups (3610 cm^{-1}) and extra lattice Al(OH) groups (3664 cm^{-1}), which in figure 9.1 (a) appear negative. The addition of 50 mbar equilibrium pressure of oxygen gas to the sample at room temperature causes a weakening of almost all benzene bands.

The strongest intensity loss is observable on the broad band between 3250 and 3450 cm^{-1}, generated by the overlapping of the signals of perturbed OH stretching vibrations. At the same time the intensity loss suffered by the hydroxyl groups is weakened and their signals grow slightly. This suggests that less benzene interacts with the OH groups. The splitting of the ν_{13} C-C benzene stretching vibration band at 1480 and 1467 cm^{-1} allows us to observe the benzene adsorption on the hydroxyl groups of the zeolite (the 1480 cm^{-1} line) and the copper ions (the 1467 cm^{-1} line) independently. With growing oxygen pressure (figure 9.1 b) the 1480 cm^{-1} signal of benzene adsorbed on the OH groups is weakened while the 1467 cm^{-1} line of benzene adsorbed on copper rises slightly. Their band areas were used for a site selective quantitative evaluation of the adsorbed benzene. At 1 mbar benzene equilibrium pressure the amount of benzene adsorbed on the copper ions is with 0.96 molecules/u.c. a little higher but still comparable to the 0.82 molecules/u.c. adsorbed on the hydroxyl groups. At this coverage both the copper ions and hydroxyl groups are not yet saturated (see figure 8.5). The adsorption of oxygen removes 0.16 molecules/u.c. from the hydroxyl groups

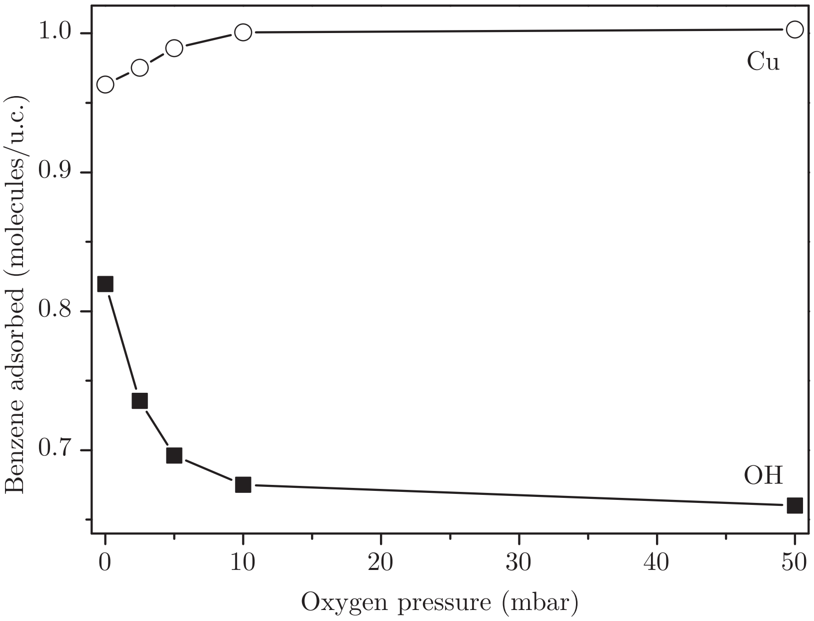

Figure 9.2: IR-derived adsorption isotherms of benzene adsorbed on copper (open circles) and OH groups (filled squares) in dependence of the oxygen equilibrium pressure.

(see figure 9.2). Only one fourth of the benzene removed from the OH groups adsorbs instead on copper, the rest is lost. This means that oxygen is the stronger adsorbate on the hydroxyl groups but not on copper, since it cannot remove any benzene adsorbed on copper but is able to displace some of the benzene from the OH groups. The displaced benzene molecules redistribute inside the zeolite pores, some being thus able to reach unoccupied copper sites, others possibly leaving the zeolite pore. At the same time no new IR lines appear so that there is no indication for the formation of any kind of benzene-oxygen complex. Further addition of benzene and oxygen did not offer any new insight. The adsorption of oxygen before the adsorption of benzene did not have any observable influence on the benzene adsorption behavior.

9.1.2 High Temperature Behavior of the Reactants

Thus we proceeded to heat up the sample after the adsorption of totally 70 mbar of oxygen and 30 mbar of benzene equilibrium pressure. There are mainly three processes which could occur with the rising temperature: complete combustion, the oxidation of benzene to phenol or other intermediates, or thermal desorption. All of them should lead to changes in the spectrum, loss of intensity and the appearance of new lines corresponding to phenol, water, carbon dioxide or free benzene. Only very weak gas phase benzene lines were observed during heating, so that simple thermal desorption can be neglected.

9.1.2.1 Reaction Products

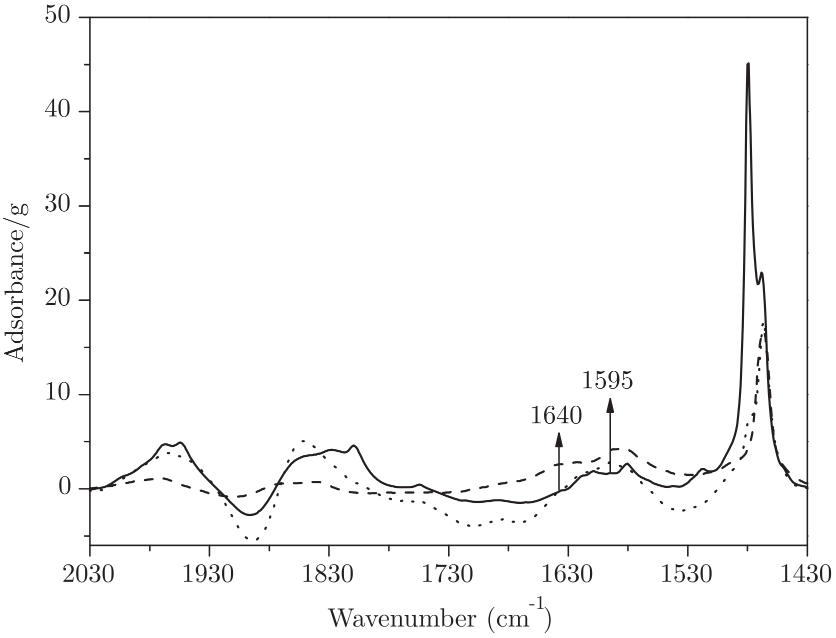

Figure 9.3: IR absorption bands after adsorption of 70 mbar of oxygen and 30 mbar of benzene equilibrium pressure on Cu/HZSM5 at room temperature (solid line), subsequent heating at 523 K (dotted line) and evacuation at room temperature for 48 h (dashed line)

By heating the sample the adsorption lines are getting broader and remain so even after cooling and evacuation for two days. As can be seen in figure 9.3 the broad spectrum makes it difficult to differentiate the signals. By taking different backgrounds and analyzing also the difference spectra we were able to pinpoint two strong new signals. The bands at 1640 and 1595 cm^{-1} persist even after evacuating the sample, proving their strong interaction with the catalyst. The 1640 cm^{-1} band indicates the formation of water. A strong broad signal around 2360 cm^{-1} belonging to carbon dioxide appears during heating but disappears on evacuation. The appearance of these two products is a clear evidence of the complete combustion of some of the previously adsorbed benzene. The 1595 cm^{-1} signal could be attributed to the C-C stretching vibration of phenol.[93] It matches the frequency of pure phenol adsorbed on Cu/HZSM5. It is not the most intensive line of phenol, but the other signals overlap with the benzene lines. When a Cu/HZSM5 sample with adsorbed phenol is heated, the bands become broad as in the case of adsorbed benzene or benzene with oxygen. This makes it even more difficult to distinguish between the signals of the products and those of the reactants.

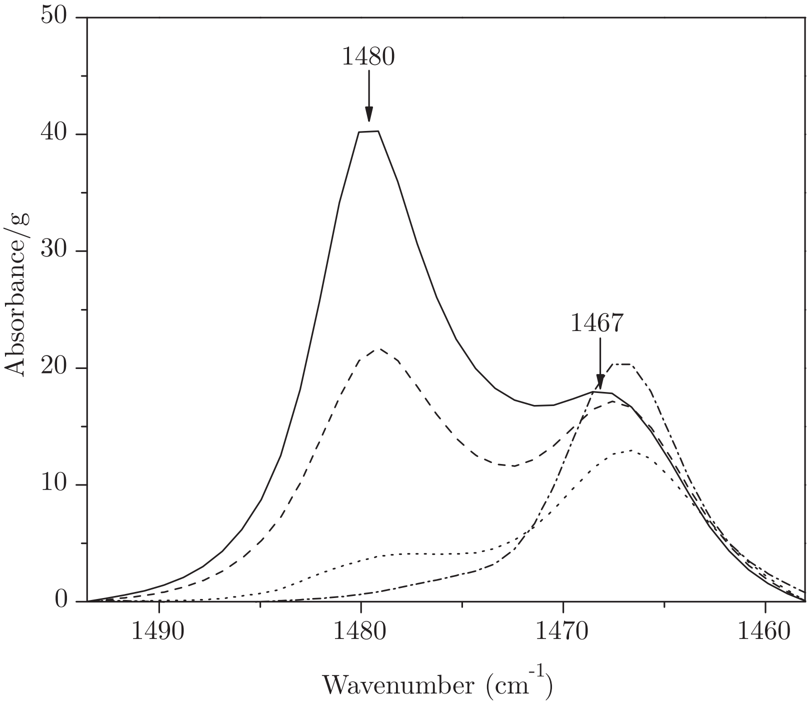

(a)

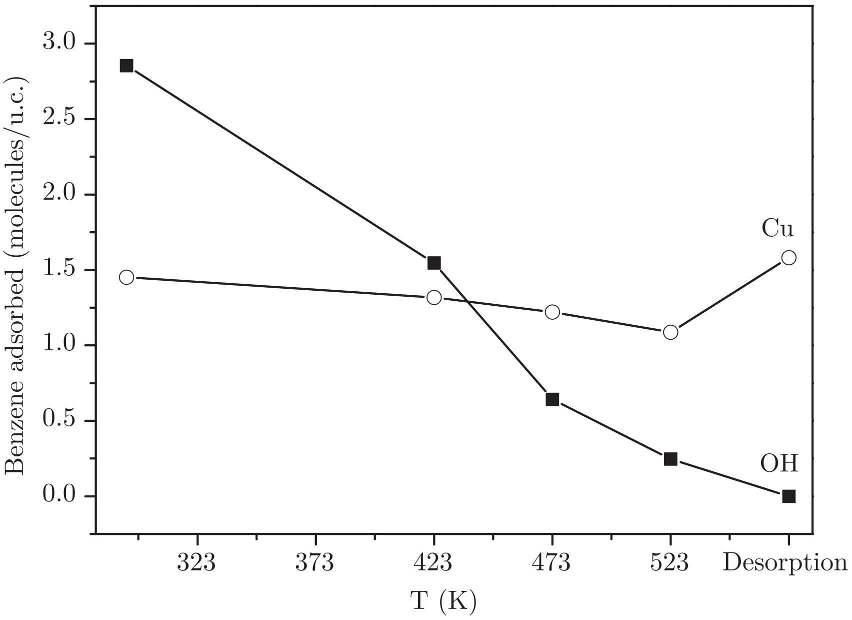

(b)

Figure 9.4: ν_{13} C-C benzene stretching vibration bands after adsorption of 70 mbar of oxygen and 30 mbar of benzene equilibrium pressure on Cu/HZSM5 at room temperature (solid line) and subsequent heating at 423 K (dashed line), 523 K (doted line) and subsequent desorption at room temperature for 48 h (dash doted line)((a)). IR-derived adsorption isotherms of benzene adsorbed on copper (open circles) and OH groups (filled squares) in dependence of the sample temperature with the value obtained after desorption displayed at the end of the scale ((b)).

9.1.2.2 Benzene Consumption on Copper vs. OH-Groups

In figure 9.4 (a) the ν_{13} C-C benzene stretching vibration band shows the loss in benzene that is interacting with the zeolitic OH-groups. The amount of benzene adsorbed on copper decreases only slightly. In figure 9.4 (b) the amounts of benzene/u.c. adsorbed on copper and OH-groups are plotted for the different sample temperatures. At 523 K 91% of the benzene adsorbed on OH groups has disappeared (from 2.85 to 0.24 molecules/u.c) while only a 25% loss (from 1.45 to 1.08 molecules/u.c) is observable on copper. So while almost all benzene adsorbed on the OH groups is consumed only very little of the benzene adsorbed on copper reacts. The stability of the benzene molecules adsorbed on copper is demonstrated well during the evacuation of the sample. Not only does benzene not desorb from copper but the copper ions also catch some of the molecules that desorbed from the hydroxyl groups. Compared to the 1.08 molecules/u.c. adsorbed on copper at 523 K, after cooling and evacuating the sample we measured a 45% gain in benzene adsorbed on copper to 1.58 molecules/u.c., which is 4% more even than the starting value. After the evacuation of the sample no more benzene adsorbed on hydroxyl groups is observable but no loss of hydroxyl groups could be noted. The phenol contribution to the ν_{13} band can be neglected.

9.1.2.3 Benzene Migration Route

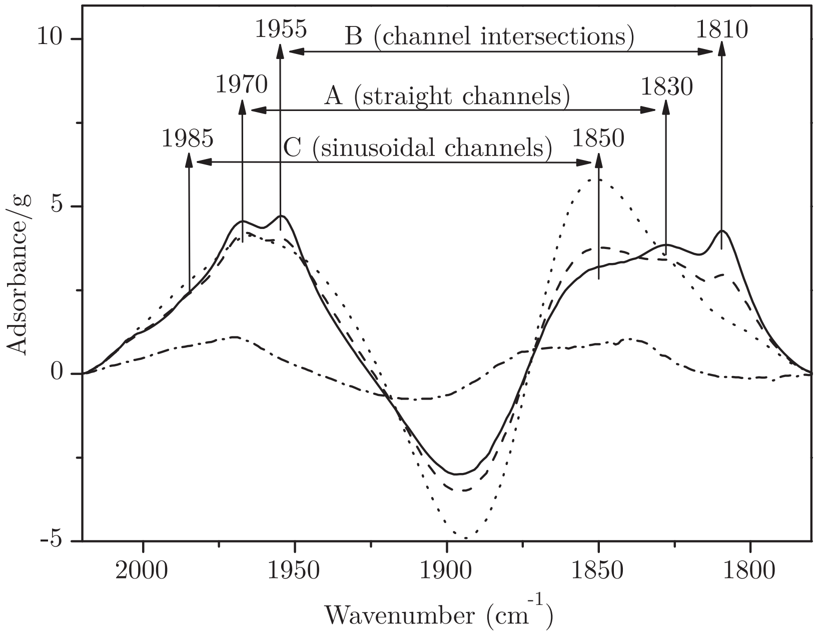

Figure 9.5: Splitting of the $(\nu_7 + \nu_{19})$ and $(\nu_{11} + \nu_{19})$ combination vibrations of benzene on CuHZSM5 at room temperature (solid line) and subsequent heating at 423 K (dashed line), 523 K (doted line) and subsequent desorption at room temperature for 48 h (dash doted line)

When benzene adsorbs on copper-free and copper-containing HZSM5 zeolites, the $(\nu_7 + \nu_{19})$ and $(\nu_{11} + \nu_{19})$ out of plane combination vibrations of benzene split into three sets of bands which allowed us to follow the adsorption route of the molecule through the zeolitic pore structure (see figure 9.5). The high frequency pair A (1970 and 1830 cm^{-1}) was assigned to benzene located in the straight channels, pair B (1955 and 1810 cm^{-1}) to molecules residing at the channel intersections and group C (1985 and 1850 cm^{-1}) to molecules in the sinusoidal channels. By observing these bands the route of the benzene migration was established in the previous chapter. The benzene molecules enter the zeolite structure through the straight channels, migrating then into the channel intersections. There up to 4 molecules/u.c. can be stabilized (one molecule at each intersection), a further increase of the loading pushes the molecules into the sinusoidal channels. The Cu/HZSM5 sample which was exposed to 70 mbar of oxygen and 30 mbar of benzene equilibrium pressure, contains 4.3 benzene molecules/u.c. meaning that the channel intersections are essentially full and some molecules already entered the sinusoidal channels.

In figure 9.5 the signal of the benzene molecules residing at the channel intersections (pair B) and in the straight channels (pair A) is diminishing with rising temperature, while there seems to be more benzene entering the sinusoidal channels (pair C). The rise in the intensity of the two lines forming pair C is asymmetric because the 1850 cm^{-1} line is overlapped by the signal of coke, so that only the 1985 cm^{-1} line is reliable. Still we can conclude that the benzene molecules located at the channel intersections react first followed closely by those in the straight channels. At 523 K only 1.33 molecules/u.c. are left and these are mostly adsorbed on copper. The study of the pure benzene adsorption suggested that little or no benzene-copper interaction takes place inside the sinusoidal channels. This means that the benzene molecules that are left are located mainly in the straight channels. This assumption is confirmed by the spectrum of the benzene molecules left in the sample after evacuation (figure 9.5, dash dot dotted line). Besides the coke signal, only pair A is still observable, proving that benzene remains only in the straight channels where it is strongly adsorbed on copper (figure 9.5 dash dot dotted line).

9.2 EPR SPECTRA

9.2.1 *g*-Factor Analysis

Benzene adsorption causes an amplitude decrease of the $g_{\|}$=2.31 and 2.32 signals of the two square pyramidal $\alpha 3$ and $\alpha 4$ Cu(II) species. At the same time a new

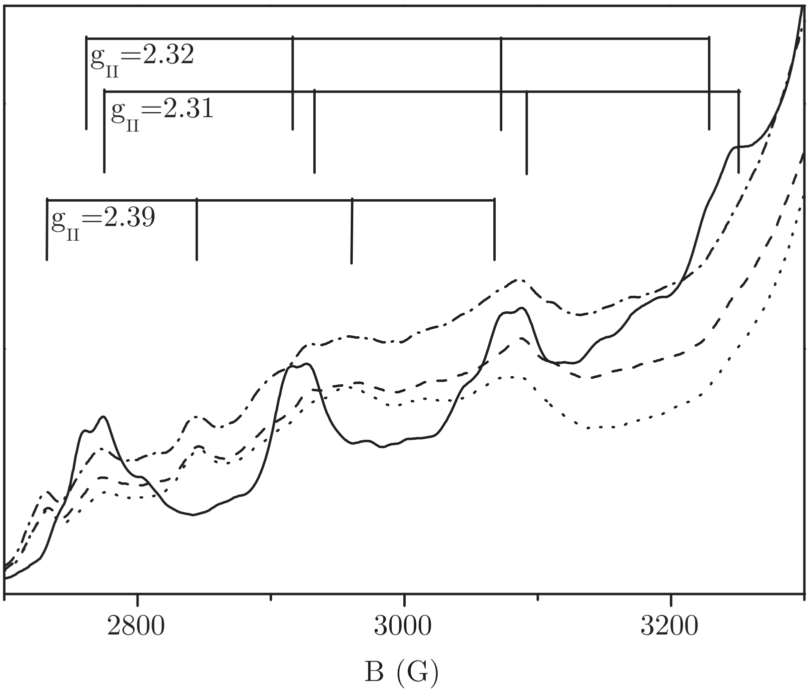

Figure 9.6: Parallel range of the Cu(II) EPR spectra with $g_{\|}$-factor assignment in Cu/HZSM5 zeolites at room temperature (solid line) followed by the adsorption of 3.5 molecules/u.c. of benzene (dash dotted line), 100 mbar equilibrium pressure of oxygen (dashed line) and subsequent heating of the sample at 373 K and cooling at room temperature for the measurement (dotted line). The spectrum was taken with a ZSM973 sample, but it is representative for all the samples independent of the ion exchange procedure.

signal with $g_{\|}$=2.39 grows in, which corresponds in value to hydrated octahedral copper ions. Subsequent addition of oxygen induces a further amplitude decrease of all the signals due to a small amount of spin exchange. The sample was then heated up to 373 K for 1 h and measured after cooling at room temperature. All signals suffer a further loss in amplitude.

When the order of the benzene and oxygen adsorption is interchanged the $g_{\|}$=2.39 signal appears only after the heating of the samples. Before this the spectrum is broadened strongly by spin exchange with oxygen. This means that when benzene is adsorbed on copper, there is less interaction taking place with the afterwards added oxygen than in the case when oxygen is adsorbed first. It is interesting to observe that even though not all Cu(II) ions have a benzene molecule directly adsorbed on them, the presence of the molecules in their vicinity seems to prevent their interaction with oxygen at room temperature. When oxygen is adsorbed first, spin exchange takes place, proving that the Cu(II) ions in their initial state are accessible for this kind of interaction. The subsequent adsorption of benzene does not directly lead to the appearance of the new signal, only after the heat treatment the new species is formed. Heating the samples reduces the broadening and the new signal becomes stronger and clearer.

9.2.2 Single Dose Adsorption

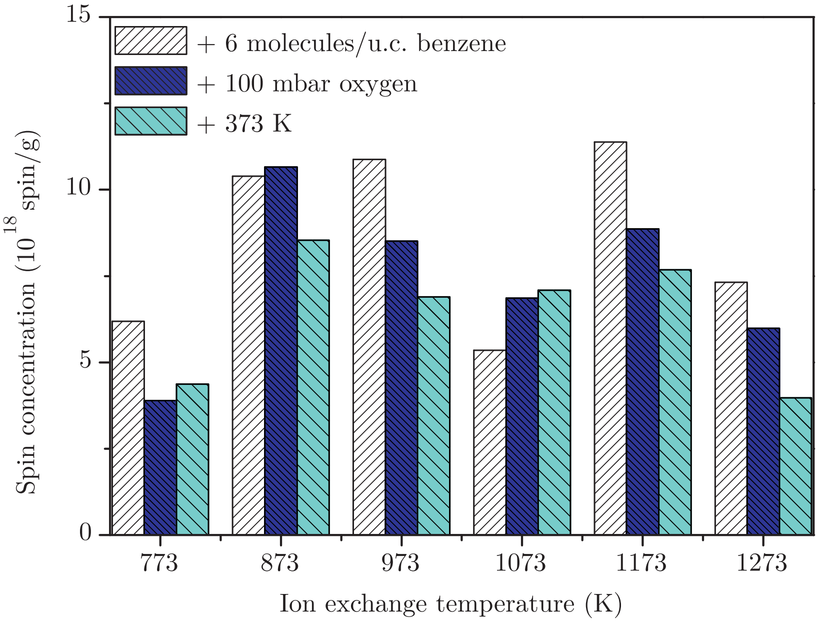

(a)

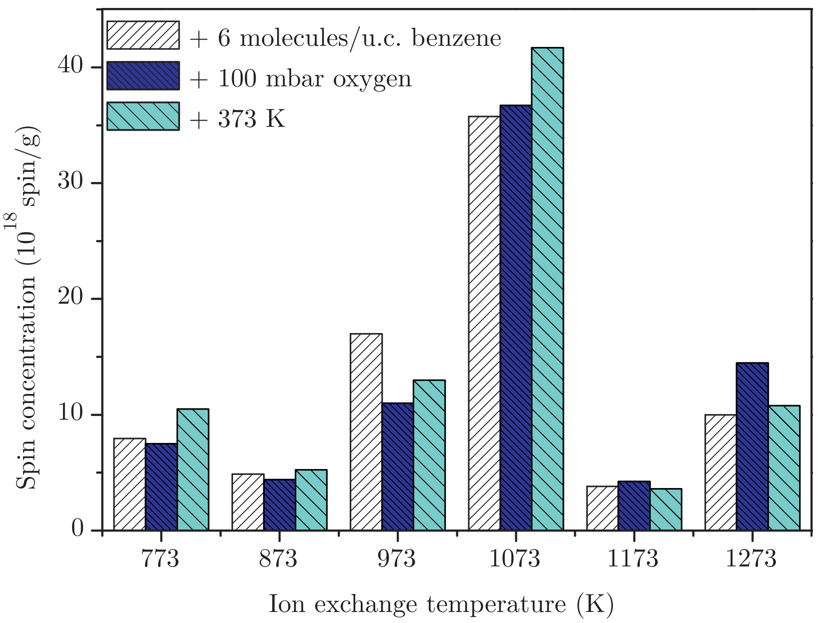

(b)

Figure 9.7: Spin concentration of two sets ((a) and (b)) of solid state ion exchanged Cu/HZSM5 zeolites after the adsorption of 6 molecules/u.c. of benzene (white bars), subsequent adsorption of 100 mbar equilibrium pressure of oxygen (blue bars) and subsequent heating of the sample at 373 K and cooling at room temperature for the measurement (cyan bars).

The solid state ion exchanged samples on which in the previous chapter 6 molecules/u.c. benzene were adsorbed (see figure 8.13), were used to simulate the oxidation reaction conditions. Thus their spin concentration was determined after the subsequent adsorption of 100 mbar equilibrium pressure of oxygen. As expected from the experience we have gained in the previous chapters concerning the stepwise adsorption of benzene and oxygen, the response of the samples to the oxygen addition differs strongly from sample to sample. We proceeded to heating the samples up to 373 K and measuring them after cooling. In the first charge (figure 9.7(a)) most samples showed a reduction in the spin concentration. Unfortunately, the reproduction of this behavior on a another set of samples (figure 9.7(b)) failed. This set indicated an oxidation of the copper ions after the heat treatment. Considering the fact that the changes in the spin concentration lie in the established error margin, a constant spin concentration could be assumed as well. Thus no clear trend could be determined proving again that this type of measurements is not sensitive enough.

9.2.3 Continuous Flow Measurements

In situ EPR measurements were performed at 473 K under a continuous flow of either $1.5{\cdot}10^{-5}$ mol s^{-1} benzene or $0.14 \cdot 10^{-5}$ mol s^{-1} oxygen or of both together. The deep-bed conditions in the sample tube prevent the interaction of the gases with the center of the sample so that not all of the sample responds to the adsorption. The separate adsorption of benzene on fresh samples causes the reduction of Cu(II) to Cu(I) and the adsorption of oxygen the oxidation of Cu(I) to Cu(II). Thus we would expect that the alternate adsorption of the benzene and oxygen would lead to an alternate reduction and oxidation of the copper ions facilitating a catalytic cycle. As shown in figure 9.8 this is not the case. The Cu(II) ions are reduced by benzene and the subsequent adsorption of oxygen is not able to oxidize them back. $3.5{\cdot}10^{18}$ spin/g are reduced by benzene on the solid state ion exchanged ZSM973 sample and $7{\cdot}10^{18}$ spin/g on the liquid ion exchanged Cu/HZSM5 sample. At this point both samples show saturation of the accessible Cu(II). Switching the benzene flow to an oxygen flow had no effect on the oxidation state of the ZSM973 sample. On the Cu/HZSM5 sample, oxygen manages to oxidize back about 3% of the copper ions, but a continuing alternate addition of benzene and oxygen does not change the already reached state.

In figure 9.8 the spin concentration of the samples is observed also when both gases are passed through the sample simultaneously. On both samples this also leads to an irreversible reduction of about 20% of the copper ions. Measurements with different flow rates and adsorption times were also performed for both types

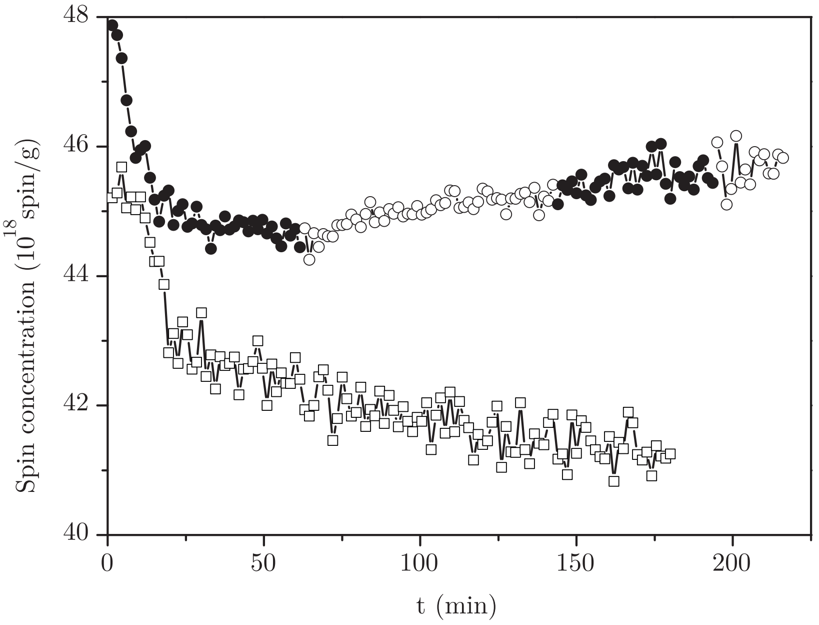

(a)

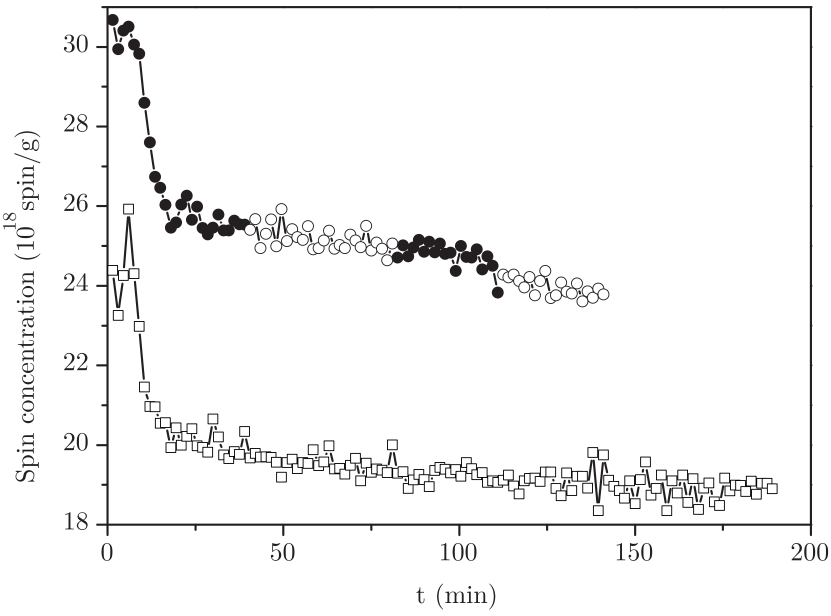

(b)

Figure 9.8: In situ spin concentration determination for a flow of 1.5$\cdot 10^{-5}$ mol s^{-1} of benzene (filled circles), 0.14 $\cdot 10^{-5}$ mol s^{-1} oxygen (open circles) and the simultaneous addition of both 1.5$\cdot 10^{-5}$ mol s^{-1} of benzene and $\cdot 10^{-5}$ mol s^{-1} oxygen (open squares) at 473 K on Cu/HZSM5 (a) and ZSM973 (b)

of measurements (simultaneous or alternate adsorption) but are not shown here since the behavior of the samples remained essentialy the same.

9.2.4 The Benzene Radical Cation

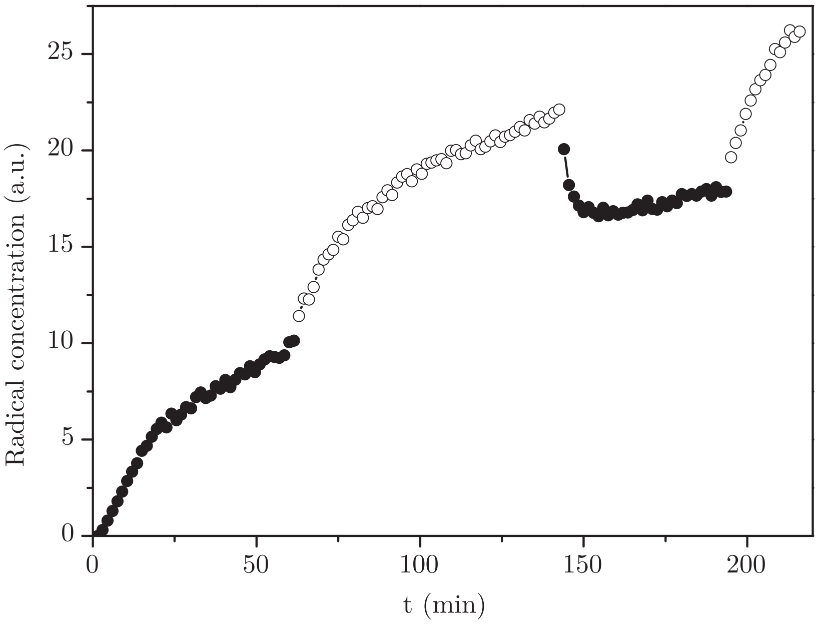

Figure 9.9: Relative radical concentration determination for an alternating flow of 1.5·10^{-5} mol/s of benzene (filled circles) and 0.14 ·10^{-5} mol/s oxygen (open circles) at 473 K on Cu/HZSM5.

Simultaneously with the appearance of the new $g_{\|}$=2.39 species the signal of the benzene radical cation (see figures 8.16 and 8.17) grows in. The determined overall spin concentration of the samples contains both the copper signal and the benzene radical cation. When oxygen is adsorbed the radical signal becomes more asymmetric, making it difficult to calculate its exact spin concentration. Thus we used the amplitude of the radical in order to observe its relative evolution.

On the solid state ion exchanged samples the radical signal is rather weak. While copper is reduced, the radical grows in when benzene is adsorbed on the sample, independently of oxygen being adsorbed first or not. It reaches its upper limit when the samples reaches saturation and remains constant through any following procedures. When benzene and oxygen are adsorbed simultaneously the radical is hardly observable.

In figure 9.9 the evolution of the amplitude of the radical signal of the liquid ion exchanged Cu/HZSM5 sample in figure 9.8 is plotted as it evolves during the alternate adsorption of benzene and oxygen. The radical signal grows with the amount of benzene adsorbed on the fresh sample and keeps growing even when the benzene flow is replaced by oxygen. This could explain the slight increase in the overall spin concentration of the sample. Intriguing is the fact that the radical signal is weakened if the oxygen is replaced again with a benzene flow and grows again when oxygen is switched back on. During the simultaneous adsorption of both gases the radical signal grows continuously. Even though the radical signal grows, the overall spin density of the sample reaches a constant level after the initial reduction suggesting that the two processes, radical formation and copper reduction, cancel each other out.

9.3 GC/MS MEASUREMENTS

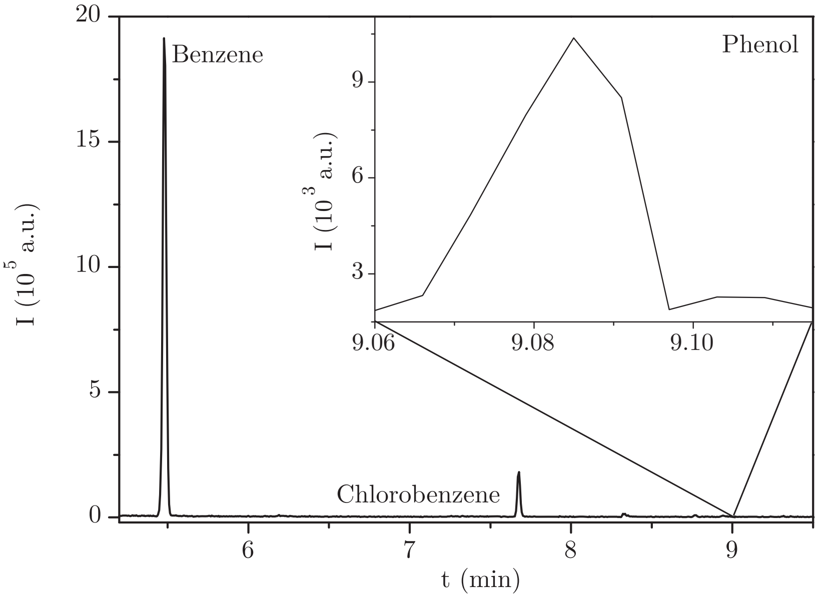

Figure 9.10: GC/MS spectrum of a ZSM973 sample dissolved in water and acetonitril after the adsorption of 6 molecules/u.c. benzene, 100 mbar equilibrium pressure oxygen and heating at 373 K. Note the change of scale.

The zeolite samples on which benzene and oxygen had been adsorbed, either stepwise or under continuous flow condition, and which afterwards had been heated up to simulate reaction conditions, were analyzed by gas chromatography. For this the samples were washed in a 1:1 water and acetonitril mixture which was then injected into a gas chromatograph with a mass spectrometer detector. On all the samples traces of phenol were detected besides large amounts of benzene. The amounts of phenol were so small that no reliable quantitative evaluation was possible (see figure 9.10). They prove though that the reaction takes place even at temperatures as low as 373 K. On the other hand, the large amount of benzene accumulated in the samples indicates that the small phenol yield is not caused by an insufficient adsorption capability of the zeolite. It indicates rather that from the large quantity of stored benzene only very little is able to react. On the solid state ion exchanged samples, which were ion-exchanged with

CuCl, chlorobenzene was additionally detected (see figure 9.10). Zeolite samples that had been exposed only to benzene were also analyzed but no products or intermediates were found.

The gas stream from the *in-situ* EPR measurements was directed into the GC/MS chromatograph for analysis too. In this case only benzene and oxygen that had bypassed the zeolite could be detected. With the built-in column, it was not possible to separate oxygen from water or carbon mono- or dioxide. The fact that no phenol could be detected this way may be caused by the insufficient strength of the carrier gas flow to desorb the product from the zeolite or by the possible condensation of phenol in the gas lines.

9.4 DISCUSSION

The study of the competitive adsorption of both gases determined that benzene is the stronger adsorbate than oxygen on copper, but not on the hydroxyl groups. The adsorption of benzene on the copper centers is so strong that it can hardly be removed through evacuation or even heating. When the sample is heated the benzene molecules adsorbed at the channel intersections react first. The heating of the sample removes or consumes almost all the benzene adsorbed on the hydroxyl groups, leaving only the molecules adsorbed on copper inside the straight channels of the zeolite. These strongly bound molecules block the straight channels of the zeolite which eventually leads to the poisoning of the catalyst. The chlorobenzene that was detected on solid state ion exchanged samples indicate that chlorine ions from the ion exchange process remain in the zeolite and could also lead to the poisoning of the catalyst.

Pure benzene adsorption leads to the formation of the benzene radical cations on copper-free and copper-containing HZSM5 zeolites. In the presence of oxygen the radical signal grows continuously even though the overall spin concentration of the sample remains constant. This could be achieved by a compensation through a further reduction of copper. As observed by FTIR oxygen can displace some of the benzene molecules adsorbed on the hydroxyl groups which then can reduce more copper ions to form additional radical cations.

When both reactants are adsorbed, benzene can be oxidized to phenol even at temperatures as low as 373 K. This low activation barrier presents a great advantage for it allows running the process at low temperatures and thus hopefully evade complete combustion. However, the determined phenol quantities were very small, indicating that from the large amounts of adsorbed benzene only very little could be oxidized.

CHAPTER 10

COMPARISON BETWEEN THE CU/HZSM5 AND CU/HY ZEOLITES

It is interesting to compare the Cu/HZSM5 zeolite with the Cu/HY zeolite, which has a more symmetric structure, is less polar and does not perform the benzene oxidation to phenol by gas phase oxygen. The copper content in Cu/HY is higher and the copper ions occupy only the two sites, SII and SIII. One dicopper peroxide complex was found in Cu/HY with a Cu-Cu distance of 3.21 Å in solid state ion exchanged samples and 2.9 Å in liquid ion exchanged samples. Both distances are smaller than the Cu-Cu distance of 3.33 Å found in solid state ion exchanged Cu/HZSM5. The Cu/HY has a higher abundance of dimers, a fact that suggest that the dimers are not essential, but if they nevertheless are, this may be related to the higher Cu-Cu separation and different isomers in Cu/HZSM5.

The adsorption of oxygen on Cu/HY leads to the oxidation of the copper ions to Cu(II), but in contrast to Cu/HZSM5 the hydroxyl groups showed only very weak interactions with the adsorbate and only at low temperatures.[75] This is attributed to the higher Brønsted acidity in Cu/HZSM5, due to its higher Si/Al ratio. These facts emphasize the importance of the bifunctionality of the Cu/HZSM5 zeolite where the hydroxyl groups and the copper ions work together.

On both ZSM5 and Y zeolites benzene adsorbs on copper and on the hydroxyl groups at room temperature. Cu(II) is reduced to Cu(I) and an organic radical is formed during the adsorption. On the Cu/HY zeolite the EPR signal is unresolved and cannot be accurately assigned, while on the Cu/HZSM5 the hyperfine septet of the benzene cation is clearly visible. For the CuHY zeolite a η^2-coordination to copper was calculated for benzene while on Cu/HZSM5 a higher coordination number is plausible. The involvement of the copper dimers in the benzene adsorption has not been reported on the faujasite. On Cu/HZSM5 one of the peroxide dimers is perturbed by benzene but does not dissociate.

For the competitive adsorption of benzene and oxygen on CuHY the theoretical calculations suggest that both reactants adsorb on the same copper ion. No intermediates or products besides coke could be determined.

The differences in symmetry, polarity, copper concentration and coordination are essential for the reaction involving the single copper units. Also the Na content of the samples seems to have different effects. On the CuNaY zeolite no copper reduction could be observed while on CuNaZSM5 the reduction process and radical formation runs unhindered though more slowly.

CHAPTER 11

CONCLUSIONS

The study of the initial state of the zeolite revealed the existence of mainly three possible catalytic centers: the single copper ions, the copper dimers and the Brønsted acid sites. The fact that both the copper ions and the Brønsted centers can interact with both benzene and oxygen can lead to an interplay of both sites during the oxidation reaction. The behavior of the Brønsted sites is one of the main differences between the Cu/ZSM5 and the catalytically inactive CuHY zeolites. This leads to the assumption that the reaction mechanism on the Cu/HZSM5 zeolite relies on the bifunctionality of the catalyst. The separate analysis of the adsorption of benzene and oxygen on copper exchanged HZSM5 samples suggested the possibility of a successful catalytic cycle also due to the reducing respectively oxidating effect of the two adsorbents on the copper ions.

On copper-free HZSM5 zeolites benzene radical cations are formed and oxygen interacts with the Brønsted sites but no phenol can be obtained. This leads to the assumption that copper plays another role besides the activation of the reactants. The high Si/Al ratio of Cu/HZSM5 (≈ 21) has the consequence that the second charge of the observed Cu(II) has to be compensated by the presence of a second Al ion or extra-framework anions, as in $[\mathrm{Cu(II)OH^-}]^+$ which may also be represented by the resonance structure $[\mathrm{Cu(I)OH^\bullet}]^+$. The homolytic dissociation of the $\mathrm{Cu(II)OH^-}$ into a Cu(I) ion and $\mathrm{OH^\bullet}$ radical should be energetically more convenient than the heterolytic dissociation into a Cu(II) and a $\mathrm{OH^-}$ ion. It means that hydroxyl radicals may become available from such a structure.

In figure 11.1 a reaction mechanism, formed of three intertwined cycles, is suggested. In cycle I the $[\mathrm{Cu(II)OH^-}]^+$ ion pair dissociates into a Cu(I) ion and $\mathrm{OH^\bullet}$ radical which enters cycle III. When hydrogen peroxide becomes available Cu(I) acts like a Fenton's reagent cleaving it into an $\mathrm{OH^-}$ ion and an $\mathrm{OH^\bullet}$ radical. The radical can enter cycle II, while the $\mathrm{OH^-}$ ion and the Cu(II) ions form back the initial ion pair closing the cycle.

Cycle II describes the phenol formation on copper. The adsorption of oxygen on copper forms a hybrid between Cu(I)-$\mathrm{O_2^\bullet}$ and Cu(II)-$\mathrm{O_2^-}$. This species can react

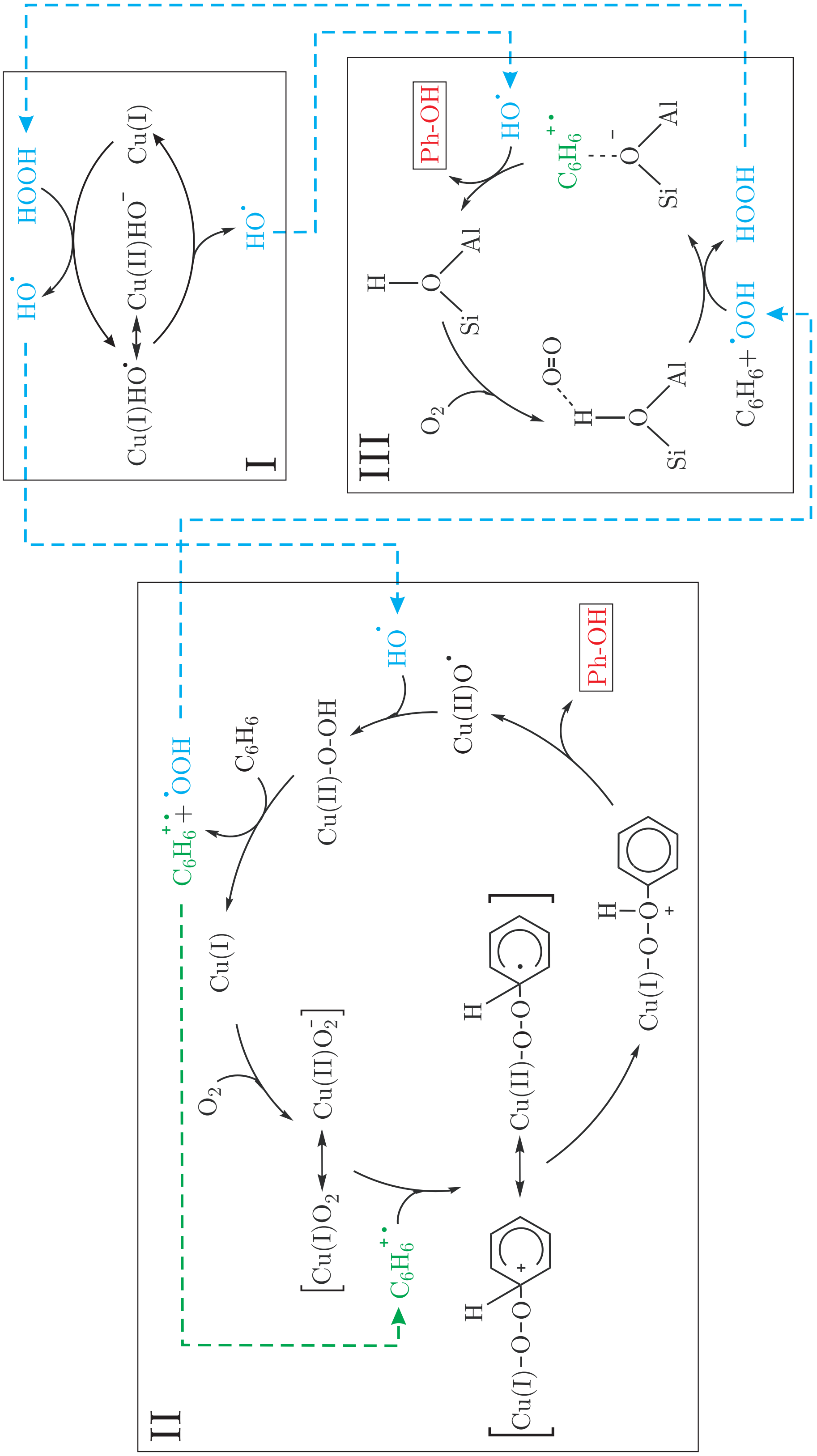
I
HOOH
HO•
Cu(I)HO•
Cu(II)HO⁻
Cu(I)
HO•
III
Ph-OH
HO•
C6H6+•
O⁻
Si
Al
H
O
Al
Si
HOOH
O2
O=O
H
O
Si
Al
C6H6+ •OOH
II
C6H6+• + •OOH
C6H6
Cu(II)-O-OH
HO•
Cu(II)O•
Ph-OH
Cu(I)
O2
Cu(II)O2⁻
[Cu(I)O2]
C6H6+•
H
Cu(I)-O-O
Cu(II)-O-O
H
Cu(I)-O-O
H

Figure 11.1: Reaction scheme for the oxidation of benzene to phenol on Cu/HZSM5.

with a benzene radical cation and eliminate a proton to restore the aromaticity. Through the oxidation of copper to Cu(II), the Cu(I)OOHC$_6$H$_5$ dissociates into a copper oxide radical and phenol. The copper oxide radical interacts with an OH$^\bullet$ radical to Cu(II)OOH. The cycle is closed by reducing the copper back to Cu(I) with a benzene molecule under the formation of a benzene radical cation, which can reenter the cycle and a OOH$^\bullet$ radical needed in cycle III.

Cycle III contains the contribution of the internal Si(OH)Al groups of the zeolite. The adsorption of oxygen on the Brønsted sites leads to the formation of an H-bonded complex. This complex can react with a benzene molecule and an OOH$^\bullet$ radical (formed in cycle II) under the formation of a benzene radical cation and hydrogen peroxide. This hydrogen peroxide enters then cycle I. If a hydroxyl radical (formed in cycle I) reacts with the benzene radical cation on the Brønsted site, phenol is formed and the catalytic cycle is closed. Thus phenol is formed both over the copper and the Brønsted sites, a fact which theoretically should lead to high yields. The main disadvantage of having three intertwined catalytic cycles is the fact that if one cycle is interrupted the others fail too.

There are a number of observations which support this proposal. The Y zeolite has a lower Si/Al ratio which reduces the necessity of extra-framework anions and thus the probability of finding hydroxyl radicals. Since the benzene oxidation to phenol does not take place on the Cu/HY zeolite, despite the fact that benzene radicals are formed, it can be assumed that on the Cu/HZSM5 zeolite the reaction is promoted by hydroxyl radicals. Another difference between the two zeolites lies in the interaction of the Brønsted sites with oxygen. On the Y zeolite oxygen does not adsorb on the hydroxyl groups invalidating thus cycle III. Without the involvement of the Brønsted sites no hydrogen peroxide could be formed and the hydroxyl radicals would be consumed fast and the whole catalytic cycle would fail.

While phenol and the benzene radical cations could be detected, the presence of hydrogen peroxide and the hydroxyl radicals could not be proved, a fact that could be explained through fast recombination processes. The interaction of copper and of the Brønsted sites with both oxygen and benzene was observed as well as the oxidation and reduction of the copper sites. The fact that no loss in Brønsted sites could be detected during the oxidation reaction supports their assumed role as catalysts.

In the copper exchanged HZSM5 samples two types of dicopper peroxide dimers were found, the bis(μ-oxo)- and ($\mu - \eta^2 : \eta^2$-peroxo) dimers. Oxygen adsorption cleaves one of them into two individual Cu(II)-O$_2^-$ units, though it is not yet clear which one of them is affected. Benzene adsorption causes a shift in the Néel temperature of the same dimer. While one of the dimers is not sensitive neither to benzene nor to oxygen, the other one is interacting with both substances and could thus promote the benzene to phenol oxidation by a parallel route. It is at this point not known whether the copper dimers are responsible in any part for the catalytic activity of the Cu/HZSM5 zeolites in the benzene oxidation. Since Cu/HY which has a higher abundance of dimers is inactive this may suggest that the dimers are not essential, but if they nevertheless are, this may be related to the higher Cu-Cu separation and different isomers in Cu/HZSM5.

Independent of the reaction path for the phenol formation the strong benzene copper interaction leads to poisoning of the catalyst. The inability to desorbe both benzene and phenol adsorbed on copper hinders the reoxidation of the sample and thus a successful catalytic cycle. The reaction takes place inside the channel intersections of the zeolite, leaving the benzene adsorbed on copper inside the straight channels uninvolved. This pore blocking hinders the phenol molecules from diffusing out of the zeolite structure and thus leads to a further poisoning of the catalyst and a difficult product extraction.

With the knowledge of the reaction mechanism on a molecular level, the specific tailoring of a new catalyst towards higher phenol yields would become possible. That catalyst would need the bifunctionality given by the interplay of the hydroxyl groups of the parent zeolite and the exchanged cations. The lattice must interact strongly enough with the reactants to activate them but also allow their desorption in order to prevent poisoning. It would be desirable to be able to isolate the ion exchange to the channel intersections, where the reaction then takes place, and leave the channels free for the products to diffuse out. It has been observed here that copper is not best suited to be the catalyst for this reaction, not because of lack of reactivity but because of the strength of its interaction with benzene and phenol which leads to a fast poisoning of the catalyst and thus to low yields and difficult product extraction.

CHAPTER 12

SUMMARY

The focus of this study lies in the understanding on a molecular level of the oxidation of benzene to phenol with molecular oxygen over copper-containing HZSM5 zeolites. This direct gas phase oxidation reaction would be a promising alternative to the Cumene process if the catalyst could be optimized to give higher yields. Thus we started our work by characterizing the initial state of the zeolite and the ion exchanged copper ions and then followed the changes they undergo during the adsorption of the reactants and the oxidation reaction. Hereby not only a qualitative analysis of the oxidation processes was performed, but a quantitative evaluation of the adsorbed molecules and the involved catalytic centers. By combining different experimental techniques (FTIR, EPR, XAFS, UV-Vis, GC/MS) with theoretical calculations and results obtained on the catalytically inactive CuHY zeolite, we were able to suggest a reaction path and determine the cause for the small phenol yields.

Since the copper ion exchange method has a tremendous influence on the amount of exchanged ions and their oxidation state, we observed in our study samples prepared by either liquid or solid state ion exchange, the latter performed at different temperatures, between 773 and 1273 K. The cation of the parent zeolite, also plays an important role, leading us to study both copper-free and copper-containing H- and Na-ZSM5 zeolites. After the ion exchange, no further oxidative or reductive treatment was applied to the samples. Thus, in their initial form, the zeolites contain a mixture of copper oxidation states, Cu(I) and Cu(II). We determined that independent of the preparation method the copper ions occupy three positions in the zeolite structure: the $\alpha 3$ and $\alpha 4$-sites (planar six-rings with an additional O-T-O bridge located at the surface of the straight channels) and the $\gamma 6$-sites (planar six-rings with an additional O-T-O-T-O bridge positioned at the channel intersections).[67] The copper content of the samples was determined to 5 - 10 wt.% (4.7 - 9.5 Cu/u.c.) for solid state ion exchanged samples dependig on the ion exchange temperature and around 1.3 wt.% (1.2 Cu/u.c.) for liquid ion exchanged HZSM5 or NaZSM5 samples (Cu/Al=0.34). From the total copper amount only 1-5% of the ions in the solid state ion exchanged samples are in the Cu(II) oxidation state, while in the samples prepared by liquid ion exchange 78% of the copper ions are Cu(II). In the solid state ion exchanged samples the total copper amount, the Cu(II) percentage and the oxidation state of the ions in the three different locations depend on the ion exchange temperatures. With rising ion exchange temperature the copper positioned at the $\gamma 6$-sites is found mainly in the Cu(I) oxidation state, while the Cu(II) amount in the $\alpha 4$-sites rises. For the $\alpha 3$-site the Cu(I)/Cu(II) ratio remains almost unchanged at different exchange temperatures. Both the total copper content and the Cu(II) percentage of the solid state ion exchanged samples presents a maximum at the ion exchange temperature of 973 K.

In literature besides single copper units, a wide range of possible copper oxygen complexes has been discussed, but no concurrent conclusions could be drawn. Single oxygen bridged EPR silent Cu(II)-O^{2-}-Cu(II) complexes[39,65,74] have been reported as well as dioxygen bridged species.[38,40,64,80] The study of the low temperature magnetic behavior of our samples resulted in the first experimental evidence of the antiferromagnetic behavior of the copper dimers in Cu/HZSM5 zeolites. The samples contain two types of antiferromagnetically coupled copper dimers, with Néel temperatures of 8 and 25 K. The large Cu-Cu separation of 3.34 Å, corresponds to the calculated value for the bent ($\mu - \eta^2 : \eta^2$-peroxo)dicopper core isomer $[Cu_2(\mu - \eta^2 : \eta^2\text{-}O_2)]^{2+}$.[38,40,67] The UV-Vis measurements suggested the presence of a mix of bis(μ-oxo)- and planar and bent ($\mu - \eta^2 : \eta^2$-peroxo) dimers. Together they make up 10% to 30% of the samples total copper content. The low energy barrier between the isomers suggests a facile pathway for the formation or cleavage of an O-O bond[38] which would be an important step for any oxidation reaction.

This was proven by the oxygen adsorption which cleaves irreversibly one of the dicopper complexes into single Cu(II)-O_2^- units. Oxygen adsorbs also on the single copper ions, oxidizing them under the formation of side-on bonded Cu(II)-O_2^- species. On the hydroxyl groups of the zeolite oxygen adsorbs not only at low but also at room temperature, forming a 1:1 H-bonded complex. The internal Si(OH)Al groups show the strongest interaction both with oxygen and benzene, compared to the other hydroxyl groups.

In literature the adsorption of benzene on plain HZSM5 zeolites has been studied[9–19] as well as on copper-exchanged HZSM5 samples[20–24], but no agreement was reached concerning the preferential adsorption sites, the coordination to copper and the activation of the molecule. Our study revealed not only the adsorption order on the different sites but also the diffusion path of the molecules inside the zeolite framework. The exact migration route of the molecules inside the zeolitic pores was determined by the observation of the benzene IR-adsorption bands at different loadings. The molecules enter the zeolite structure through the straight channels. When the benzene loading grows to 2 molecules/u.c. the second molecule enters the channel intersections. In the channel intersections up to 4 molecules/u.c, one molecule at each intersection, can be stabilized, a further increase of the loading pushing the molecules into the sinusoidal channels. Intriguing is the fact that on the NaZSM5 samples the behavior of the molecules seems to be exactly opposite, the molecules seemingly going from the sinusoidal into the straight channels and only at higher loadings into the channel intersections.

IR-derived site-specific adsorption isotherms allowed us to observe the benzene adsorption on copper independently from the adsorption on the hydroxyl groups. The adsorption isotherms of the hydroxyl groups describe the filling of the zeolite pores at the different locations (straight and sinusoidal channels and their intersections). The adsorption isotherms on copper show that the benzene adsorption on the copper centers precedes the benzene-OH interaction indicating that copper is the preferred adsorption site for benzene, but the copper centers are quickly saturated. The saturation limit is reached while the benzene molecules are accumulating in the channel intersections. There is no or only very little copper-benzene interaction in the sinusoidal channels. The overall adsorption order for Cu/HZSM5 zeolites is thus Cu > terminal Si(OH) > internal Si(OH)Al. On the liquid ion exchanged samples the saturation limit is reached at a benzene to copper ratio of 1, while on solid state ion exchanged samples only loadings of 0.4 molecules/Cu are reached. There is a maximal amount of copper that can interact with benzene. Any further increase in the copper concentration of the sample leads to no improvement of the zeolites adsorption capacity.

The almost non-existent shift of the C-H in-plane vibrations, compared to the large shift and splitting of the out of plane vibrations indicates that the benzene molecule interacts with copper over the delocalized π-orbitals and not via a C-H bond. It reduces the copper ions to Cu(I) under the formation of the benzene radical cation. It is interesting to notice that the Cu(II) ions which are not reduced by the benzene adsorption suffer a conformation change, observable through the change of the $g_{\|}$-factors. The presence of sodium ions does not hinder the process. The benzene cation radical formation on copper-free HZSM5 samples is not yet clearly understood.

One of the dicopper peroxide complexes is sensitive to both the adsorption of benzene and oxygen. While oxygen can dissociate the dimer, its interaction with benzene is not so strong, causing only a shift in the Néel temperature. Still, its interaction with both reactants could promote the benzene to phenol oxidation.

The second dimer is insensitive to the adsorption of either benzene or oxygen leading us to the assumption that its position is somewhat secluded, possibly in the sinusoidal channels.

The spectroscopic study of the competitive adsorption of both gases on Cu /HZSM5 zeolites both at room and high temperatures was performed in this study for the first time. It revealed that benzene is the stronger adsorbate than oxygen on copper, but not on the hydroxyl groups. When the sample is heated with oxygen and benzene, the benzene molecules located in the channel intersections react first. All benzene adsorbed on the hydroxyl groups is consumed. In contrast the copper ions in the straight channels tend to catch molecules displaced from the hydroxyl groups binding them strong enough to avoid desorption even after degassing, blocking thus the pores.

The formation of the benzene radical cation is enhanced by the presence of oxygen. In the *in-situ* continuous flow EPR measurements, every time oxygen was added to the sample, the increase of the radical concentration could be observed, which was compensated by a further reduction of the copper ions. While pure oxygen adsorption oxidizes the Cu(I) ions to Cu(II), pure benzene reduces the Cu(II) ions to Cu(I), an important premise for a catalytic cycle. Unfortunately when both reactants are adsorbed the oxidizing effect of oxygen cannot compensate the copper reduction.

The reaction occurs at temperatures as low as 373 K, but the determined phenol quantities were very small, indicating that from the large amounts of adsorbed benzene only very little could be oxidized. Since we observed a strong interaction of both reactants with the copper ions as well as with the hydroxyl groups, we suggest a reaction path which relies on the bifunctionality of the catalyst. The reaction mechanism consists of three intertwined cycles. The high Si/Al ratio of Cu/HZSM5 has the consequence that the second charge of the observed Cu(II) has to be compensated by the presence of a second Al ion or extra-framework anions, as in $[\mathrm{Cu(I)OH}^{\bullet}]^{+}$. The homolytic dissociation of this ion pair delivers hydroxyl radicals which drive the other two catalytic cycles. In both these cycles phenol is formed with not only copper but also the Brønsted sites acting as catalytic centers. Hydrogen peroxide is also formed and subsequently dissociated by copper through a Fenton's reaction. The interplay of both the copper ions and the Brønsted sites has the advantage that phenol is formed on both catalytic centers but if one cycle is interrupted the whole process fails.

Independent of the reaction path the strong benzene copper interaction hinders the desorption of both benzene and phenol. Thus the reoxidation of the sample fails and the catalytic cycle cannot be completed. The pore blocking of the benzene molecules hinders also the phenol molecules from diffusing out of the zeolite structure and thus leads to a further poisoning of the catalyst and a difficult product extraction.

The diffusion route through the zeolite pore structure and the adsorption order of benzene and oxygen on both copper and the hydroxyl groups of the ZSM5 zeolite has been determined quantitatively, so that the location of the molecules is known for any loading. This enabled the characterization of the catalyst during the oxidation process and thus the setup of a reaction mechanism. The knowledge of the reaction mechanism on a molecular level and of the factors hindering a successful catalytic cycle offers now the possibility of an intentional tailoring of a new catalyst.

CHAPTER 13

ZUSAMMENFASSUNG

Der Fokus dieser Arbeit liegt auf dem Verständnis des Oxidationsprozesses von Benzol zu Phenol mit molekularem Sauerstoff in kupferhaltigen HZSM5 Zeolithen auf molekularer Ebene. Diese direkte Gasphasen-Oxidation wäre eine viel versprechende Alternative zum Cumol-Verfahren, falls der Katalysator in Hinblick auf eine höhere Ausbeute optimiert werden könnte. Als erstes wurde deshalb der Anfangszustand des Zeolithen und der ausgetauschten Kupfer-Ionen charakterisiert und anschließend die Änderungen, die während der Adsorption der Reaktanden bzw. der Oxidationsreaktion auftreten, untersucht. Dabei wurde nicht nur eine qualitative Analyse des Oxidationsprozesses durchgeführt, sondern auch eine quantitative Evaluation der adsorbierten Moleküle und katalytischen Zentren. Durch die Kombination unterschiedlicher experimenteller Techniken (FTIR, ESR, XAFS, UV-Vis, GC/MS) mit theoretischen Rechnungen und Ergebnissen, die aus der Untersuch-ung von katalytisch inaktiven CuHY Zeolithen gewonnen wurden, war es möglich einen Reaktionsmechanismus für die Oxidation von Benzol zu Phenol vorzuschlagen und den Grund für die kleine Phenolausbeute zu ermitteln.

Da die Kupfer Austauschmethode einen großen Einfluss auf die Menge und den Oxidationszustand der ausgetauschten Ionen hat, wurden in dieser Arbeit Proben untersucht, die sowohl durch Flüssig- als auch durch Festkörperionenaustausch hergestellt wurden. Letzteres wurde bei unterschiedlichen Temperaturen, zwischen 773 und 1273 K durchgeführt.

Das Kation, welches durch Kupfer ersetzt wird, spielt auch eine wichtige Rolle, sodass sowohl kupferhaltige und kupferfreie H- als auch NaZSM5 Zeolithe untersucht wurden. Nach dem Ionenaustausch wurden die Proben keinen weiteren oxidierenden oder reduzierenden Behandlungen ausgesetzt und enthalten deshalb eine Mischung von Kupfer in den Oxidationsstufen Cu(I) und Cu(II). Die Kupfer-Ionen besetzten unabhängig von der Präparationsmethode drei Positionen in den Zeolithen: $\alpha 3$ und $\alpha 4$ (planare Sechsringe mit einer zusätzlichen O-T-O Brücke, lokalisiert an der Oberfläche der geraden Kanäle) und $\gamma 6$ (planare

Sechsringe mit einer zusätzlichen O-T-O-T-O Brücke, lokalisiert an den Kreuzungen der Kanäle). Der Kupfergehalt der Proben wurde mit 5 bis 10 gew% (4.7 - 9.5 Cu/EZ), abhängig von der Austauschtemperatur, für die Festkörper-ausgetauschten Proben und zu 1.3 gew.% (1.2 Cu/EZ) für flüssig-ausgetauschte HZSM5 und NaZSM5 Proben (Cu/Al=0.34) bestimmt. Bei den Festkörper-ausgetauschten Proben liegt zwischen 1 und 5% des Kupfers in der Oxidationsstufe II vor, während bei den flüssig-ausgetauschten Proben 78% als Kupfer(II) vorliegen. Die Ionenaustauschtemperatur hat bei der Festkörper-Methode einen großen Einfluss auf den Gesamtkupfergehalt, den Cu(II)-Anteil und den Oxidationszustand der Ionen an den unterschiedlichen Plätzen. Mit steigender Ionenaustauschtemperatur befinden sich die Kupfer-Ionen welche an den γ6-Plätzen lokalisiert sind, hauptsächlich im Oxidationszustand I, während der Cu(II)-Gehalt der α4-Plätze steigt. Auf den α3-Plätzen bleibt das Cu(I)/Cu(II)-Verhältnis nicht von der Ionenaustauschtemperatur beeinflusst. Sowohl der Gesamtgehalt an Kupfer als auch die Cu(II)-Konzentration der Festkörper-ausgetauschten Proben erreichen ihr Maximum bei einer Austauschtemperatur von 973 K.

In der Literatur wurden neben den einzelnen Kupfer-Ionen viele mögliche Kupfer-Sauerstoff-Komplexe diskutiert, doch konnte keine übereinstimmende Schlussfolgerung gezogen werden. Zu den vorgeschlagenen Komplexen zählen sowohl ESR-inaktive, durch ein einzelnes Sauerstoffatom überbrückte Cu(II)-O^{2-}-Cu(II) Komplexe[39,65,74], als auch solche die durch zwei Sauerstoffatome gebunden sind.[38,40,64,80] Durch die Tieftemperatur-Magnetisierungs-Messungen konnte das antiferromagnetische Verhalten der Kupferdimere in Cu/HZSM5 Zeolithen zum ersten mal experimentell nachgewiesen werden. Die Proben enthalten zwei Arten von antiferromagnetisch gekoppelten Kupfer-Dimeren mit Néel-Temperaturen von 8 und 25 K. Der große Cu-Cu Abstand von 3.34 Å stimmt mit dem errechneten Abstand für nicht-planare ($\mu-\eta^2:\eta^2$-peroxo) Kupfer-Isomere $[Cu_2(\mu-\eta^2:\eta^2\text{-}O_2)]^{2+}$[38,40,67] überein. Die UV-Vis Messungen weisen auf die Existenz einer Mischung aus den bis(μ-oxo) und den planar bzw. nicht-planaren ($\mu-\eta^2:\eta^2$-peroxo) Dimeren hin. Zusammen machen sie 10 bis 30% des gesamten Kupfermenge der Proben aus. Die niedrige Energiebarriere zwischen den Isomeren deutet auf eine leichte Bildung und Spaltung der O-O Bindung hin, was ein wichtiger Schritt für jede Oxidationsreaktion ist.

Dies wurde durch die Sauerstoffadsorption bewiesen, durch welche eines der Dimeren irreversibel in einzelne Cu(II)O Einheiten gespalten wird. Sauerstoff adsorbiert auch auf die einzelnen Kupfer-Ionen und oxidiert sie unter Bildung einer endständig gebundenen Cu(II)O Spezies. An den Hydroxylgruppen des Zeolithen adsorbiert Sauerstoff sowohl bei Tief- als auch bei Raumtemperatur unter Bildung eines 1:1 H-gebundenen Komplexes. In vergleich zu den anderen

OH-Gruppen weisen die internen Si(OH)Al Gruppen die stärkste Wechselwirkung sowohl mit Sauerstoff als auch mit Benzol auf.

In der Literatur wurde die Adsorption von Benzol sowohl auf kupfer-freien[9–19] wie auch auf kupfer-haltigen HZSM5 Proben[20–24] untersucht, wobei die Meinungen über die bevorzugten Adsorptionszentren, die Kupfer-Koordination und die Aktivierung der Moleküle stark divergieren. In dieser Arbeit konnte nicht nur die Adsorptionsreihenfolge auf den unterschiedlichen aktiven Zentren sondern auch die Diffusionsroute der Moleküle durch die Zeolithstruktur bestimmt werden. Diese Route konnte durch die Untersuchung der Adsorptionsbanden von Benzol bei unterschiedlichen Beladungen bestimmt werden. Die Moleküle diffundieren zuerst in die geraden Kanäle des Zeolithen. Wenn die Benzolbeladung auf 2 Moleküle/EZ. wächst, tritt das zweite Molekül in die Kanalkreuzung ein. In den Kreuzungen können bis zu 4 Moleküle/EZ stabilisiert werden, wobei sich in jeder Kreuzung ein Molekül befindet. Eine weitere Erhöhung der Beladung drückt die Moleküle in die sinusoidalen Kanäle. Im Gegensatz dazu wurde bei dem NaZSM5 Zeolith eine inverse Diffusionsroute gefunden. Die Benzolmoleküle wandern von den sinusoidalen Kanälen aus in die Geraden und erst bei hohen Beladungen in die Kreuzungen.

Die IR-abgeleiteten Adsorptionsisothermen erlauben es uns die Adsorption von Benzol auf Kupfer unabhängig von der Adsorption auf den Hydroxylgruppen zu beobachten. Die Adsorptionsisothermen der Hydroxylgruppen beschreiben die Auffüllung der Zeolithporen an den unterschiedlichen Plätzen (den geraden und sinusoidalen Kanälen und deren Kreuzungen), während die Adsorptionsisothermen der Kupfer-Ionen zeigen, dass Benzol wahrscheinlicher an die Kupfer-Zentren adsorbiert, wobei diese schnell gesättigt werden. Die Sättigungsgrenze wird erreicht, während die Benzolmoleküle die Kanalkreuzungen auffüllen. Es gibt keine oder fast keine Benzol-Kupfer Wechselwirkung in den sinusoidalen Kanälen. Die Reihenfolge der Adsorption ist Cu > terminale Si(OH) > interne Si(OH)Al. Auf den flüssig-ausgetauschten Proben wird die Sättigung bei einem Benzol zu Kupfer Verhältniss von 1 erreicht, während auf den festkörper-ausgetauschten Proben nur ein Verhältnis von 0.4 erreicht werden kann. Es gibt eine maximale Anzahl von Kupfer-Zentren die mit Benzol wechselwirken können. Eine weitere Steigerung der Kupferkonzentration führt zu keiner Verbesserung der Adsorptionskapazität des Zeolithen.

Die fast nicht vorhandene Verschiebung der C-H in-plane Schwingungen, verglichen mit der starken Verschiebung und Spaltung der out of plane Schwingungen weist darauf hin, dass die Benzol-Moleküle mit den Kupfer-Ionen durch ihre delokalisierten π Orbitale wechselwirken und nicht über eine C-H Bindung. Die Kupfer-Ionen werden dabei unter Bildung von Benzol-Radikal-Kationen zu Cu(I) reduziert. Anhand der g-Faktoren lässt sich feststellen, dass die Umgebung der Cu(II)-Ionen, die nicht durch die Benzoladsorption reduziert werden, geändert wird. Dieser Prozess ist unabhängig von der Anwesenheit von Natrium. Die Bildung der Benzol-Radikal-Kationen auf kupferfreien HZSM5 Zeolithen ist noch nicht geklärt.

Eines der Kupferperoxid Dimere ist sowohl gegenüber der Adsorption von Sauerstoff als auch von Benzol empfindlich. Während Sauerstoff das Dimer spaltet, ist dessen Wechselwirkung mit Benzol nicht so stark und führt deshalb nur zu einer Verschiebung der Néel Temperatur. Trotzdem könnten seine Wechselwirkungen mit beiden Reaktanden die Bildung von Phenol fördern. Das zweite Dimer ist unempfindlich gegenüber der Adsorption von Sauerstoff als auch von Benzol, was zur Annahme führt, dass dieses wahrscheinlich in den sinusoidalen Kanälen lokalisiert ist.

In dieser Arbeit wurde die kompetitive Adsorption beider Gase auf Cu/HZSM5 Zeolithen bei Raum- und Hochtemperatur zum ersten mal spektroskopisch untersucht. Die Messungen ergaben, dass Benzol der stärkere Adsorbant auf Kupfer, aber nicht auf den Hydroxylgruppen ist. Wenn die Proben nach der Adsorption beider Gase erhitzt werden, reagieren die Benzol-Moleküle aus den Kanalkreuzungen als Erste. Alle Benzol-Moleküle, die an den Brönsted-Zentren gebunden sind, werden verbraucht. Im Gegensatz dazu neigen die Kupfer-Zentren aus den geraden Kanälen dazu, Benzol-Moleküle, die von den Hydroxylgruppen desorbiert wurden, abzufangen und so stark zu binden, dass diese nicht mehr desorbiert werden können und die Poren blockieren.

Die Bildung der Benzol-Radikal-Kationen wird durch die Zugabe von Sauerstoff verstärkt. Wenn der Sauerstoffzufluss in den *in-situ*-ESR-Durchfluss-Messungen eingeschalten wurde konnte die Zunahme der Radikalkonzentration beobachtet werden, die von einer weiteren Reduktion von Kupfer kompensiert wurde. Während die Adsorption von reinem Sauerstoff Cu(I) zu Cu(II) oxidiert, reduziert Benzol Cu(II) zu Cu(I), eine wichtige Vorrausetzung für einen katalytischen Zyklus. Da die oxidierende Wirkung von Sauerstoff nicht ausreicht, um die Reduktion der Kupfer-Zentren zu kompensieren wenn beide Reaktanden gleichzeitig adsorbiert werden, kommt die Reaktion zum Erliegen.

Die Reaktion findet auch bei niedrigen Temperaturen (373 K) statt. Die gemessenen Phenolmengen waren sehr klein, was für einen geringen Umsatz des adsorbierten Benzols spricht. Da eine starke Wechselwirkung beider Reaktanden sowohl mit den Kupfer-Zentren als auch mit den Hydroxylgruppen nachweisbar war, wird ein Reaktionspfad vorgeschlagen, welcher auf der Bifunktiona-lität des Katalysators beruht. Der Reaktionsmechanismus besteht aus drei ineinander greifende Kreisprozesse. Das hohe Si/Al Verhältniss in den Cu/HZSM5

Zeolithen hat als Folge dass die Ladung der beobachteten Cu(II) Ionen durch ein zweites Al oder anderes Anion kompensiert werden muss, wie zum Beispiel $[\mathrm{Cu(I)OH}^{\bullet}]^{+}$. Die homolytische Spaltung dieses Ionenpaares liefert Hydroxyl-Radikale welche die anderen zwei katalytischen Zyklen antreiben. Phenol wird in beiden dieser Kreisprozesse erzeugt, wobei sowohl die Kupfer-Ionen als auch die Brønsted-Säuregruppen als katalytische Zentren agieren. Dabei wird auch Wasserstoffperoxid erzeugt und nachträglich durch Kupfer über eine Fentons Reaktion zersetzt. Das Zusammenspiel der Kupfer- und Brønsted-Zentren hat den Vorteil dass auf beiden Phenol erzeugt wird. Der Nachteil besteht darin, dass der gesammte Kreisprozess unterbrochen wird, wenn ein Zyklus zum Stehen kommt.

Unabhängig von dem Reaktionspfad verhindert die starke Benzol-Kupfer Wechselwirkung die Desorption von Benzol und Phenol. Dadurch kann der Katalysator nicht reoxidiert werden und der katalytische Zyklus wird unterbrochen. Die Verstopfung der Poren durch Benzol-Moleküle verhindert, dass die Phenol-Moleküle aus den Zeolithen heraus diffundieren können, was zu einer weiteren Vergiftung des Katalysators und zu einer erschwerten Produktextraktion führt.

Die Diffusionsroute durch die Porenstruktur des Zeolithen und die Reihenfolge der Adsorption von Sauerstoff und Benzol auf Kupfer und den Hydroxylgruppen des ZSM5 Zeolithen wurden quantitativ bestimmt, so dass die Position der Moleküle bei jeder Beladung bekannt ist. Dadurch wurde die Charakterisierung des Katalysators während der Oxidationsreaktion und die Aufstellung eines Reaktionsmechanismus ermöglicht. Die Kenntnis des Reaktionsmechanismus auf molekularer Ebene und der Faktoren, die den Kreisprozess stören, eröffnet die Möglichkeit der gezielten Entwicklung eines neuen Katalysators.

CHAPTER 14

ABBREVIATION LIST

α	absorption coefficient
α	electron spin state with M_S=-1/2
β	electron spin state with M_S=+1/2
χ	anharmonicity constant
χ	volume magnetic susceptibility
δ	retardation
$\epsilon(\tilde{\nu})$	extinction coefficient
φ	angle
φ	phase
$\Delta\varphi$	phase difference
γ	magnetogyric ratio
λ	spin-orbit coupling constant
λ	wavelength
μ	reduced mass
μ_0	vacuum permeability
μ_e	electron magnetic moment
μ_B	Bohr magneton
μ_J	total magnetic moment
μ_N	nuclear magneton
μ_n	nuclear magnetic moment
ν	frequency
ν_{vib}	vibration frequency
ν_{rot}	rotation frequency
$\tilde{\nu}$	wavenumber
θ	angle
θ	Curie-Weiss temperature
ω	angular velocity
ω	Larmor frequency
$\psi(r)$	electron wave function

$\|\psi(0)\|^2$	probability of finding the electron at the nucleus
a	charge of the metal ion
a	hyperfine coupling constant
A	area
A	absorbance
A_{max}	maximal band absorbance
$\underline{A}$	hyperfine coupling tensor
B	rotational constant
B_e	rotational constant for a vibrational-free state
$\vec{B}$	external magnetic field
B_0	magnitude of the external magnetic field
B_m	modulation amplitude
BET	equation for specific area determination
BS	beam splitter
ΔB	half width at half maximum
c	speed of light
c	concentration
cxx, yy, zz	direction cosines
C_i	dicopper complex
d	d-orbital function
D	dissociation energy
D_e	centrifugal constant
DFT	density functional theory
e	electron charge
E	total energy
E_i	vibrational energy
E_p	potential energy
E_{rot}	rotational energy
EPR/ESR	electron paramagnetic/spin resonance
EXAFS	extended X-ray absorption fine structure
EZ	Einheitszelle
F_G	Gauss function
F_L	Lorentz function
FTIR	Fourier transform infrared
gg-factor, Land	e factor
g_e	free electron *g*-factor
G	vibrational term value
G	gain of signal amplifier
GC	gas chromatography

h	Planck's constant
$\hbar$	$h/2\pi$
H	Hamilton operator
I	moment of inertia
$I(\varphi)$	interferogram
I	quantum number of the nuclear spin
$\vec{I}$	nuclear spin angular momentum
I_0	intensity of the incident beam
IR	infrared
J	rotational quantum number
J	spin quantum number of the total angular momentum
J	electron exchange coupling constant
$\vec{J}$	total angular momentum
k	spring constant
l	thickness
L	orbital spin quantum number
$\vec{L}$	orbital angular momentum
m	mass
m_e	electron mass
m_p	proton mass
M	metal ion
M	molar mass
M	magnetization
$M_{1,2}$	mirror
M_I	magnetic quantum number of the nuclear spin
M_S	magnetic quantum number of the electron spin
MS	mass spectroscopy
N	number of atoms
N	degrees of freedom
NMR	nuclear magnetic resonance
p	pressure
P_B	vapor pressure of benzene
r	distance
$\vec{r}$	unit vector in r direction
R	integrated fraction of total spectrum
R_0	universal gas constant
S	electron spin quantum number
$\vec{S}$	spin angular momentum
$S(\tilde{\nu})$	spectrum

t	time
T	temperature
T	tetrahedrally coordinated atom
T	rotational-vibrational term value
T	transmittance
T_C	Currie temperature
T_N	Neél temperature
u.c.	unit cell
UV-Vis	ultraviolet-visible range
v	velocity
v_i	vibrational quantum number
V(r)	potential
wt.	weight
XANES	X-ray absorption near edge spectroscopy
XAS	X-ray adsorption spectroscopy
Z	atomic number
Z	zeolite framework
X	spin concentration

HZSM5	acid form of the ZSM5 zeolite
Cu/HZSM5	copper-containing HZSM5 zeolite, liquid ion exchanged
CuNaZSM5	copper-containing NaZSM5 zeolite, liquid ion exchanged
NaZSM5	sodium form of the ZSM5 zeolite
ZSM973	copper-containing HZSM5 zeolite, labeled with the temperature of the solid state ion exchange

LIST OF FIGURES

1.1 Cumene process 7

2.1 Scheme of the construction of the ZSM5 framework from pentasil units (A) linked to form chains (B). The resulting channel system (E) is sketched with the projections along the straight (C) and sinusoidal channels (D). 10
2.2 The ZSM5 structure with indication of the six-ring sites α, β and γ and the planar five-ring δ. 15

3.1 1-Dimensional anharmonic potential and energy levels. 20
3.2 Sketch of a FTIR Spectrometer. 27

4.1 The electron Zeeman splitting of the M_S states of a S=1/2 system, at increasing external magnetic field. 30
4.2 The vector addition of the orbital and spin magnetic moments. . . . 31
4.3 Zeeman and hyperfine splitting of the energy levels of an atom with S=1/2 and I=3/2 like in the case of Cu^{2+}. 33
4.4 Level scheme for the d-orbitals in a tetragonally compressed octahedral crystal field. 36
4.5 Direction cosines of the external magnetic field B_0. 37
4.6 Inverse magnetic susceptibility as a function of temperature for a antiferromagnet and ferromagnet. 39

5.1 Amount of ion exchanged copper in weight percent and percentage of Cu(II) of the total amount of exchanged copper vs. the ion exchange temperature of the samples 42
5.2 Sketch of the sample pellet mounted on a movable plate which enables to move the sample perpendicular to the optical path of the spectrometer, so as to observe only the very thin edge of the pellet. 43
5.3 Sketch of the experimental setup built for continuous flow EPR measurements. 46

5.4 EPR double resonator cavity. The modified suprasil tube for continuous flow measurements is inserted with the heating tube in the back resonator. The standard sample is placed in the front resonator. The iris tunes the microwave for the whole cavity so that the same conditions exist in both resonators. 47

6.1 FTIR spectrum of a HZSM5 sample at different positions of the sample cell. The spectrum series depicts the intensity loss while moving the sample from the position of its full thickness (dashed line) towards the edge (dotted line). 52

6.2 The spectral range of the hydroxyl groups of a HZSM5 sample. . . 53

6.3 Cu(II) EPR spectra with general $g_{\|}$ and $g_{\perp}$-factor assignment for a copper ion with axial symmetric coordination. The spectrum was taken with a ZSM973 sample at room temperature, but it is representative for all the samples independent of the ion exchange procedure 54

6.4 Parallel range of the Cu(II) EPR spectra with $g_{\|}$-factor assignment in Cu/HZSM5 zeolites at room temperature. The spectrum was taken with a ZSM973 sample, but it is representative for all the samples independent of the ion exchange procedure. 55

6.5 Structure of the (a)$\alpha 3$, (b) $\alpha 4$ and (c) $\gamma 6$ sites in Cu/HZSM5[67]. . . . 55

6.6 Fractions of the Cu(II) sites $\gamma 6$, $\alpha 3$ and $\alpha 4$ as determined from the $g_{\|}$ species assignment in solid state ion exchanged samples at different ion exchange temperatures, measured at room temperature. 56

6.7 Magnetization plot of a solid state ion exchanged ZSM973 sample. The spectrum is representative for all the samples independent of the ion exchange procedure. 57

6.8 Diffuse reflectance UV-Vis spectrum of a fresh solid state ion exchanged sample (ZSM973) (solid line) and the deconvoluted dicopper peroxide bands (dotted lines). 57

6.9 Possible dicopper oxygen complexes in Cu/HZSM5 zeolites with the Cu-Cu and Cu-O bond distances in Å.[38,40,67,73] 58

7.1 $^{16}O_2$ (solid line) and $^{18}O_2$ (dotted line) IR absorption bands after adsorption of 200 mbar equilibrium pressure of oxygen on Cu/HZSM5 at 80 K. 61

7.2 Difference spectra in the range of the hydroxyl stretching modes of Cu/HZSM5 during the adsorption of 20 mbar (solid line), 40 mbar (dotted line) and 200 mbar (dashed line) equilibrium pressure $^{16}O_2$ at 80 K. 62

7.3 Integrated absorption of the $^{16}O_2$ adsorption band at 1549 cm^{-1} and of the hydroxyl groups of Cu/HZSM5. 63

7.4 Lattice vibration bands before (dotted line) and after $^{16}O_2$ (solid line) adsorption on Cu/HZSM5 at room temperature and 200 mbar oxygen equilibrium pressure. 65

7.5 $^{16}O_2$ (solid line) and $^{18}O_2$ (dotted line) absorption bands on Cu/HZSM5 in the zeolite framework vibration region at room temperature and 200 mbar oxygen equilibrium pressure. 65

7.6 Absorption bands on Cu/HZSM5 in the zeolite framework vibration region at room temperature after the adsorption of 400 mbar oxygen equilibrium pressure (solid line) and subsequent evacuation for 15 minutes (dashed line) and 250 minutes (dotted line). . . 66

7.7 Absorption bands of carbon mono- and dioxide and nitrogen impurities on Cu/HZSM5 at room temperature. 67

7.8 Absorption bands on Cu/HZSM5 in the zeolite framework vibration region at room temperature after the adsorption of 60 mbar hydrogen equilibrium pressure. 68

7.9 Cu/HZSM5 zeolite before (solid line) and after the adsorption of 100 mbar equilibrium pressure O_2 (dotted line) at room temperature. Spectra representative for both liquid and solid state ion exchanged samples. 69

7.10 EPR lines of 10^{-8} $mol{\cdot}g^{-1}$ of molecular oxygen in Cu/HZSM5. . . . 70

7.11 EPR lines of $8.28{\cdot}10^{-8}$ $mol{\cdot}g^{-1}$ of molecular oxygen (solid line), $9.90{\cdot}10^{-8}$ $mol{\cdot}g^{-1}$ (dashed line) and $14.85{\cdot}10^{-8}$ $mol{\cdot}g^{-1}$ (dotted line) in Cu/HZSM5. 71

7.12 Spin concentration change of a solid state ion exchanged Cu/HZSM5 sample during the stepwise adsorption of aliquots of $9.75{\cdot}10^{-9}$ mol/g of oxygen (open triangle). Oxygen was adsorbed in equal amounts on a second sample (open circles) which was then degassed and exposed again to the same procedure (full circles) (integration range 2450-3950 G). The arrows indicate the point at which the samples stop adsorbing and the oxygen gas phase signal appears. 72

7.13 Spin concentration of two different charges of solid state ion exchanged Cu/HZSM5 samples (a) and (b) in their initial state (white bars), after the adsorption of 100 mbar equilibrium pressure of oxygen (blue bars) and subsequent degassing for 180 minutes at room temperature (cyan bars). 73

7.14 Spin concentration change of a solid state ion exchanged Cu/HZSM5 (ZSM973) under 2 ml·min^{-1} continuous flow of oxygen at room temperature, with 200 ml·min^{-1} continuous flow of helium as carrier gas (integration range 2450-3950 G). 74

7.15 (a) Magnetization plot before (squares) and after 100 mbar oxygen adsorption (triangles) on solid state ion exchanged ZSM973. (b) Magnetization plot after oxygen adsorption (circles) and subsequent desorption (triangles) on solid state ion exchanged ZSM973. 76

8.1 Benzene IR absorption bands after adsorption of 0.025 mbar equilibrium pressure of benzene on Cu/HZSM5 at room temperature. . 79

8.2 Splitting of the benzene vibration bands on Cu/HZSM5 82

8.3 Splitting of the $(\nu_7 + \nu_{19})$ and $(\nu_{11} + \nu_{19})$ combination vibrations of benzene on Cu/HZSM5 (dotted line), CuZSM5700 (dashed line) and NaZSM5 (solid line) at a loading of 5.5 molecules/u.c. at room temperature. 84

8.4 Splitting of the ν_{13} C-C stretching vibration of benzene into the adsorption on the OH groups (1479 cm^{-1}) and on copper (1468 cm^{-1}) on Cu/HZSM5 at room temperature 85

8.5 IR-derived adsorption isotherm of benzene adsorbed on copper (open circles) and OH groups (filled squares) on Cu/HZSM5. The amount of Cu/u.c. in the sample is indicated by the dashed line, the H$^+$/u.c. amount by the dotted line. 86

8.6 IR-derived adsorption isotherm of benzene adsorbed on copper (open circles) and OH groups (filled squares) on ZSM973. The amount of Cu/u.c. in the sample is indicated by the dashed line. . 87

8.7 IR-derived adsorption isotherm of benzene adsorbed on copper (open circles) and OH groups (filled squares) on CuNaZSM5. The amount of Cu/u.c. in the sample is indicated by the dashed line, the H$^+$/u.c. amount by the dotted line. 87

8.8 IR-derived adsorption isotherm of benzene adsorbed on OH groups (filled squares) on NaZSM5. 88

8.9 Benzene molecules adsorbed on Copper and Cu(II) 89

8.10 IR bands in the zeolite framework vibrations region after the adsorption of benzene on Cu/HZSM5 at 0.25 (solid line), 0.5 (dashed line), 1 (dotted line) and 10 mbar (dash-dotted line) benzene equilibrium pressure at room temperature. 91

8.11 Parallel range of the Cu(II) EPR spectra with $g_{\|}$-factor assignment in Cu/HZSM5 zeolites at room temperature before (solid line) and after the adsorption of 6 molecules/u.c. (dotted line). The spectrum was taken with a ZSM973 sample, but it is representative for all the samples independent of the ion exchange procedure. 91

8.12 Spin concentration of two different charges (a) and (b) of solid state ion exchanged samples (ZSM773 (open square), ZSM873 (full circle), ZSM973 (full triangle), ZSM1073 (full square), ZSM1173 (open circle), ZSM1273 (open triangle)) as a function of the adsorbed benzene dose (1.2 molecules/u.c.) at room temperature. The error bars of $2{\cdot}10^{18}$ spins/g are not plotted for the sake of clarity. 92

8.13 Spin concentration of two different charges (a) and (b) of solid state ion exchanged samples as a function of the ion exchange temperature before and after the adsorption of 6 molecules/u.c. of benzene at room temperature. 93

8.14 In situ spin concentration determination for a benzene continuous flow of $1.5{\cdot}10^{-5}$ mol/s at 343 K for Cu/HZSM5 (squares), ZSM973 (empty circles) and CuNaZSM5 (filled circles). Values contain both the Cu(II) and the radical spins. Note the change of scale for the three curves. 94

8.15 Cu/HZSM5 EPR spectra under a continuous benzene flow of $1.5{\cdot}10^{-5}$ mol/s at 343 K. 95

8.16 Benzene radical cation signal measured (dotted lines) and simulated (solid lines) on Cu/HZSM5 (a) and HZSM5 (b). 96

8.17 Normalized benzene radical cation measured on Cu/HZSM5 (solid line) and ZSM973 (dotted line) at 373 K after the adsorption of 100 mbar equilibrium pressure of benzene 97

8.18 Magnetization plot before (circles) and after the adsorption of 0.1 molecules/u.c. (filled squares) and subsequent further adsorption of 0.4 molecules/u.c. (filled triangles) of benzene on Cu/HZSM5. . 98

8.19 Sketch of a copper ion in the $\alpha 3$ position interacting with a benzene molecule over its delocalized π-orbitals. 99

9.1 IR absorption bands after adsorption of 1 mbar equilibrium pressure of benzene on Cu/HZSM5 at room temperature (dotted line) and subsequent adsorption of 50 mbar equilibrium pressure of oxygen (solid line) (a) with the split ν_{13} C-C benzene stretching vibration enlarged (b). 102

9.2 IR-derived adsorption isotherms of benzene adsorbed on copper (open circles) and OH groups (filled squares) in dependence of the oxygen equilibrium pressure. 103

9.3 IR absorption bands after adsorption of 70 mbar of oxygen and 30 mbar of benzene equilibrium pressure on Cu/HZSM5 at room temperature (solid line), subsequent heating at 523 K (dotted line) and evacuation at room temperature for 48 h (dashed line) 104

9.4 ν_{13} C-C benzene stretching vibration bands after adsorption of 70 mbar of oxygen and 30 mbar of benzene equilibrium pressure on Cu/HZSM5 at room temperature (solid line) and subsequent heating at 423 K (dashed line), 523 K (doted line) and subsequent desorption at room temperature for 48 h (dash doted line)((a)). IR-derived adsorption isotherms of benzene adsorbed on copper (open circles) and OH groups (filled squares) in dependence of the sample temperature with the value obtained after desorption displayed at the end of the scale ((b)). 105

9.5 Splitting of the $(\nu_7 + \nu_{19})$ and $(\nu_{11} + \nu_{19})$ combination vibrations of benzene on CuHZSM5 at room temperature (solid line) and subsequent heating at 423 K (dashed line), 523 K (doted line) and subsequent desorption at room temperature for 48 h (dash doted line) . . 106

9.6 Parallel range of the Cu(II) EPR spectra with $g_{\|}$-factor assignment in Cu/HZSM5 zeolites at room temperature (solid line) followed by the adsorption of 3.5 molecules/u.c. of benzene (dash dotted line), 100 mbar equilibrium pressure of oxygen (dashed line) and subsequent heating of the sample at 373 K and cooling at room temperature for the measurement (dotted line). The spectrum was taken with a ZSM973 sample, but it is representative for all the samples independent of the ion exchange procedure. 108

9.7 Spin concentration of two sets ((a) and (b)) of solid state ion exchanged Cu/HZSM5 zeolites after the adsorption of 6 molecules/u.c. of benzene (white bars), subsequent adsorption of 100 mbar equilibrium pressure of oxygen (blue bars) and subsequent heating of the sample at 373 K and cooling at room temperature for the measurement (cyan bars). 109

9.8 In situ spin concentration determination for a flow of $1.5{\cdot}10^{-5}$ mol s^{-1} of benzene (filled circles), $0.14\ {\cdot}10^{-5}$ mol s^{-1} oxygen (open circles) and the simultaneous addition of both $1.5{\cdot}10^{-5}$ mol s^{-1} of benzene and ${\cdot}10^{-5}$ mol s^{-1} oxygen (open squares) at 473 K on Cu/HZSM5 (a) and ZSM973 (b) 111
9.9 Relative radical concentration determination for an alternating flow of $1.5{\cdot}10^{-5}$ mol/s of benzene (filled circles) and $0.14\ {\cdot}10^{-5}$ mol/s oxygen (open circles) at 473 K on Cu/HZSM5. 112
9.10 GC/MS spectrum of a ZSM973 sample dissolved in water and acetonitril after the adsorption of 6 molecules/u.c. benzene, 100 mbar equilibrium pressure oxygen and heating at 373 K. Note the change of scale. 113

11.1 Reaction scheme for the oxidation of benzene to phenol on Cu/HZSM5.118

LIST OF TABLES

5.1 Physical properties of the samples determined from nitrogen adsorption isotherms . . . 42

6.1 Summary of the structural and spectroscopic properties of the dicopper oxide complexes.[73] . . . 58

8.1 Assignment of observed spectrum of benzene adsorbed on Cu/HZSM5 and wavenumber shift relative to the gas phase.[88] . . . 80
8.2 Benzene loadings at which the split $(\nu_7 + \nu_{19})$ and $(\nu_{11} + \nu_{19})$ combination vibrations of benzene appear first, in molecules/u.c.. . . . 83

BIBLIOGRAPHY

[1] R. Hamada, Y. Shibata, S. Nishiyama and S. Tsuruya, *Phys. Chem. Chem. Phys.*, 2003, **5**, 956–965.

[2] A. Kubacka, Z. Wang, B. Sulikowski and V. C. Corberan, *J. Catal.*, 2007, **250**, 184–189.

[3] A. Waclaw, K. Nowinska and W. Schwieger, *Appl. Catal. A: Gen*, 2004, **270**, 151–156.

[4] H. Yamanaka, R. Hamada, H. Nibuta, S. Nishiyama and S. Tsuruya, *J. Mol. Catal. A*, 2002, **178**, 89–95.

[5] T. Kitamura, H. Kanzaki, R. Hamada, S. Nishiyama and S. Tsuruya, *Can. J. Chem.*, 2004, **82**, 1597–1605.

[6] T. Archipov, S. Santra, A. B. Ene, H. Stoll, G. Rauhut and E. Roduner, *J. Phys. Chem. C*, 2009, **113**, 4107–4116.

[7] C. Förste, A. Germanus, J. Kärger, H. Pfeifer, J. Caro, W. Pilz and A. Zikanova, *J. Chem. Soc. Faraday Trans. 1*, 1987, **83**, 2301–2309.

[8] S. J. Reitmeier, R. R. Mukti and J. A. Lercher, *J. Phys. Chem. C*, 2008, **112**, 2538–2544.

[9] A. Zecchina, C. Versino, A. Appiano and G. Occhiena, *J. Phys. Chem.*, 1968, **72**, 1471–1474.

[10] D. B. Shah, C.-J. Guo and D. T. Hayhurst, *J. Chem. Soc. Faraday Trans.*, 1995, **91**, 1143–1146.

[11] R. L. Portsmouth, M. J. Duer and L. F. Gladden, *J. Chem. Soc. Faraday Trans.*, 1995, **91**, 559–567.

[12] E. Roduner, M. Stolmar and H. Dilger, *J. Phys. Chem. A*, 1998, **102**, 7591–7597.

[13] Y. Huang and E. A. Havenga, *J. Phys. Chem. B*, 2000, **104**, 5084–5089.

[14] R. Goyal, A. N. Fitch and H. Jobic, *J. Phys. Chem. B*, 2000, **104**, 2878–2884.

[15] A. Sahasrabudhe, V. S. Kamble, A. K. Tripathi and N. M. Gupta, *J. Phys. Chem. B*, 2001, **105**, 4374–4379.

[16] A. K. Tripathi, A. Sahasrabudhe, S. Mitra, R. Mukhopadhyay, N. M. Gupta and V. B. Kartha, *Phys. Chem. Chem. Phys.*, 2001, **3**, 4449–4455.

[17] E. Roduner and H. Dilger, *J. Am. Chem. Soc.*, 2001, **123**, 7717–7718.

[18] S. I. Reshetnikov, S. B. Ilyin, A. A. Ivanov and A. S. Kharitonov, *React. Kinet. Catal. Lett.*, 2004, **83**, 157–164.

[19] I. P. Zaragoza, J. M. Martinez-Magadan, R. Santamaria, D. Dixon and M. Castro, *Int. J. Quantum. Chem.*, 2000, **80**, 125–132.

[20] E. Broclawik, P. Kozyra and J. Datka, *C. R. Chimie*, 2005, **8**, 491–508.

[21] E. Kukulska-Zajac, P. Kozyra and J. Datka, *Appl. Catal. A: Gen.*, 2006, **307**, 46–50.

[22] P. Kozyra, J. Zalucka, M. Mitoraj, E. Broclawik and J. Datka, *Catal. Lett.*, 2008, **126**, 241–246.

[23] V. A. Bolshov and A. M. Volodin, *React. Kinet. Catal. Lett.*, 1991, **43**, 87–91.

[24] A. N. Il'ichev, V. A. Matyshak and V. N. Korchak, *Mendeleev Commun.*, 1999, **1**, 27–29.

[25] M. Weber, M. Weber and M. Kleine-Boymann, *Ullmann's Encyclopedia of Industrial Chemistry*, Wiley VCH, 1998.

[26] C. Friedel and J. M. Crafts, *Ann. Chim. (Paris)*, 1888, **14**, 935.

[27] B. Lücke, K. V. Narayana, A. Martin and K. Jähnisch, *Adv. Synth. Catal.*, 2004, **346**, 1407–1424.

[28] J. Weitkamp and L. Puppe, *Catalysis and Zeolites*, Springer, Berlin, 1999.

[29] H. van Bekkum, E. M. Flanigen, P. A. Jacobs and J. C. Jansen, *Introduction to Zeolite Science and Practice*, Elsevier, Amsterdam, 2001.

[30] J. B. Nagy, P. Bodart, I. Hannus and I. Kiricsi, *Synthesis, characterisation and use of zeolitic mesoporous materials*, DecanGen Ltd., Szeged, 1998.

[31] N. Y. Chen, W. E. Garwood and F. G. Dwyer, *Shape Selective Catalysis in Industrial Applications*, Marcel Dekker Inc., New York, 1989.

[32] Y. Kuroda, A. Kotani, H. Maeda, H. Moriwaki, T. Morimato and M. Nagao, *J. Chem. Soc. Faraday Trans.*, 1992, **88**, 1583–1590.

[33] W. Grunert, N. W. Hayes, R. W. Joyner, E. S. Shpiro, M. R. H. Siddiqui and G. N. Baeva, *J. Phys. Chem.*, 1994, **98**, 10832–10846.

[34] M. H. Groothaert, K. Lievens, H. Leeman, B. M. Weckhuysen and R. A. Schoonheydt, *J. Catal.*, 2003, **220**, 500–512.

[35] P. Nachtigall, D. Nachtigallova and J. Sauer, *J. Phys. Chem. B*, 2000, **104**, 1738–1745.

[36] A. V. Kucherov, H. G. Karge and R. Schlögl, *Microporous Mesoporous Mater.*, 1998, **25**, 7–14.

[37] N. B. Castagnola, A. J. Kropf and C. L. Marshall, *Appl. Catal. A: Gen.*, 2005, **290**, 110–122.

[38] B. R. Goodman, K. C. Hass, W. F. Schneider and J. B. Adams, *J. Phys. Chem. B*, 1999, **103**, 10452–10460.

[39] M. J. Rice, A. K. Chakraborty and A. T. Bell, *J. Phys. Chem. B*, 2000, **104**, 9987–9992.

[40] B. R. Goodman, W. F. Schneider, K. C. Hass and J. B. Adams, *Catal. Lett.*, 1998, **56**, 183–188.

[41] J. Dedecek and B. Wichterlova, *Phys. Chem. Chem. Phys.*, 1999, **1**, 629–637.

[42] S. C. Larsen, A. Aylor, A. T. Bell and J. A. Reimer, *J. Phys. Chem.*, 1994, **98**, 11533–11540.

[43] J. Sarkany, J. L. Ditri and W. M. H. Sachtler, *Catal. Lett.*, 1992, **16**, 241–249.

[44] M. Anpo, M. Matsuoka, Y. Shioya, H. Yamashita, E. Giamello, C. Morterra, M. Che, H. H. Patterson, S. Webber, S. Ouellette and M. A. Fox, *J. Phys. Chem.*, 1994, **98**, 5744–5750.

[45] G. T. Palomino, P. Fisicaro, S. Bordiga, A. Zecchina, E. Giamello and C. Lamberti, *J. Phys. Chem. B*, 2000, **104**, 4064–4073.

[46] P. J. Smeets, M. H. Groothaert, R. M. van Teeffelen, H. Leeman, E. J. M. Hensen and R. A. Schoonheydt, *J. Catal.*, 2007, **245**, 358–368.

[47] B. R. Goodman, K. C. Hass, W. F. Schneider and J. B. Adams, *Catal. Lett.*, 2000, **68**, 85–93.

[48] M. J. Rice, A. K. Chakraborty and A. T. Bell, *J. Catal.*, 1999, **186**, 222–227.

[49] S. Sklenak, J. Dedecek, C. Li, B. Wichterlova, V. Gabova, M. Sierka and J. Sauer, *Phys. Chem. Chem. Phys.*, 2009, **11**, 1237–1247.

[50] O. H. Han, C. S. Kim and S. B. Hong, *Angew. Chem., Int. Ed.*, 2002, **41**, 469–472.

[51] H. Günzler and H.-U. Gremlich, *IR Spectroscopy: An Introduction*, Wiley VCH, Weinheim, 2002.

[52] B. Schrader, *Infrared and Raman Spectroscopy*, VCH GmbH., Weinheim, 1995.

[53] H. Haken and H. C. Wolf, *Molekülphysik und Quantenchemie*, Springer-Verlag, Berlin, 1994.

[54] W. Demtröder, *Molecular Physics. Theoretical Principles and Experimental Methods*, Wiley VCH, Weinheim, 2005.

[55] M. Brustolon and E. Giamello, *Electron Paramagnetic Resonance: A Practitioner's Toolkit*, Wiley VCH, New York, 2009.

[56] F. Gerson and W. Huber, *Electron Spin Resonance Spectroscpy of Organic Radicals*, Wiley-VCH, Weinheim, 2003.

[57] J. A. Weil, J. R. Bolton and J. E. Wertz, *Electron paramagnetic resonance : elementary theory and practical applications*, Wiley VCH, New York, 1994.

[58] N. M. Atherton, *Principles of Electron Spin Resonance*, Ellis Horwood Limited, Chichester, 1993.

[59] C. P. J. Poole and H. A. Farach, *The Theory of Magnetic Resonance*, Wiley VCH, New York, 1972.

[60] W. J. Weltner, *Magnetic Atoms and Molecules*, Van Nostrand Reinold Company Inc., New York, 1983.

[61] J. P. Hobson and R. A. Armstrong, *J. Phys. Chem.*, 1963, **67**, 2000–2007.

[62] S. Brunauer, P. H. Emmett and E. Teller, *J. Am. Chem. Soc.*, 1938, **60**, 309–319.

[63] A. B. Ene, M. Bauer, T. Archipov and E. Roduner, *Phys. Chem. Chem. Phys.*, 2010, **12**, 6520 – 6531.

[64] V. F. Anufrienko, N. N. Bulgakov, N. T. Vasenin, S. A. Yashnik, L. T. Tsikoza, S. V. Vosel and Z. R. Ismagilov, *Dokl. Chem.*, 2002, **386**, 273–276.

[65] T. Beutel, J. Sarkany, G. D. Lei, J. Y. Yan and W. M. H. Sachtler, *J. Phys. Chem.*, 1996, **100**, 845–851.

[66] J. Sarkany and W. M. H. Sachtler, *Zeolites*, 1994, **14**, 7–11.

[67] M. H. Groothaert, K. Pierloot, A. Delabie and R. A. Schoonheydt, *Phys. Chem. Chem. Phys.*, 2003, **5**, 2135–2144.

[68] A. Jentys, G. Warecka and J. A. Lercher, *J. Mol. Catal.*, 1989, **51**, 309–327.

[69] J. Sarkany, *Appl. Catal., A*, 1999, **188**, 369–379.

[70] L. Que and W. B. Tolman, *Angew. Chem., Int. Ed.*, 2002, **41**, 1114–1137.

[71] P. L. Holland and W. B. Tolman, *Coord. Chem. Rev.*, 1999, **192**, 855–869.

[72] N. Kitajima, K. Fujisawa, C. Fujimoto, Y. Morooka, S. Hashimoto, T. Kitagawa, K. Toriumi, K. Tatsumi and A. Nakamura, *J. Am. Chem. Soc.*, 1992, **114**, 1277–91.

[73] M. H. Groothaert, J. A. van Bokhoven, A. A. Battiston, B. M. Weckhuysen and R. A. Schoonheydt, *J. Am. Chem. Soc.*, 2003, **125**, 7629–7640.

[74] M. LoJacono, G. Fierro, R. Dragone, X. B. Feng, J. dItri and W. K. Hall, *J. Phys. Chem. B*, 1997, **101**, 1979–1984.

[75] S. Santra, T. Archipov, A. B. Ene, H. Komnik, H. Stoll, E. Roduner and G. Rauhut, *Phys. Chem. Chem. Phys.*, 2009, **11**, 8855–8866.

[76] F. Wakabayashi, J. N. Kondo, K. Domen and C. Hirose, *J. Phys. Chem.*, 1996, **100**, 4154–4159.

[77] F. Wakabayashi, T. Fujino, J. N. Kondo, K. Domen and C. Hirose, *J. Phys. Chem.*, 1995, **99**, 14805–14812.

[78] E. Broclawik, J. Datka, B. Gil and P. Kozyra, *Int. J. Mol. Sci.*, 2002, **3**, 435–444.

[79] D. Sengupta, W. F. Schneider, K. C. Hass and J. B. Adams, *Catal. Lett.*, 1999, **61**, 179–186.

[80] J. Sarkany, *J. Mol. Struct.*, 1997, **410**, 95–98.

[81] R. Bulanek, *Phys. Chem. Chem. Phys.*, 2004, **6**, 4208–4214.

[82] O. Bludsky, P. Nachtigall, P. Cicmanec, P. Kotek and R. Bulanek, *Catal. Today*, 2005, **100**, 385–389.

[83] R. Beringer and J. G. Castle, *Phys. Rev.*, 1951, **81**, 82–88.

[84] L. M. Mirica, M. Vance, D. J. Rudd, B. Hedman, K. O. Hodgson, E. I. Solomon and T. D. P. Stack, *Science*, 2005, **308**, 1890–1892.

[85] L. M. Mirica, X. Ottenwaelder and T. D. P. Stack, *Chemical Reviews*, 2004, **104**, 1013–1045.

[86] E. I. Solomon and M. D. Lowery, *Science*, 1993, **259**, 1575–1581.

[87] T. Armaroli, M. Trombetta, A. G. Alejandre, J. R. Solis and G. Busca, *Phys. Chem. Chem. Phys.*, 2000, **2**, 3341–3348.

[88] J. E. Bertie and C. D. Keefe, *J. Mol. Struct.*, 2004, **695-696**, 39–57.

[89] C.-J. Guo, O. Talu and D. T. Hayhurst, *AIChE J.*, 1989, **35**, 573–578.

[90] E. A. Pidko, J. Xu, B. L. Mojet, L. Lefferts, I. R. Subbotina, V. B. Kazansky and A. van Santen, *J. Phys. Chem. B*, 2006, **110**, 22618–22627.

[91] H. Garcia and H. D. Roth, *Chem. Rev.*, 2002, **102**, 3947–4007.

[92] V. A. Bolshov, A. M. Volodin, G. M. Zhidomirov, A. A. Shubin and A. F. Bedilo, *J. Phys. Chem.*, 1994, **98**, 7551–7554.

[93] H. D. Bist, J. C. D. Brand and D. R. Williams, *J. Mol. Spectr.*, 1967, **24**, 402–412.

ACKNOWLEDGMENT

First of all I would like to thank Prof. Dr. Emil Roduner for the supervision of my PhD work and for encouraging me to become a member of his group, of the "Graduate College for Magnetic Resonance" and the SFB706. I am very grateful for his warm support, thoughtful guidance and for giving me the freedom to pursue my own ideas. I am thankful for the opportunity to experience new techniques and to present our activities on numerous conferences, workshops, and seminars.

I gratefully acknowledge Prof. Dr. Micheal Hunger for writing the second advisory opinion and Prof. Dr. Joris van Slageren for taking the chairmanship of the examination board.

I would like to thank Dr. Herbert Dilger for allowing me and helping me to take apart and modify every experimental setup we have, an activity which I enjoyed a lot.

Mrs. Gabriele Bräuning is also acknowledged for her help and guidance with the GC/MS and together with Mrs. Beatrice Omiecienski for getting the chemical reactants and other laboratory items.

I sincerely thank the members of the mechanical workshop and Mr. Jürgen Huske from the electrical workshop for their help in modifying and constructing new experiments, independent of how busy they were or how complex my inquiries were. I would like to thank Mr. Werner Hopf for preparing the EPR tubes and all sorts of other incredible glass pieces. Also I would like to thank the members of the low temperature department for always having some helium left for me.

Dr. Matthias Bauer is acknowledged for the EXAFS and XANES measurements and data evaluation. From the Institute for Technical Chemistry Dr. Sabine Opelt is acknowledged for the BET measurements as well as Jörg Frey for performing the UV-Vis measurements.

I thank Dr. Tanja Archipov and Dr. Shampa Santra for our fruitful discussions concerning the Cu/HY zeolite.

My special thanks go to my HiWi's Alexander Kromer, Christoph Reiter and Moritz Bauer for being my little helpers and doing the sample preparation for me.

I would also like to thank Barbara Vogel and Tobias Kittel for their friendship and for never saying no when I asked for help, no matter if it concerned my experiments, paper work or a coffee break. I also thank Andreas Dreizler, Christopher Jensen and Jesus Zerpa-Unda for the discussions and help with equipment heavier or taller than me.

Benjamin Marchetti is acknowledged not only for correcting my german version of the Summary but also for all our other discussions over a coffee too.

My special thanks go to all of my friends, especially to Cristina Alvarez, Minyoung Young, Gurneet Kaur, Farshid Krimpour and Michael Curcic, who have been at my side all these years no matter the distance or the problems.

Being a part of the Graduate College and the SFB706 was not only a great learning experience but also an occasion to spend wonderful times at various workshops and conferences and meet new people from all over the world. I'm grateful for all the friends I have won among the colleagues of my group but also among the members of the Graduate College.

I also thank the Deutsche Forschungsgemeinschaft and the Land Baden- Württemberg for the financial support through SFB 706.

There are not words enough to thank my parents and my grandparents for their support, trust and confidence but especially for their sacrifice in letting me go. Never will I be able to repay what they have done for me.

CURRICULUM VITAE

Augusta Bianca Ene

Born on 03.04.1981 in Cluj-Napoca, Romania

Educational Qualifications:

1987 - 1999	**Primary and Secondary education at the "George Cosbuc" national college, Cluj-Napoca, Romania**
1999 - 2004	**Study of physics at the University of Stuttgart,Stuttgart, Germany**
2004 - 2005	**Diploma thesis "Determination of Neutral Carbon Concentration in an RF-Plasma by VUV Spectroscopy", Institute for Plasma-science, University of Stuttgart, Germany**
2006 - 2010	**Ph.D. graduation at Institute for Physical Chemistry, University of Stuttgart, Germany**

Publication List

- **A. B. Ene, P. Lindner, R. Stirn, U. Schumacher, Rev. Sci. Instrum. 2007, 78, 123110.**

- **K. Koschorrek, S. M. Richter, A. B. Ene, E. Roduner, R. D. Schmid, V. B. Urlacher, Appl. Microbiol. Biotechnol. 2008, 79, 217.**

- **T. Archipov, S. Santra, A. B. Ene, H. Komnik, H. Stoll, G. Rauhut, E. Roduner, J. Phys. Chem. C 2009, 113, 4107.**

- **U. Schumacher, R. Stirn, A. B. Ene, K. Hirsch, M. Leins, P. Lindner, A. Schulz, M. Walker, IEEE Transactions on Plasma Science 2009, 37, 1836.**

- **S. Santra, T. Archipov, A. B. Ene, H. Komnik, H. Stoll, E. Roduner, G. Rauhut, Phys. Chem. Chem. Phys. 2009, 11, 8855 - 8866.**

- **Augusta Bianca Ene, Matthias Bauer, Tanja Archipov, Emil Roduner, Phys. Chem. Chem. Phys. 2010, 12, 6520 - 6531.**

- **Augusta Bianca Ene, Tanja Archipov, Emil Roduner, J. Phys. Chem. C. 2010, 114 (34), 14571Ű14578.**

- **Augusta Bianca Ene, Tanja Archipov, Emil Roduner, J. Phys. Chem. C. 2011.**